

Microfluidics Applications:

Modelling of Artificial Synaptic Communications and
Interactions of Unsupported Artificial Lipid
Membranes

Dissertation

zur Erlangung des Grades
des Doktors der Naturwissenschaften
der Naturwissenschaftlich-Technischen Fakultät
der Universität des Saarlandes

Von

Harvey Nagy Mounier Tawfik

Saarbrücken

2020

Tag des Kolloquiums: 03.06.2020

Dekan: Prof. Dr. rer. nat. Guido Kickelbick

Berichterstatter: Prof. Dr. Ralf Seemann

Jun. Prof. Dr. Bianca Schrul

Vorsitz: Prof. Dr. Albrecht Ott

Akademischer Mitarbeiter: Dr. Thomas Faidt

Abstract

In this work, we present new microfluidic schemes for studying the formation of free-standing artificial lipid membranes. Using these schemes single and double free-standing lipid membranes can be produced, which are easily accessible for optical and electrophysiological measurements.

We have applied these schemes to study certain interactions between nanoparticles, oils, ions and proteins with lipid membranes. We studied the interaction of apatite nanoparticles with artificial membrane. These nanoparticles are being introduced to red blood cells with Trehalose to be used for cryopreservation. Also, we studied the effect of silicone oil on membrane tension and gramicidin A insertion and functionality on lipid membranes; we have found that addition of 5 and 10% of silicone oil is decreasing membrane tension and increase the conductance of certain monovalent ions. We have found that the addition of CoQ10 to our artificial lipid membrane is increasing the membrane tension and as a result it is decreasing the fluidity of such membrane.

Using a modified version of the microfluidic setup we could produce two free-standing lipid membranes facing each other with the possibility to change the buffer content without disrupting the two lipid membranes. We inserted gramicidin A ion channels to both (pre- and post-synaptic) membranes and later we blocked these channels with calcium ions in only the presynaptic-like membrane.

Zusammenfassung

In dieser Arbeit werden neue mikrofluidische Methoden zur Untersuchung von freistehenden künstlichen Lipidmembranen vorgestellt. Mit Hilfe dieser Methoden können einzelne und doppelte Membranen hergestellt werden, die für optische und elektrophysiologische Messungen gut zugänglich sind.

Diese Methoden wurden zur Untersuchung besonderer Interaktionen zwischen Nanopartikeln, Ölen, Ionen und Proteinen mit Lipidmembranen verwendet. Der Mechanismus von Apatit-Nanopartikel unterstützter Aufnahme von Trehalose in rote Blutkörperchen zur Kryokonservierung konnte anhand Modellsystemen untersucht werden. Auch haben wir die Wirkung von Silikonöl auf die Membranspannung und Gramicidin A Einfügung und Funktionalität auf Lipidmembranen untersucht und festgestellt, dass die Zugabe von 5 und 10% Silikonöl die Membranspannung verringert und die Leitfähigkeit für bestimmte monovalente Ionen erhöht. Wir haben festgestellt, dass die Zugabe von CoQ10 zu unserer künstlichen Lipidmembran die Membranspannung erhöht und dadurch die Fluidität dieser Membran verringert.

Mit einem modifizierten mikrofluidischen Aufbau konnten zwei freistehende sich gegenüber liegende Lipidmembranen erzeugt werden, mit der Möglichkeit, den Pufferinhalt zu ändern, ohne die beiden Lipidmembranen zu zerstören. Wir haben Gramicidin A-Ionenkanäle in beide (prä- und postsynaptische) Membranen eingefügt und später diese Kanäle in der präsynaptische Membran durch Kalziumionen blockiert.

Contents

Abstract	I
Zusammenfassung.....	II
List of Figures	VII
List of Tables	XVIII
Introduction.....	1
Chapter 1: Background and State of Art	4
1.1. Structure and Functions of Biological Cell Membranes.....	4
1.1.1. Architecture of Biological Membranes	5
1.1.2. Membrane Biophysics and Polymorphism.....	10
1.1.3. Electrical Properties of Lipid Membrane	12
1.1.4. Lipid Membrane Tension	14
1.1.5. Mechanisms of membrane fusions	15
1.1.6. Driving Forces for membrane fusions	18
1.2. Structure and Physiology of Neuronal Synapse.....	20
1.2.1. Types of Synapses	20
1.2.2. Relation between Anatomy and Physiology of Synapses	21
1.2.3. Consequences of Vesicles fusions and Vesicles recycling.....	23
1.2.4. Electrophysiology of Neurons during Excitation and Inhibition	24
1.2.5. Factors affecting Synaptic Transmission.....	26
1.3. Patch Clamp Techniques.....	28
1.3.1. Patch Clamp configurations.....	29
1.3.2. Electrical Equivalent Circuit	32
1.3.3. Capacitance Measurements Technique for lipid bilayer	33

1.3.4. Patch Clamp Amplifier	36
1.3.5. Clamp Amplifier Set-up	37
Chapter 2: Molecules, Materials and Experimental Set-up	40
2.1. Experimental Setup.....	40
2.2. Materials	41
2.2.1. Lipids	41
2.2.2. Proteins	44
2.2.3. Coenzyme Q10 (CoQ10)	45
2.2.4. Oils.....	46
2.2.5. Polydimethylsiloxane (PDMS)	47
2.3. Methods	48
2.3.1. Formation of Small Unilamellar Vesicles (SUV).....	48
2.3.2. Microfluidic chips fabrication	48
2.3.3. Microelectrode Fabrication.....	51
Chapter 3: Different Microfluidic Designs for Bilayer Membrane Formation and Membranes Interactions	55
3.1. One Lipid Bilayer Membrane	55
3.1.1. Cross-Geometry	55
3.1.2. Parallel-Channels Geometry.....	57
3.1.3. Tube Geometry	59
3.2. Two Lipid Bilayer Membranes	62
3.2.1. Parallel Channels	62
3.2.2. Parallel Channel Geometry with Different Electrodes Orientation....	64
3.2.3. Cross Geometry	66

Chapter 4: Microfluidic Scheme for Studying the Interaction between Apatite Nanoparticles Loaded with Trehalose and Red Blood Cells 69

4.1. Red Blood Cells Cryopreservation69

4.2. Experimental set-up70

 4.2.1. Formation of a free-standing lipid bilayer in the presence of apatite NP 70

4.3. Interactions between Apatite NPs and RBCs and Fluorescent Evidence70

 4.3.1. Interaction energy between apatite NP and synthetic lipid bilayers... 70

 4.3.2. Translocation of Eu-doped apatite NP through the lipid bilayer..... 72

 4.3.3. Translocation of FITC through the lipid bilayer 73

Chapter 5: Effect of Different Proteins, compounds and Oil Compositions on the Behaviour of Artificial Bilayer Lipid Membranes 74

5.1. Introduction and Concepts74

5.2. Effect of Silicone Oil on Membrane-Tension of Artificial BLM74

 5.2.1. Interfacial Tension of LiCl Droplet in DOPC/Squalene. 75

 5.2.2. Interfacial Tension of NaCl Droplet in DOPC/Squalene 77

 5.2.3. Interfacial Tension of KCl Droplet in DOPC/Squalene 79

 5.2.4. Contact Angle Measurements and Free-Energy Gain Calculations.. 81

5.3. Effect of Silicone Oil on Gramicidin A Functionality in BLM..... 82

 5.3.1. Effect of Silicone oil on Current Measurements through Gramicidin A Ion Channels. 83

 5.3.2. Effect of Calcium Ions on Functional gA Channels in BLM. 85

 5.3.3. Different Ions Transfer Through Gramicidin A Ion Channels in BLM86

5.4. Effect of Coenzyme Q10 on Unsupported Bilayer Membranes.....90

Chapter 6: Modelling an Artificial Synaptic Communications in Microfluidic Platform.....	94
6.1. The Need for Artificial Synapse.	94
6.2. The Experimental-Mimicking of Neuronal Synapse.....	94
6.2.1. The Concept of Artificial Synapse	95
6.3. Designs for Artificial Synapses.....	95
6.3.1. Three-Parallel Channels Artificial Neuronal Synapse-Like Model ...	96
6.3.2. Two-Parallel One-Perpendicular Artificial Neuronal Synapse-Like Model.....	97
6.4. Step-by-Step Formation of Artificial Neuronal Synapses.....	98
6.4.1. Formation of Two Stable unsupported BLMs.....	98
6.4.2. Insertion of Gramicidin A Protein as a Membrane Receptor-like....	100
6.4.3. Blocking of Gramicidin A Ion Channels in the Presynaptic Area ...	104
Summary	107
Appendix.....	109
Bibliography	111
Acknowledgment	126
Declaration	127

List of Figures

- Figure 1:** A schematic Diagram for a eukaryotic cell. The plasma membrane is surround the cell and is composed mainly of lipid and proteins. The inner organelles are the machines of the cell-firm which responsible for all cell processes. Organelles are found in the cytoplasm and being isolated by outer lipid membranes. 5
- Figure 2:** Schematic diagram of different layers forming a plasma cell membrane. The outermost layer which is in contact with the extracellular fluid is composed of the glycocalix. The innermost layer facing the cytoplasmic side is a network of microfilaments; proteins. The middle layer is formed by the liquid crystalline lipid-protein structure.. 6
- Figure 3:** A schematic diagram for different types of membrane lipids, a) phospholipids main structure, b) Glycolipids main structure and c) Sterols main structure. 8
- Figure 4:** A schematic diagram of membrane proteins and how they are attached to the lipid bilayer membrane, a) Transmembrane proteins attached to the bilayer through the fatty acids chains, b) Integral membrane proteins also by fatty acid chains and c) Peripheral membrane proteins attached to the transmembrane proteins. 10
- Figure 5:** Illustration of different lipid shapes and their effect on lipid phases formation. In the middle, with 0 curvature, lipids forming the lamellar allignment. In case of increasing the positive curvature, lipids arranged in hexagonal then micelles phases. On the opposite side, or negative curvature, lipids forming the inverted or reversed hexagonal or reversed phases 11
- Figure 6:** A flat lipid bilayer separating two ionic solution compartments, the hydrophobic core of the lipid bilayer prevent the flow of ions from one compartment to the other, therefore a lipid membrane can be modelled as an electrical capacitor. 13
- Figure 7:** Two lipid monolayers are contacting to each other to form a lipid bilayer membrane. Θ is the angle formed at the interface between the aqueous and non-aqueous phases. 15
- Figure 8:** Different fusion events occurring in one cell or between different cells. 16
- Figure 9:** Fusion of two lipid membranes: (1) Two lipid membranes (2) A rearrangement in one point initiating the fusion (3) Fusion between the two lipid membranes forming a stalk (4) Hemifusion state (5) Full fusion state (6) 17

Figure 10: Illustration diagram for exocytosis event. The process starts when the n-snc1 is being released from the Syntaxin. After that the fusion process starts through withdrawing and coiling to form a four-strand-coiled structure. Consequently, the two membranes fuses together and the vesicle releases its content to start to recycling steps. Due to presence of α -SNAP and NSF in the cytoplasm of the presynaptic area, dissociation of the three SNARE-complex components and VAMP attaches again to a new synaptic vesicle to start a new cycle. 19

Figure 11: Illustration of neuronal structure and synapses. The diagram is showing different structures of synapses according to their location. 20

Figure 12: Illustration diagram for a chemical synapse showing the neurotransmitter in the presynaptic area (on top) ready to be released towards the receptors in the post synaptic area (below) through the synaptic gap..... 22

Figure 13: Illustration for the postsynaptic membrane protein-receptors with focus on the roles of the second messenger activator. (1) The activation of K^+ ion channels in the postsynaptic membrane (2) cAMP or cGMP activation (3) Activation of intracellular enzymes (4) Gene transcription activation. 22

Figure 14: synaptic vesicle exocytosis and endocytosis. (a) An electron microscope image for a presynaptic terminal of *Drosophila melanogaster* showing small synaptic vesicles inside the yellow circle. (b) A life-cycle of vesicles starting from SNARE-mediated fusion, transmitter release, endocytosis and filling with transmitter and finally attaching to V-SNAREs for another exocytosis event..... 25

Figure 15: Illustration diagram for different nerve potentials. (A) Is a showing the rest potential of spinal motor nerve (B) is a potential inside the soma after nerve excitation (C) is the inhibition potential following the excitatory events. 26

Figure 16: Patch Clamp mode variations. In the upper row, a schematic diagram for single-channel recording with the 2 possible changes that could be done to reach inside-out or open-cell-attached configurations. Whole-cell recording configurations. Starting from the upper middle configuration; On-Cell, and by applying modifications to the electrode or the cell itself, all other configurations have been developed to different measurements techniques and for over-passing limitations of the first technique. 29

Figure 17: (a) Whole-Cell patch recording (b) Whole-Cell capacitive current recording in response to hyperpolarization pulse ($\Delta V= 10$ mV). 32

Figure 18: A schematic diagram for a BLM and equivalent capacitor. The Area ‘A’ of the capacitor is the area of the membrane and the thickness ‘d’ between the two plates is equivalent to the thickness of the membrane.....	35
Figure 19: Schematic diagram for electrical circuit equivalent to the 2-BLMs orientation. (a) Two BLMs parallel to each other and this is equivalent to two capacitors connected in series in an electrical circuit (b). (c) The equation is simply showing the effect of connecting capacitors in series on the total capacitance.....	35
Figure 20: A schematic diagram for the situation of insertion of ion channels in one of the membranes. (a) Is showing two BLMs with ion channels in one BLM. (b) The electrical equivalent for the previous case (two membrane equivalent circuit) which is not applied in the one-two membranes equivalent circuit (c) A simple electrical circuit with a capacitor and resistor connected in series which is considered to be the equivalent modal for this situation.	36
Figure 21: Illustration diagram for the lock-in amplifier showing all built-in components	37
Figure 22: EPC 10 USB Patch Clamp Amplifier. (a) The main unit, (b) the probe and (c) the model cell.....	39
Figure 23: the experimental setup for fabrication of lipid bilayer membranes in microfluidics platforms.....	41
Figure 24: Chemical structure of Monoolein.....	42
Figure 25: Chemical structure of DOPC	42
Figure 26: Chemical structure of DOPS	43
Figure 27: Chemical structure of NBD-PE.....	43
Figure 28: Chemical structure of Cholesterol.....	44
Figure 29: Gramicidin A insertion into lipid bilayer membrane. In the left part, the two subunits of the gramicidin A are diffusing in the lipid membrane until they find each other to form an ion channel; like in the right diagram. In the right diagram, illustration of one functional ion channel.....	45
Figure 30: Chemical structure of Coenzyme Q10	45

Figure 31: Chemical structure of squalene 47

Figure 32: General Chemical structure of any Silicon oil. 47

Figure 33: photolithography procedures (a) addition of SU-8 50 to pre-cleaned silicon wafer (b) after spin coating, the SU-8 is uniformly distributed (c) soft baking to evaporate the solvent of the photoresist (d) the mask is on top of the silicon wafer then starting UV exposure (e) the final SU-8 master after development 49

Figure 34: Soft lithography procedures (a) Cleaned SU-8 50 master prepared by photolithography (b) addition of PDMS mixture to the master (c) baking of the PDMS mixture (d) the PDMS is peeled from the master (e) plasma treatment for PDMS and glass followed by attaching both part to each other (f) heating the chip to insure irreversible bonding..... 51

Figure 35: our setup for electrical measurements. Electrodes sealed to the PDMS chip and connected to the amplifier through the head stage of the HEKA setup..... 54

Figure 36: Cross-Geometry microfluidic chip; a) an image for empty chip, b) insertion of water from 2 facing-inlets, c) the two water finger touch each other to form a bilayer, d) a lipid bilayer membrane formed in the middle between the fingers 56

Figure 37: Capacitance measurement graph for bilayer membrane formation. Section (a) is showing the first stage in BLM formation in which the 2 monolayers touch each other but no BLM formed yet. Section (b) is the jump in capacitance once the zipping starts. Section (c) is almost a fixed membrane is formed and yielding a stable capacitance. Section (d) the 2 monolayers are separated again from each other and capacitance drops to reach almost zero with time. 57

Figure 38: Two parallel-channels geometry. (a) The start of the experiment by introduction of the aqueous phase from both sides. (b) The two water fingers are getting close to each other to start the fusion. (c) The fusion has started in a small area and continue to form a BLM. (d) The BLM extend until it reach a specific area according to the gap width..... 58

Figure 39: Electrophysiological measurements for BLM formation in the parallel-channels geometry. Section (a) is showing the first stage in BLM formation in which the 2 monolayers touch each other but no BLM formed yet. Section (b) is the jump in capacitance once the zipping starts. Section (c) is showing slight increase in BLM area. Section (d) is showing a slower increase in the formed BLM..... 59

Figure 40: schematic diagram of the Tube scheme for building a BLM. (a) Schematic diagram showing the concept of the design, two opposing electrolyte solutions separated by oil-lipid mixture, with time the oil drain and the two monolayers fuse and form the BLM. (b) In a PTFE tube, we have tried first to build a BLM (inside the yellow ring) and record capacitance of the formed membrane. (c) In homemade PDMS channel, we have applied the same procedures to build a BLM. (d) We were able to build many BLMs in a parallel way with different lipid composition..... 60

Figure 41: A real image for a more professional 'Tubing' system. (a) A tube with 4 mm diameter connected from both sides with 2 glass syringes to push the electrolyte solution from both sides and prevent its leakage, on top of the tube from both sides, there are 2 electrodes were inserted through 2 holes and connected to the HEKA amplifier, in the middle; inside the yellow circle, the BLM was formed. (b) An electrical capacitance curve was recorded to ensure the formation of a BLM; in section 'a' the gradual increase in the bilayer area is exported as increase the capacitance value until reaching a fixed membrane area as in section 'b' 61

Figure 42: Schematic Diagram for microfluidic chip to generate 2 free-standing BLMs. (a) A schematic diagram describing the concept of design, three channels separated by 2 walls and 2 middle gaps where the three water fingers meet each other to form parallel membranes. The diagram is also showing the positioning of electrodes to. (b) After perfusion of the chip with the buffer. (c) The three water fingers started to touch each other to form 2 BLMs. (d) The 2 BLMs are already formed and highlighted by the yellow circles. 62

Figure 43: Capacitance measurement for 2 BLMs connected in series. (a) The 2 BLMs are connected in a series connection and giving a capacitance in the range of 30-35 pF. (b) One BLM has ruptured and creating a situation of single BLM represented by the jump in capacitance..... 64

Figure 44: Schematic Diagram for microfluidic chip to generate 2 free-standing BLMs. (a) Schematic diagram for the design of the chip showing the inlets for buffer solution and oil-lipid mixture with orientation for electrodes inlets. (b) Microscopic image for empty chip with illustration for inlets. (c) After filling the chip with oil, the perfusion of the chip with buffers from the three channels started. The 2 black electrodes (100 μm diameter) are inserted from both sides. (d) The middle buffer finger is reaching the middle gap area and form 2 free-standing BLMs inside the yellow circles. 65

Figure 45: Capacitance measurement for 2 BLMs connected electrically in series. (a) In the first phase no BLMs are being formed yet and no capacitance was recorded. (b) The 2 BLMs are connected in a series connection and giving a capacitance in the range of 30-

35 pF. (c) One BLM has ruptured and creating a situation of single BLM represented by the jump in capacitance..... 66

Figure 46: Microscopic Images for Cross-Geometry one-outlet Design. (a) Empty chip with illustrations for the different inlets. (b) After insertion of water fingers, the three interfaces, covered with lipids, come close to each other's to start zipping and formation of the BLMs. (c) The 2 BLMs are formed in the specified gap and the middle channel is still moving. (d) A closer look for the formed BLMs highlighted with yellow circles.. 67

Figure 47: Microscopic Images for Cross-Geometry two-outlet Design. (a) Empty chip with illustrations for the different inlets and outlets. (b) After insertion of water fingers, the three interfaces, covered with lipids, come close to each other's to start zipping and formation of the BLMs. (c) The 2 BLMs are formed in the specified gap and the middle channel is still moving. (d) A closer look for the formed BLMs highlighted with yellow circles. 68

Figure 48 Illustration diagram for formation of free-standing lipid membrane in microfluidic chip, apatite NPs are dispersed in the aqueous phase, while the continuous phase is the oil in which the lipid molecules are dissolved. 70

Figure 49: Langmuir isotherms describing the bilayer coverage as function of NPs concentrations and medium pH. 72

Figure 50: Fluorescing Eu-doped apatite NP attached to the lipid bilayer as evidence of non-crossing the lipid membrane..... 72

Figure 51: Two water droplets with their interfaces separated by a DOPC lipid bilayer one of them contains fluorescent FITC loaded on apatite NPs while the other is empty, at time= 0, the empty droplet is not fluorescent while over time a fluorescence is appearing as an evidence of translocation of FITC to the other droplet with help of the NPs. 73

Figure 52: Interfacial Tension Measurements of LiCl droplet in DOPC/Squalene/Si Ar20 0%. 8 different trails T1 to T8 were done to make an average with standard error. 75

Figure 53: Interfacial Tension Measurements of LiCl droplet in DOPC/Squalene/Si Ar20 0.1%. 9 different trails T1 to T8 were done to make an average with standard error. 76

Figure 54: Interfacial Tension Measurements of LiCl droplet in DOPC/Squalene/Si Ar20 1%. 8 different trails T1 to T8 were done to make an average with standard error. 76

Figure 55: Interfacial Tension Measurements of NaCl droplet in DOPC/Squalene/Si Ar20 0%. 8 different trails T1 to T8 were done to make an average with standard error. 77

Figure 56: Interfacial Tension Measurements of NaCl droplet in DOPC/Squalene/Si Ar20 0.1%. 8 different trails T1 to T8 were done to make an average with standard error. 78

Figure 57: Interfacial Tension Measurements of NaCl droplet in DOPC/Squalene/Si Ar20 1%. 8 different trails T1 to T8 were done to make an average with standard error. 78

Figure 58: Interfacial Tension Measurements of KCl droplet in DOPC/Squalene/Si Ar20 0%. 8 different trails T1 to T8 were done to make an average with standard error. 79

Figure 59: Interfacial Tension Measurements of KCl droplet in DOPC/Squalene/Si Ar20 0.1%. 8 different trails T1 to T8 were done to make an average with standard error. ... 80

Figure 60: Interfacial Tension Measurements of KCl droplet in DOPC/Squalene/Si Ar20 1%. 8 different trails T1 to T8 were done to make an average with standard error. 80

Figure 61: Formation of a bilayer lipid membrane for measuring membrane tension. A) The two monolayers are decorating the two electrolyte solutions before contacting each other. B) The two monolayers touched each other but not zipped yet to form a BLM. C) The BLM formed by zipping and contact angle was measured. 81

Figure 62: IV-Analysis of monoolein BLM with and without gramicidin A. A) Electroporation curve due to absence of ion channel through which current would flow from one side to the other. The increase by application of 200mV is indicating the existence of pores in the membrane but not due to gA. B) IV-Curve showing the effect of gA on current measurements. The current measured is proportional to the applied voltage. 83

Figure 63: IV-Analysis of monoolein BLM with and without silicon oil in presence of gramicidin A. A) IV-Curve showing the effect of gA on current measurements. The current measured is proportional to the applied voltage. No Si AR20 was added during this measurement. B) In presence of Si Ar20 there is a minor shift in the IV curve. This is an indication for the assembly of Si Ar20 between lipid molecules which may affect the functionality of gA ion channels. 84

Figure 64: Patchmaster-Software images for IV-analysis of monoolein BLM in presence of gA ion channels. A) The green points are indicating the current measured upon application of voltage during membrane zipping process. B) After the zipping, gA ion channels started the assembly process and this could be noticed from the slight current (10 nA) recorded. C) After the assembly of gA ion channels, the proportional IV relation started to be noticed. 85

Figure 65: IV curves for monoolein BLM + Squalene + Si Ar20 in absence and presence of Ca^{+2} . A) IV analysis for monoolein BLM in presence of Si AR20 and functional gA ion channels. B) After addition of Ca^{+2} to the system, all gA ion channels were blocked by Ca^{+2} to reach almost zero ampere..... 85

Figure 66: IV-Analysis for different ions transfer through gA ion channels in absence of Si Oil. According to the atomic weight, the transfer velocity from through gA ion channels is increasing with increase in atomic weight until reaching Rb^{+} and Cs^{+} which have a very close transfer rate and sometimes Rb^{+} is faster than Cs^{+} 86

Figure 67: IV-Analysis of different ions transfer through gA ion channels in monoolein BLM. Upon addition of very low concentrations of Si Ar20; 0.1, 0.2 and 0.3%, we did not notice a major differences in conductance of gA ion channels. All conductance measurements are within the same order like in 0% Si Ar20..... 87

Figure 68: The difference in conductance between the 5 ions in 4 different oil compositions. We can notice that Li^{+} have the lowest conductance in all oil compositions, while Rb and Cs are the higher in conductance. K^{+} conductance had decreased after the addition of Si Ar20. In general there is a decrease in conductance for all ions after the addition of Si Ar20 except in Li^{+} which has the lowest conductance..... 88

Figure 69: IV-Analysis of different ions transfer through gA ion channels in monoolein BLM. Upon addition of higher concentrations of Si Ar20; 5 and 10%, we noticed a major differences in conductance of gA ion channels. The predicted conductance for each has increased and lost the stated order for conductance. An increase in Li^{+} conductance was detected. There is increase in the conductance of K^{+} higher than Cs^{+} in both 5 and 10%. 88

Figure 70: The differences in conductance between the 5 ions in 3 different oil compositions. Li^{+} conductance has increased by folds while still the lower in conductance when compared to the other ions. There were also an increase in the conductance of Na^{+} and K^{+} with increase of Si Ar20 concentration when compared to 0%. K^{+} has recorded higher conductance than Cs^{+} with 5 and 10% Si Ar20 concentrations. Rb^{+} has recorded the higher conductance at 5 and 10% Si Ar20. 89

Figure 71: A microscopic image for the setup used for studying the effect of CoQ10 on BLM. Due to lipophilic nature of CoQ10, it is being dissolved in the lipid/oil mixture and perfused in this chip. The contact angle Θ was measured to calculate membrane tension. 90

Figure 72: Specific capacitance plotted as a function of CoQ10 concentration in the BLM. C_s was found to be increasing with the increase CoQ10 concentration. Above CoQ10 concentration of 0.001 mg/ml there were no membranes formed due to higher concentration..... 91

Figure 73: Interfacial tension measurements for different CoQ10 concentrations in DPhPC/Squalene system. A) Three different measurements and average extraction of pure DPhPC/Squalene droplet. B) Three different measurements and average extraction of 0.0005mg/ml CoQ10 in DPhPC/Squalene droplet. C) Three different measurements and average extraction of 0.001mg/ml CoQ10 in DPhPC/Squalene droplet. From the above measurements, the interfacial tension of DPhPC/Squalene is increasing with increase of CoQ10 concentration..... 91

Figure 74: Effect of CoQ10 on interfacial tension and membrane tension of DPhPC/Squalene system. A) Plotting for interfacial tension for three different concentrations as a function of CoQ10 concentration with standard error. With the increase in CoQ10 concentration, there was increase in interfacial tension of DPhPC/Squalene droplet. B) Membrane tension for the three different concentrations as a function of CoQ10 concentration with standard error. Due to increase in interfacial tension with the increase in CoQ10 concentration, there were also increase in membrane tension of DPhPC/Squalene BLM. 92

Figure 75: Concept of building artificial synapse into a microfluidic chip. a) A schematic diagram for neuronal synapse. b) An empty schematic diagram showing the pre- and postsynaptic membranes. c) A schematic diagram for the pre- and postsynaptic membranes. 95

Figure 76: Design 1 for a neuronal synapse-like model. a) An empty chip showing different inlets and outlets. The yellow circles are highlighting the functional area; where the unsupported bilayer membranes are formed. b) A succesful attempt to build a synaptic structure showing the pre-/ postsynaptic free-flow of buffers and a fixed middle droplet representing the synaptic gap..... 96

Figure 77: Design 2 for a neuronal synapse-like model. a) An empty chip showing different inlets and outles. The yellow circles are highlighting the two opening where the two BLMs will be formed. b) the arrows are showing the directios of movements of each channel. The middle channel is composed of to intersecting inlets to generate the middle

buffer droplet. c) the middle droplet has reached the middle area to start forming the 2 opposing membranes. d) After few seconds, the 2 BLMs have been formed while the flow in the upper channel (the presynaptic area) is continuous. 98

Figure 78: Capacitance measurements for 2 unsupported bilayer membranes opposing to each other. These minor fluctuations resulted from movements in BLMs positions slightly over time. The average of 50 pF is a proof for the formation of the needed system and stability for long time. 99

Figure 79: Capacitance measurements for 2 unsupported bilayer membranes. This graph is showing the case of rupturing of one of the two BLMs. a) one membrane is formed but the other membrane is not yet. b) After the zipping of the second membrane, the capacitance has recorded about 40 pF for few minutes. c) After rupturing of one of the two membranes, the capacitance jumped to almost 80 pF. 100

Figure 80: Assembly of Gramicidin A subunits into a BLM. A) In the beginning of the experiment, the two subunits of gramicidin A are distributed in the buffer of channels 2 and 3. Channel 3 is playing the role of postsynaptic area. B) After continuous flow in the chip, 2 BLMs were formed while the gramicidin A channels are formed only in the lower BLM; because there is no any subunits from the protein in channel 1. 101

Figure 81: Capacitance measurements for two membranes in presence of gA. A) The capacitance measurement recording around 100 pF while optically there were two BLMs formed. B) A microscopic image with illustration of the position of the gA and the equivalent electrical component. The upper membrane is representing the presynaptic membrane and the lower membrane is representing the postsynaptic membrane. 102

Figure 82: Capacitance measurements of 2 BLMs with gA in all channels. A) Capacitance jump delayed about 75 seconds until the jump to about 60 pF indicating the formation of the 2 BLMs. B) A microscopic image for stable 2 BLMs with illustration to the position of gA in both channels. 103

Figure 83: Capacitance measurements of 2 BLMs with gA in all channels. A) Capacitance jump after 10 seconds then drop from 50 pF to almost 0 F after formation of the 2 BLMs and assembly of the ion channels, respectively. B) A microscopic image for stable 2 BLMs with illustration to the position of gA in both channels. **Error!**
Bookmark not defined.

Figure 84: Assembly of Gramicidin A subunits into the 2 BLMs. A) In the beginning of the experiment, the two subunits of gramicidin A are distributed in the buffer of the 3 channels. Channel 3 is playing the role of postsynaptic area while channel 1 is

representing the presynaptic area. B) After continuous flow in the chip, 2 BLMs were formed and gramicidin A ion channels are being formed in both BLMs. 104

Figure 85: Assembly of Gramicidin A subunits into the 2 BLMs in presence of Ca^{+2} ions. A) gA ion channels are being inserted into both BLMs. B) Ca^{+2} ions started to reach the presynaptic-membrane area and block any gA channels. 104

Figure 86: Capacitance measurements for insertion of gA and the effect of Ca^{+2} . A) Capacitance measurements is showing three crucial steps: 1. Formation of the 2 BLMs representing the pre- and postsynaptic membranes. 2. Insertion of gA in both and the drop in capacitance. 3. The flow of Ca^{+2} in the presynaptic area and the blockade of gA ion channels which is shown as increase in capacitance above that measured in the first step. B) A microscopic image for stable 2 BLMs. 105

List of Tables

Table 1: Microfabrication parameters.....	50
Table 2: Micropipette Pulling Parameters	53
Table 3: Calculated value of equilibrium constant (Langmuir) K_1 for the system NP/bilayer and related value of the standard free energy of interaction ΔG°	71
Table 4: Interfacial tension measurements of LiCl droplets as a function of Si Ar20 percentage:.....	77
Table 5: Interfacial tension measurements of NaCl droplets as a function of Si Ar20 percentage:.....	79
Table 6: Interfacial tension measurements of KCl droplets as a function of Si Ar20 percentage:.....	81
Table 7: The free energy-gain before/after formation of a BLM in presence/absence of Si Ar20:	82
Table 8: The effect of CoQ10 on membrane thickness, specific capacitance, Surface tension and membrane tension.	92

Introduction

Thousands of years ago, God created all living creatures; unique and distinctive, in which the 'cell' is the building and the functional unit. Until today, researchers are dedicating thousands of research to fully understand the structure-function relationship of these cells. Living cells could be classified mainly into two main types; prokaryotes and eukaryotes [1]. The prokaryotes, like bacteria, are primitive organisms with nucleic acid without nucleic envelope and have cell membranes [2, 3]. On the other hand, the prokaryotes, like animal cells, are more sophisticated and advanced cells where the nucleic components are enclosed in an envelope and different organelles are partitioning off different functions. Lipid membranes are surrounding these organelles and the entire cell; in other words, cells are defined structurally by lipid membranes and contain organelles which are also surrounded by lipid membranes [1, 4, 5].

These lipid membranes are the keys for *compartmentalisation* of different organelles and are considered to be the gates for each cells [1, 2]. Mainly, they are composed of fatty acids that self-assembled to build lipid membranes for the cells and for the inside organelles [2]. The communication between these organelles inside a cell and between cells and each other's is requiring specific permission-pass through these lipid membranes; which are vesicles [6, 7]. The formation of these vesicles happen when they engulf their specific cargo inside and then pudding take place to create vesicles [6]. These vesicles fuse later with another membrane to transfer the loaded cargo [8]. The fusion of these vesicles to lipid membranes is derived by fusogenic proteins such as SNAREs [9, 10].

In this thesis, we present different microfluidic platforms to study artificial, unsupported lipid membranes. The concept of all experiments is droplet interface bilayers (DiBs) which was presented by H. Barely in 2008 [11]. Utilizing this concept, we were able not only to produce one free-standing or unsupported bilayer membrane but also two free-standing bilayer membranes facing each other. For all experiments, we have observed the interaction between membranes optically (optical microscope) and by electrophysiological means (patch clamp).

We have studied the interaction between apatite nanoparticles and a free-standing phospholipid membrane [12]. These nanoparticles were used to transfer a natural Cryo-preserved; Trehalose, inside red blood cells to improve their viability after cryopreservation [12]. Apatite is composed of calcium phosphate which is biocompatible and biodegradable [13, 14]. The interaction between trehalose solution, apatite nanoparticles and artificial lipid membrane was observed by fluorescent microscopy and patch clamping. We have noticed that apatite nanoparticles mediated the insertion of trehalose inside the RBCs resulting in increasing the viability of freeze/thawed RBCs.

Also, we have focused on lipid membranes composition and subsequently the effect on their tension and on their interaction with molecules. Due to this purpose, we have used silicone oil, to decrease membrane tension and study their behaviour. We studied such interactions through interfacial tension measurements. Besides that, we have inserted an ion-channel-forming protein; gramicidin A, to the membrane to study whether their functionality; in gating ions through a bilayer, is affected. We used different monovalent ions to study how their transfer through the ion channel was affected by the different membrane tensions [15].

Another interaction that was studied in this work, is the interaction between coenzyme Q10 and artificial free-standing lipid membranes. Coenzyme Q10 is an enzyme that is embedded in the membrane of the mitochondria [16]. This anti-oxidant, vitamin-like enzyme is a member of the electron transport chain and participates in ATP production through the aerobic cellular respiration [17]. Due to its lipophilic nature, we inserted it in our lipid membrane scheme to study its effect on the membrane tension. We applied interfacial tension and electrophysiological measurements to study such effect. We have found that this antioxidant is increasing the membrane tension and decreasing the fluidity of the bilayer.

Finally, we present in this work, a new microfluidic scheme to build a model for an artificial neuronal synapse; we call it 'Artificial Synapse'. We are modelling an artificial synaptic communication.

Chapter 1: Background and State of Art

This chapter is composed mainly of two sections and the first section we will divide into two parts. In the first part, a description of cell membrane biology and the physics behind biological processes such as self-assembly of lipid molecules and membranes interactions which lead to fusion or exo- and endocytosis. A description of membrane polymorphism, membrane tension and its electrical properties. The second part of the first section will be concerned in synapse, mainly the structure and physiology behind them. In the second section of the chapter, a description for patch clamp techniques were used to characterize the electrical properties of lipid membrane.

1.1. Structure and Functions of Biological Cell Membranes

Biological cell membrane of any living organisms (fig. 1) is consisting of a lipid bilayer [18, 19]. It is very important for all living organism that no one can survive without such membranes [20]. All biological membrane are high selective and permeable barriers [21]. Simply, it could be described as a thin polar membrane of two sheets of lipid molecules that is surrounding the entire cell and responsible for cell morphology plus communication with neighbor cells [18]. The lipid bilayer is flexible and fragile at the same time and all these features are controlling all physiological process [19]

All cell membranes must be able to constantly keep the specific electrochemical gradients between the cell and the surrounding environment thanks to proteins attached to the membrane [20]. These proteins must regulate movement of ions and nutrients from inside and outside the cell and vice versa [20]. This is happening because membrane proteins are also serving as regulators and sensors for surrounding materials [22]. The protein integrated inside the membrane can be described as a solute molecule embedded in a complex anisotropic structure [21, 23]. Furthermore, inside the one cell, lipid membranes play a significant role in compartmentalization of organelles through separations and maintaining the specific organelle functionality [24, 25, 26]. Organelles representing the miniature model of neighbor cells; each has its own function besides working all together giving the final function of the main cell. These organelles are working together through a process known as intracellular trafficking vesicles [24, 27].

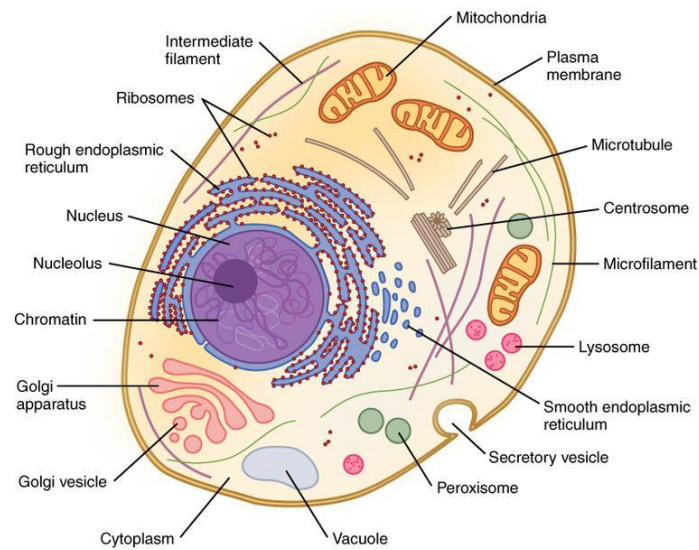


Figure 1: A schematic Diagram for a eukaryotic cell. The plasma membrane is surrounded the cell and is composed mainly of lipid and proteins. The inner organelles are the machines of the cell-firm which responsible for all cell processes. Organelles are found in the cytoplasm and being isolated by outer lipid membranes. Copyright This work is licensed under a Creative Commons Attribution 4.0 International License CC BY 4.0 (Wikipedia, 2016)

Vesicles are small structure surrounded by lipid membranes and serve as a delivery compartment inside the cell; moving in the cytoplasm from one organelle to another, maintain the functionality and integrity of organelles and consequently the cell [28].

1.1.1. Architecture of Biological Membranes

A cell membrane could be divided into three layers [29]; the middle layer is a mixture of lipids and proteins covered by the most outer layer which is a glycocalix film which is carbohydrate-enriched surface or molecules. Glycocalix functions as a barrier between the cell and the surrounding environment. Glycocalix could be considered as a sensor which is regulating the communication between extra- and intracellular environment [29]. The inner layer is a network of filaments consisting of macromolecular actin; called also the cytoskeleton [29]. Most biological membranes are consisting of lipids, proteins and sugars [20, 19] for ensuring fluidity (fig. 2). This fluidity enables rotation and diffusion within the membrane leading to the needed physiological functions [19, 20]. Upon talking about the composition of a lipid membrane, we must describe two main points; the first point is the constituents and the

second point is the assembly. Regarding constituents, cytoplasmic membrane or plasma membrane is composed of hundreds of different lipids that are mixed together un-uniformly [30]. The major constituents of the lipid membranes are phospholipids, glycoproteins and cholesterol [18]. Concerning the assembly, the lipid composition is highly distinctive for each membrane; plasma membrane composition is not the same between organisms or even cell types [30]. Lipids and proteins are being held together through non-covalent bonds [31]. Only a small category of proteins is integrated and held in cell membrane by covalent attachment of complex phospholipid anchor to the carboxylic terminal of the protein [31, 32]. The plasma membranes plays very important roles such as selective filtration controlling the transfer of ions or other molecules and the lipid bilayer is considered as an energy source through glycolysis [20].

The asymmetry of plasma membrane lipids; different biological lipids are existing in the same membrane, has been well-studied [33, [19]. Such asymmetry resulted from certain phenomena such as lipid remodeling, biosynthesis, incorporation of exogenous lipids and intracellular lipid traffic [33].

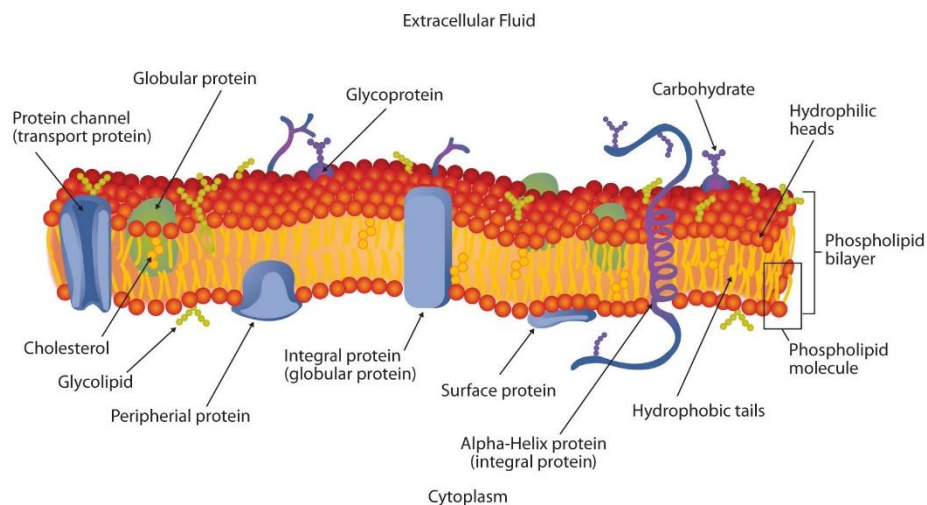


Figure 2: Schematic diagram of different layers forming a plasma cell membrane. The outermost layer which is in contact with the extracellular fluid is composed of the glycocalyx. The innermost layer facing the cytoplasmic side is a network of microfilaments, proteins. The middle layer is formed by the liquid crystalline lipid-protein structure. This work is licensed under a Creative Commons Attribution-ShareAlike 3.0 Unported License. (CC BY-SA 3.0) (Ruiz, 2007)

1.1.1.1. Membrane Lipids

The lipid barrier is considered a functional selective barrier not only between adjacent cells but also between internal organelles in the one cell [34]. They act as the

backbone of the membrane and provide the barrier between the cytoplasm and the extracellular environment. Lipids play very important roles in the cytoplasmic membrane [20, 24]. One role is related to their amphiphilic nature; this is essential in membrane assembly and consequently cell formation and internal organelles compartmentalization [24]. Another role is acting as messengers for molecules recognitions and signal transduction [24]. It has been proved that many of genetic diseases such as cancer diabetes and Alzheimer, are associated with changes in lipid orientation and metabolism which in turn showing the importance of membrane lipids in normal physiology [30, 34].

Amphipathic; amphiphilic nature of lipids means that a single lipid molecule contains both a polar (hydrophilic) part which is the *head* and a non-polar (hydrophobic) part which is the hydrocarbon chain forming the *tail*. Generally, lipids have the general formula as follow: $R_1COOCH_2 \cdot CH(OOCR_2) \cdot CH_2OP(O)_2OX$. R_1 and R_2 represent the hydrocarbon chains (i.e. the hydrophobic tail) where X represent the alcohol part of the ester group (i.e. the hydrophilic head) (fig. 3) [18].

Due to the differences of in the polar head group and acyl chains, more than one hundred types of lipids exist in a cell membrane [18]. This lipids diversity is responsible for the functionality and specificity of the cell. Plus it is supporting a wide range of functions for a normal cell [34]. From this point, man can realize how microorganisms are adapting themselves with environmental changes. Examples for functional roles also include regulatory role in cell growth, participate in the formation of some biomolecules and can modulate the enzymatic activity of enzymes [18].

Lipid membranes are being divided into Nano domains or lipid rafts to recruit specific proteins and such lipid rafting is essential in many membrane processes [35]. The physical and chemical properties of membranes are depending on their chemical structure [34]. The chemical properties are results of chemical diversity which consequently affecting the membrane function [34]. Generally, plasma membrane lipids are different between different organisms and between cells and each other but generally the lipid membrane is composed of phosphatidylcholine (PC), Sphingomyelin (SM) and gangliosides (GM) in the outer leaflet [30]. The inner leaflet mainly composed of

phosphatidylethanolamine (PE) and phosphatidylserine (PS) in addition to other lipids [30]. Sterols, mainly cholesterol, is the most important sterol in mammalian cells, it consists of hydrophilic hydroxyl head group, a steroid structure consists of four rings and short hydrocarbon side chain [18, 34].

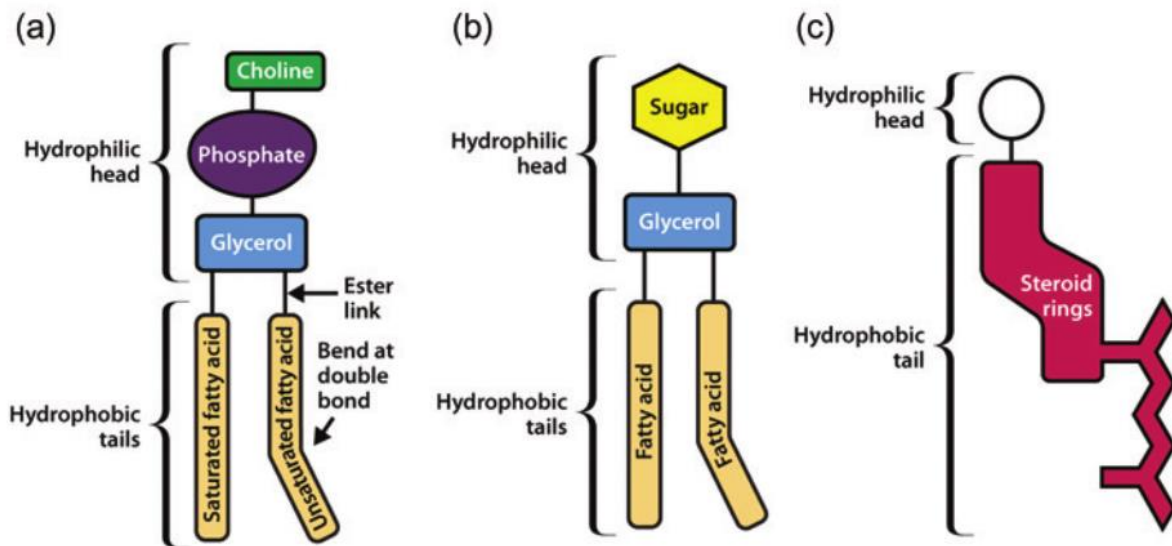


Figure 3: A schematic diagram for different types of membrane lipids, a) phospholipids main structure, b) Glycolipids main structure and c) Sterols main structure. Copyright (2015) Helen Watson, *Biological Membranes*. Attribution 3.0 Unported (CC BY 3.0) (Watson, 2015)

The core of the cell membrane is lipid molecules, mainly phospholipids especially PC with percentage more than 50 % [24]. The combination of PC and PE in one membrane is inducing curvature stress which is crucial in biological process like fusion and budding [24]. PE with other lipids like cardiolipin (CL) play role in protein placement inside the membrane and also affect its activity [24].

Phospholipids themselves have a core structure which is considered as an attachment or coordination point for different groups (fig. 3). Phospholipid molecules are not forming covalent bonds between each other and there for they can be seen as separate molecules in the membrane. In a more specific description, PC is a glycerolphospholipids (GPL) with a glycerol backbone which is the tail and the head, choline group, is composed of phosphate and alcohol (fig. 3a). Glycolipids (fig. 3b) can

be composed of glycerol or sphingosine with a sugar replacing the phosphate group [34, 18].

1.1.1.2. Membrane Proteins

According to the functionality of the cell or the organelle, the biological membrane is containing plenty of different proteins to process these functions [18]. Few examples of such functions include maintaining membrane integrity and organization of flow from outside to inside and vice versa [18]. The high percentage of membrane proteins in a cell indicates the high metabolism of this cell [18]. The orientation of each membrane protein to the cytoplasm is different from other proteins and consequently the characteristics and properties of a monolayer (i.e. one leaflet) of the membrane are highly specific from those of other monolayer [26]. Membrane proteins also are carrying most of specific functions of the cell as fusion, signalling and ion transports in both directions [20]. According to the role, proteins are divided into three main groups (fig. 4) [20]. The first group is the transmembrane proteins 'TM' (fig. 4a) which are penetrating the entire lipid membrane forming a channel connecting the extracellular and intracellular environments [31, 36]. TM are embedded between lipid molecules thanks to their hydrophobic regions where hydrophilic regions are extended on both sides of the lipid membrane [20]. The second group is the lipid-anchored proteins or integral proteins (fig. 4b) which are located outside the lipid membrane and bonded by a covalent bond to lipid molecules; through fatty acids chains [32]. The third group is the peripheral proteins (fig. 4c) which are located completely on the surface of the lipid membranes on both sides; cytoplasmic and extracellular side, and attached to transmembrane protein [18, 31]. The ratio of lipid: protein is ranging between 1:4 and 4:1 [21]. Examples for transmembrane proteins include SNAREs and ion channels [31, 37].

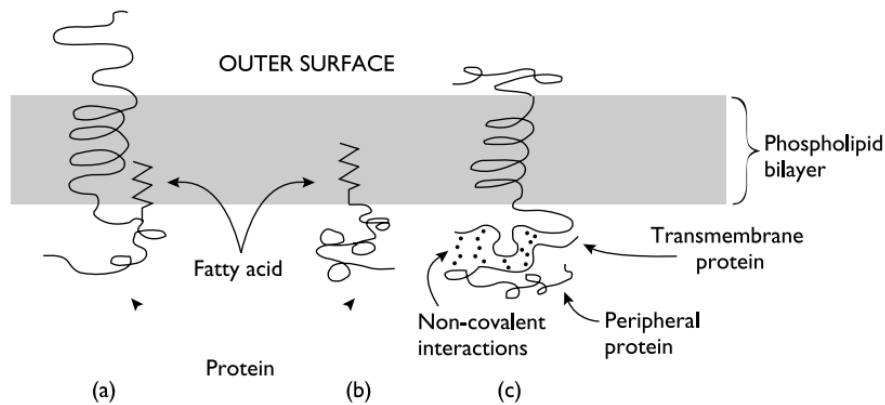


Figure 4: A schematic diagram of membrane proteins and how they are attached to the lipid bilayer membrane, a) Transmembrane proteins attached to the bilayer through the fatty acids chains, b) Integral membrane proteins also by fatty acid chains and c) Peripheral membrane proteins attached to the transmembrane proteins. Copyright (1996) Bernard S. Brown, Biological Membranes. License Number 4892430198282 (Brown., 1997)

1.1.2. Membrane Biophysics and Polymorphism

Due to the amphiphilic nature of lipid molecules, they can aggregate in different ways when they come in contact with water [36, 39]. This phenomenon is called *polymorphism* and the yield shape of this process is called a *phase*. Once these amphiphilic molecules dispersed in aqueous phase, they are arranged or packaged in different shapes or phases [39, 40]. Some of these lipids are packaged in bilayer phase such as PC while the others adopt micelles such as lysolipids and fatty acids (fig. 5) [36, 40]. Lipid phase behavior depends on several factors, some of these factors are intrinsic. An example for such intrinsic factors is the lipid architecture, in other words, the length of the hydrocarbon chains. For example, the increase of hydrocarbon chain length leads to transition from the lamellar phase (L_{α}) to inverted hexagonal phase (H_{II}). It is also found that increase in volume of head groups are leading to lamellar phase (L_{α}) [41].

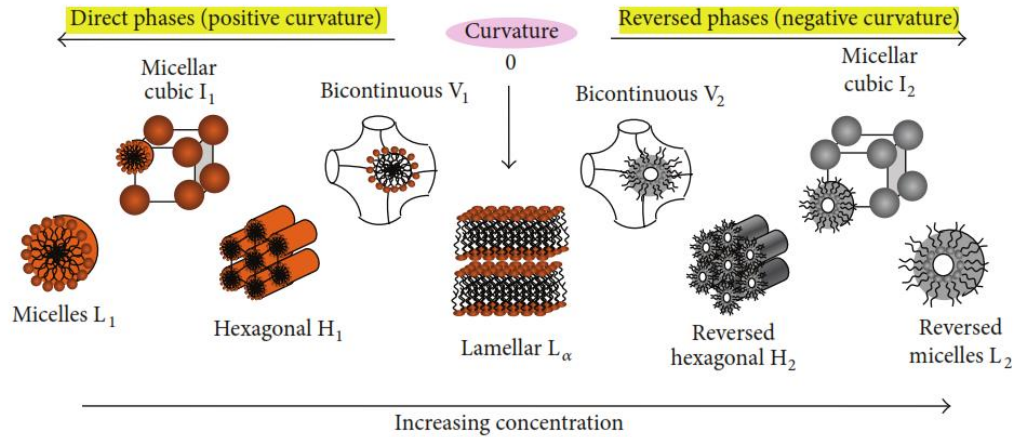


Figure 5: Illustration of different lipid shapes and their effect on lipid phases formation. In the middle, with 0 curvature, lipids forming the lamellar alignment. In case of increasing the positive curvature, lipids arranged in hexagonal then micelles phases. On the opposite side, or negative curvature, lipids forming the inverted or reversed hexagonal or reversed phases. Copyright (2015) Domenico Lombardo et al. Attribution 4.0 Unported (CC By 4.0) (Lombardo, 2015)

Lipids with short chain lengths form more fluid membranes due to less interaction with neighbor lipid molecules. Another intrinsic factor in the degree of saturation in the hydrocarbon chain; in presence of double bonds in the hydrocarbon chain prevents tight packing leading to membrane fluidity (fig. 5) [36]. Most extrinsic factors affecting the polymorphism are temperature, lipid concentration and packing ratio [41]. Packing ratio can be expressed using the following equation:

$$S = \frac{V}{al} \quad \text{Equation 1}$$

where S is packing ratio, V is the volume of hydrocarbon, a is area of the head group and l the length of the hydrocarbon chain.

Hereby, Lipid packing ratio is influenced by two parameters; the first one is the ratio between different head group sizes and the second one is the degree of saturation/unsaturation in the hydrocarbon chain [42]. When the packing ratio S is above or below 1, the membrane can form two hexagonal configurations, also called non-lamellar polymorphism. In other words, when the length of the hydrocarbon chain increase, this can bring transition ranging from lamellar (L_α) to inverted hexagonal phases (H_{II}). There are two Hexagonal phases, the first one is Hexagonal I phase (H_I) and

the second is inverted Hexagonal II phase (H_{II}) [43]. When the packing ratio $S = 1$ (zero curvature) like in PC and PS lipids, they form lamellar phase (fig. 5). When $S < 1$ (positive curvature) they form the H_I phase like the case in monoolein and this is due to presence of one hydrocarbon chain conferring an inversed conical shape (figure 5). When $S > 1$ (negative curvature) like the case of PE lipids, they form the H_{II} phase due to small polar head groups referring a conical shape (fig. 5) [43]. Cholesterol increase the lipid packing and consequently affect the elasticity of the membrane [44]. In general, Increasing the unsaturation and temperature is driving the transition towards the H_{II} phase and increasing the head group size, head group ionization and water content is doing the opposite; increase the lamellar arrangement of lipid molecules.

In addition to packing ratio, the critical micelle concentration factor (CMC) is another way to describe the polymorphism of lipid molecules. The CMC factor is calculated or detected according to the thermodynamic equation of micellization [45]:

$$\ln[CMC] = \frac{\Delta G}{RT} \quad \text{Equation 2}$$

where ΔG is the free energy gain of transfer of a lipid molecule into a corresponding micelle or lipid bilayer, R is universal gas constant and T is the absolute temperature. From the above equation, it is clear that the CMC factor is also affected by temperature and also the pressure [45]. For a certain value, the individual lipids self-assemble to form a micelle or lipid bilayer. Below this value, the lipid molecules behave like a dissolved molecule but there is no association noticed. Above this CMC value, the lipid monomers and micelle are existing in a dynamic equilibrium [46].

1.1.3. Electrical Properties of Lipid Membrane

The biological membrane has many functions plus being a barrier between cells [20]. Thus, they are subjected to many researches to identify their characteristics. Many of these characteristics are existing due to the electrostatic property of the lipid membrane. Simply, the lipid membrane consists of two monolayers of lipid molecules that fused together as shown in figure 7:

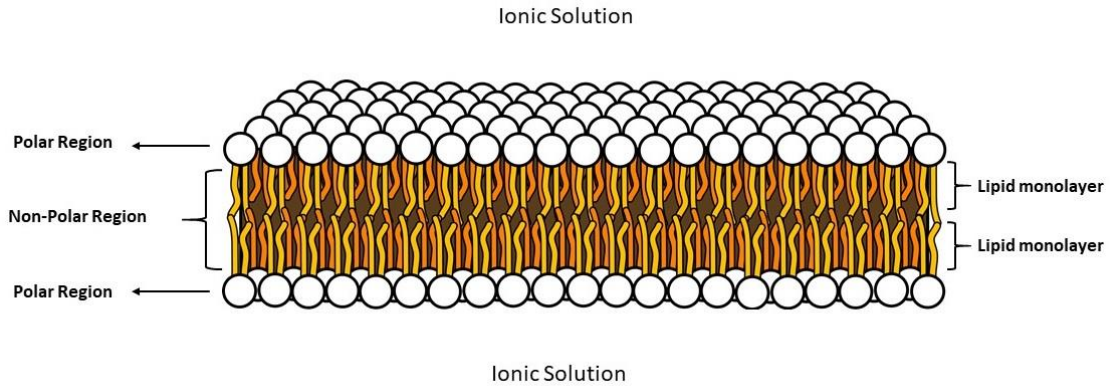


Figure 6: A flat lipid bilayer separating two ionic solution compartments, the hydrophobic core of the lipid bilayer prevent the flow of ions from one compartment to the other, therefore a lipid membrane can be modelled as an electrical capacitor. Adjusted from Wikipedia This work has been released into the **public domain** by its author. (Ruiz, 2007)

From (fig. 6), the two leaflets are being separated by a non-polar area. The hydrophobic area is resembling an electrical capacitor with a capacitance C [47]. This hydrophobic layer: capacitor-like, has a thickness d which depends on the length of the hydrocarbon chain. In other words, the hydrophobic area is indicating that the bilayer behaves like an electrical capacitor where a dielectric material separates the two conducting polar areas. This capacitance could be calculated by the following equation [47, 48]:

$$C = \frac{\epsilon_0 \epsilon_m A}{d} \quad \text{Equation 3}$$

where ϵ_0 is the vacuum permittivity, ϵ_m is the lipid dielectric constant, A is the area of the bilayer membrane and d is the thickness of the hydrophobic region. This lipid membrane is also expected to have some defects causing some ions leakage I_m and this is leading to a result that the membrane has an intrinsic resistance R_m [47]. This leakage also, could be simulated by electroporation process [49]. This happens when a certain higher voltage is applied to the bilayer. Such higher voltages are creating pore-like channels from which some ions are crossing the bilayer. [48, 50, 51]. These pores are reversible as they deformed again once the higher applied voltage drops to normal [49]. Due to its effect in the elasticity of membranes, cholesterol was found to decrease the

membrane electroporation [44]. The structure of lipid molecules is affecting the size, shape, and stability of the formed pore, in other words, formed pores are not identical for all lipid types. Factors like surface tension γ , bilayer tension Γ and voltage applied U are affecting the critical radius r_c of the pore according to the following equation:

$$r_c(U) = \frac{\gamma}{\Gamma + \frac{\epsilon_e - \epsilon_m}{2d} U^2} \quad \text{Equation 4}$$

where ϵ_e is the dielectric permittivity of the aqueous medium, ϵ_m is that of the lipid membrane and d is the membrane thickness [52]. With applied voltage and increasing hole radius also the free energy of the membrane W is changed and affected by the critical radius r_c according to the following equation [50]:

$$\Delta W(r, U) = 2\gamma\pi r - \Gamma\pi r^2 - \frac{(\epsilon_e - \epsilon_m)\pi r^2}{2d} U^2 \quad \text{Equation 5}$$

1.1.4. Lipid Membrane Tension

The density of lipid molecules in a membrane can be define as lipid packing. This lipid packing is affected by membrane curvature and the molecular shape of the lipid molecules [53, 54, 55]. Any decrease in such density is considered as ‘Lipid Packing Defects’. Lipid membrane tension is very important factor as it is affecting the stiffness and stability of lipid membrane [56]. High membrane tension was found to increase the lipid packing defects [53]. In addition, the increase in membrane tension is also decreasing the membrane thickness but increasing the membrane area, volume and other parameters such as hydration depth and hydration thickness [54]. As mentioned before, the lipid bilayer is formed when two aqueous fingers decorated by lipid monolayer come in contact with each other (fig. 7). The formed membrane has a tension Γ expressed by the following equation [43]:

$$\Gamma = 2\gamma \cos \theta/2 \quad \text{Equation 6}$$

where Θ is the angle of the bilayer at the water/oil interface and γ is the surface tension of a lipid monolayer.

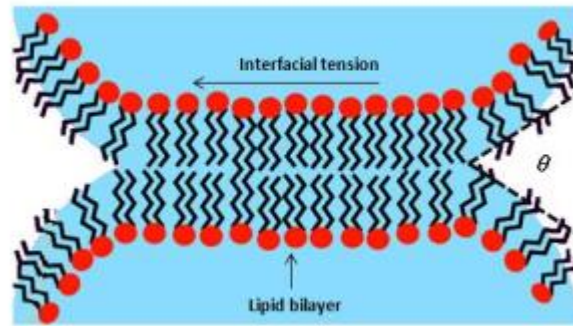


Figure 7: Two lipid monolayers are contacting to each other to form a lipid bilayer membrane. θ is the angle formed at the interface between the aqueous and non-aqueous phases. Self-Drawing

The interfacial tension could be determined by measuring the energy (change in free energy ΔF_E , equation 7) needed to form the membrane with respect pressure differences on both sides of the bilayer and also the curvature of the membrane [57]. Once the membrane tension is being calculated, it is possible to calculate the change in free energy ΔF_E to form a bilayer from two monolayers, under constant temperature, according to the following equations:

$$\Delta F_E = \Gamma - 2\gamma = 2 \Delta\gamma \quad \text{Equation 7}$$

$$\Delta F_E = 2\gamma ((\cos \theta/2) - 1) \quad \text{Equation 8}$$

From the above equations, the free energy could be defined as the amount of work was gained from the bilayer formation [57].

1.1.5. Mechanisms of membrane fusions

As a definition, membrane fusion (fig. 8 and 9) is the process by which two separate lipid membrane of two different cells fuse or merge together to form a single lipid membrane [58]. Fusion is classified into two types; *heterotypic*, when a membrane fuses with non-similar compartment or *homotypic*, when similar compartments fuse together [58, 59]. This fusion is happening as kind of communication between the two cells as mentioned in the introduction. The most studied fusion event is the *exocytosis* process where vesicles fuse with the cell membrane in order to release their content outside or even to embed some receptors, channels or transporters in the cell membrane. The lipid composition is the key in lipid membranes fusion [34]. In the case of pure lipid

membranes, there are experimental evidence to membranes that have not fused over long time despite being in contact. [58]. Fusion process is not spontaneous; it could be derived by different proteins, ions or charged lipids [58, 37].

Fusion is not a one-step process, there are certain steps called fusion intermediates or pores before the end stage. It could be divided into six major steps but of course each step is a series of minor steps [60]. Firstly, the involved membranes must reach a certain approach to each other in the range of few nanometers; this is called *tethering* (fig. 9, 1). Secondly, due to the first approach, *docking* takes place by reaching the optimum orientation between molecules. (fig. 9, 2).

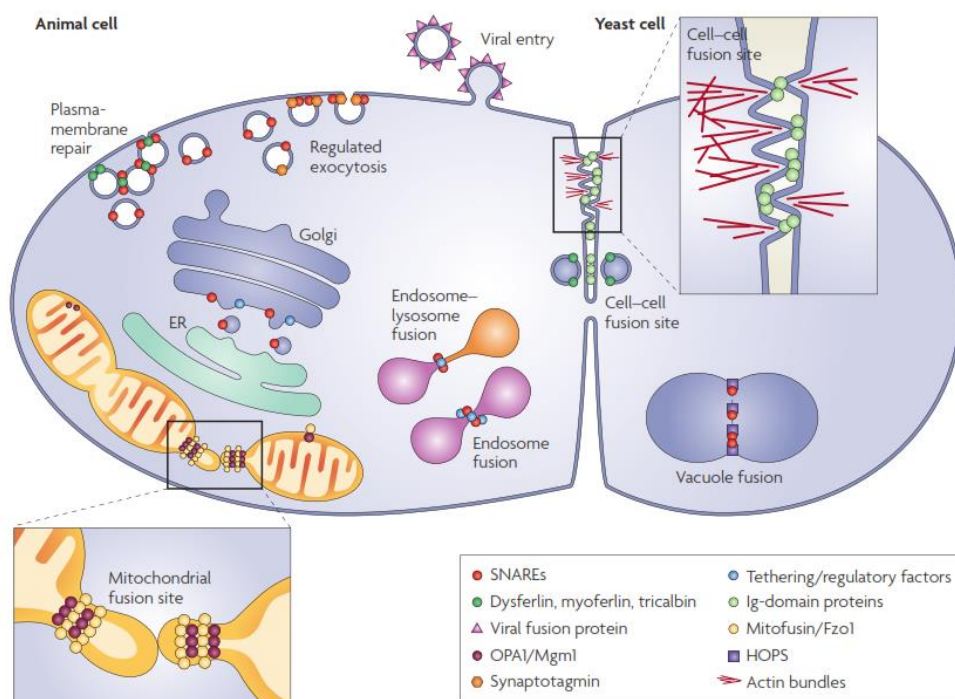


Figure 8: Different fusion events occurring in one cell or between different cells. Copyright 'Springer Nature 'Approved, Licence number 4855840801407 Martens, S., McMahon, H. Mechanisms of membrane fusion: disparate players and common principles (McMahon, 2008)

For the second step to be achieved, a drainage of the aqueous phase between the two membranes must take place; this is also could be defined as dehydration between the two membranes. The third step (fig. 9, 3) is destabilization or localized rearrangement in one point between the two membranes to initiate the fusion process. Consequently, (fig. 9, 4), such initiative fusion grows leading to mixing of the outer

layers of the two membrane and then diffuse starting from the point of contact forming a *stalk* or *hemi-fused* area [61].

After hemifusion, the opening of the pore is growing (fig. 9, 5) and the contents of both internal layers of the membranes would mix together in this case (fig. 9, 6) [60, 61, 62].

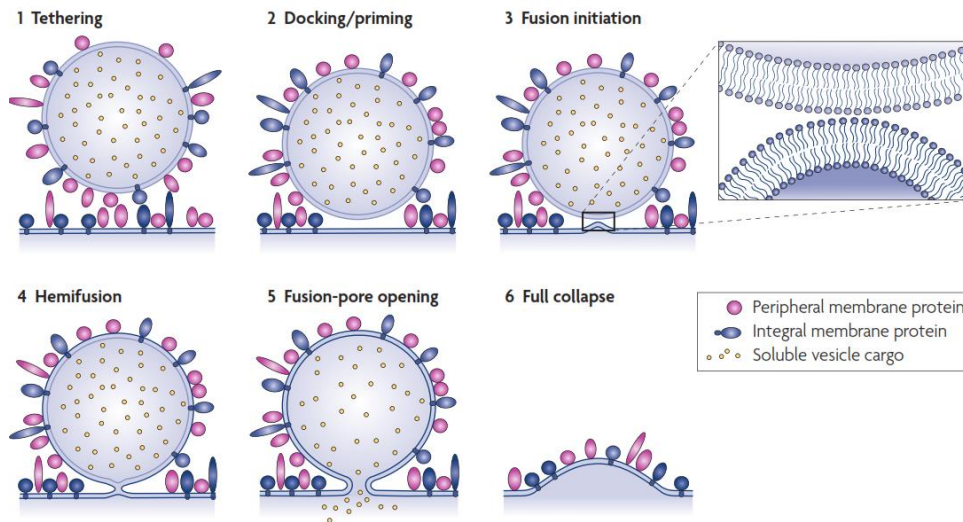


Figure 9: Fusion of two lipid membranes: (1) Two lipid membranes (2) A rearrangement in one point initiating the fusion (3) Fusion between the two lipid membranes forming a stalk (4) Hemifusion state (5) Full fusion state (6). Copyright 'Springer Nature' Approved, Licence number 4855840801407 Martens, S., McMahon, H. Mechanisms of membrane fusion: disparate players and common principles (McMahon, 2008)

Another issue that is affecting the fusion process is the degree of curvature of a membrane [63]. The normal curvature of a lipid bilayer is related to a mean curvature H^B of both inner H^{in} and outer H^{out} monolayers. This could be solved using the following equation [61]:

$$H^B = H^{out} - H^{in}$$

Equation 9

From the above equation, lipids with inverted cone shape have a positive curvature (+ve H^B). On the other hand, lipids such as unsaturated PE; molecules have cone-like shape, have a negative curvature (-ve H^B) formed monolayers. This is the reason why PE is added to enhance the fusion of artificial liposomes. Cylindrical-shaped lipid molecules such as PC, are tending to form almost flat monolayers [61].

1.1.6. Driving Forces for membrane fusions

In the previous section, we demonstrated the mechanism of lipid membrane fusion. Also, we have mentioned that the fusion process is not spontaneous. The process to bring the two membranes in apposition and very close to each other in order to start the fusion requires energy in order to overpass the repulsive forces of charged lipid [58]. The main studied system is PC-PS vesicles fusion [64]. PS lipid is charged negatively, and so, repulsion takes place in the process of fusion. To overcome this phenomena, it's studied and proved that divalent cations especially Ca^{+2} and Mg^{+2} , together or separate, are forming a complex with the negatively charged PS and so facilitate the fusion process [64]. Due to such mechanism, these divalent cations are noun as fusogenic molecules. Not only Ca^{+2} and Mg^{+2} but also other cations like Mn^{2+} , Zn^{2+} , La^{3+} , Sr^{3+} and H^+ [65]. Other examples for fusogenic molecules include organic molecules such as n-hexyl bromide and short chain alcohols by induction of inverted hexagonal (H_{II}) phase formation in which a negative curvature takes place [66].

Rather than molecules that are involved in fusion events, there is a protein family which is mostly involved and widely studied in membrane fusions; SNAREs [58, 67]. SNAREs refers to soluble *N*-ethylmaleimide-sensitive factor (NSF) attachment protein receptors [58]. It is a family of more than 60 protein members in humans [68]. According to their locations; vesicles or target membrane, SNAREs are simply divided into two main categories, V-SNAREs and T-SNAREs [69]. A most recent studies have found that several SNAREs are localized in both vesicles and membranes and as a result they have changed the abbreviations from T- to Q-SNAREs (*glutamine containing SNAREs*) and V- to R-SNAREs (*arginine containing SNAREs*) [67]. The T-SNAREs are Syntaxin and SNAP-25 where the V-SNAREs members like synaptobrevin or VAMP [61, 67]. In Figure 11 [67], a very simple illustration for *exocytosis* event operated by SNAREs complex and what happens after such event. There is a protein member that is attached to *Syntaxin* which is 'n-Sec1' and it is regulating the *Syntaxin* machinery (Figure 10). This association; between Syntaxin and n-Sec 1, is preceding the SNARE-complex core formation and a 'dissociation', between them, happens at the start of the fusion allowing the next step which is binding between *SNAP-25*, *Syntaxin* and *VAMP*, also called 'Nucleation'. The nucleation is happening between *SNAP-25*, *Syntaxin* and *VAMP* and

it just need one coil to withdraw and start the fusion between the two membranes [70] [71]. Such complex is formed of one coil between *VAMP* and *Syntaxin* and two coils of *SNAP-25* and is called a four-strand-coiled structure [67]. After the first coil is being drawn, starts the role of Ca^{+2} in triggering the fusion process until it is finished by the release of the neurotransmitter or generally the vesicle content. In the cytoplasm, there are α -SNAP and NSF are ready to start dissociating the SNARE-complex in the three components again: *SNAP-25*, *Syntaxin* and *VAMP*. By this step the recycling of vesicles start and become ready for another exocytosis event [67, 72].

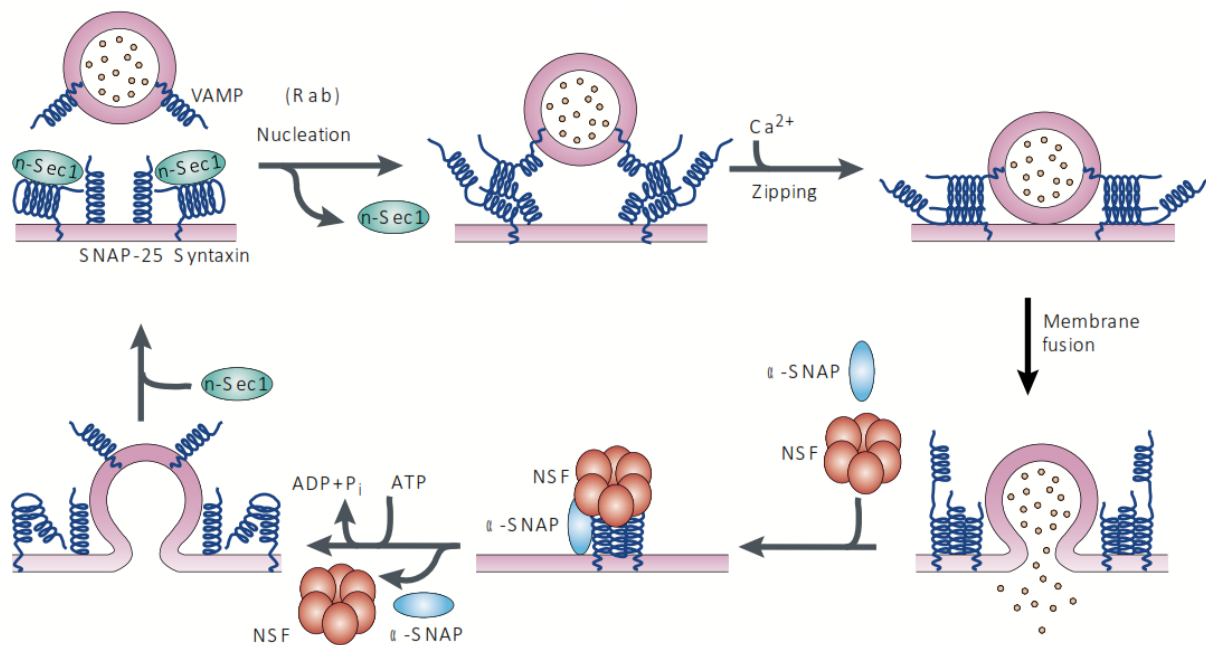


Figure 10: Illustration diagram for exocytosis event. The process starts when the *n-sec1* is being released from the *Syntaxin*. After that, the fusion process starts through withdrawing and coiling to form a four-strand-coiled structure. Consequently, the two membranes fuse together and the vesicle releases its content to start to recycling steps. Due to presence of α -SNAP and NSF in the cytoplasm of the presynaptic area, dissociation of the three SNARE-complex components and VAMP attaches again to a new synaptic vesicle to start a new cycle. Copyright licence approved 4855850549088 SNARE-mediated membrane fusion Yu A. Chen et al 2001 (Scheller, 2001)

1.2. Structure and Physiology of Neuronal Synapse

Information transmission through the central nervous system happens in the form of action potential or nerve impulse from one nerve to the next. This action potential is through the axon is propagated by the myelin sheath; nerve-insulator layer, surrounding the nerve axon [47]. Neurons or nerves are not continuous through our body but connecting to bridge large distances. The gap or the link between neurons is defined as *synapse* (fig. 12). Synapses are connection parts between neurons and each other or between neurons and cells and they are very important for neurons to achieve their functions [73].

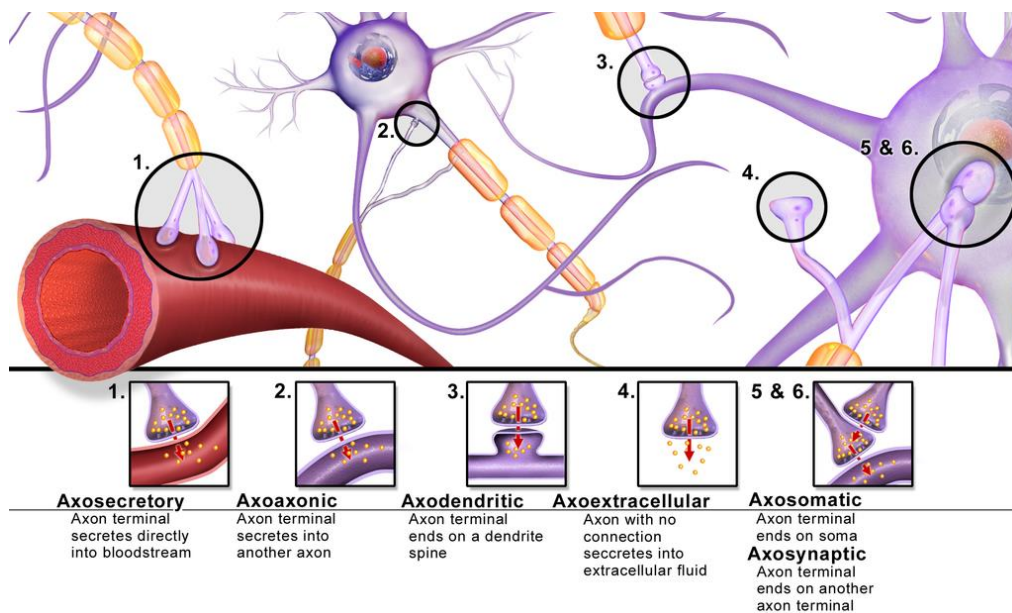


Figure 11: Illustration of neuronal structure and synapses. The diagram is showing different structures of synapses according to their location. Copyright © 2013 Wikipedia. CC BY 3.0. This work is licensed under a Creative Commons Attribution 3.0 Unported License. (Blaus, 2013)

1.2.1. Types of Synapses

According to nerves structures (fig. 11), the axon of neuron can synapse with another axon, dendrite, body cell or blood vessels [74]. Based on the previous classification synapses are named neuro-neuronic synapses, neuromuscular synapses

and neuroglandular synapses. The neuro-neuronic synapses can be sub classified into axo-axonal, axo-dendrite and axo-somatic synapses according to their sites [75, 76].

Synapses can be classified according to their functions or according to their structure. According to their functions, synapse could be divided into three main types; chemical synapse, electrical synapse and immunological synapse [77]. Almost all synapse in the central nervous system consist of chemical synapses [73]. A neuron secret a neurotransmitter; ions, to act on the subsequent neurons' receptors (fig. 12) [73].

The action could be inhibitory or excitatory and it is a *one-way* action [78]. Examples for such chemical transmitter includes; acetylcholine, epinephrine and histamine [73]. Electrical synapses are characterized by transporting ions from the interior of one cell to another [77]. Immunological synapses represent the connections between antigens and cells.

1.2.2. Relation between Anatomy and Physiology of Synapses

In Figure 12, a basic structure of a synapse showing the presynaptic area and postsynaptic area and in between the synaptic cleft [73, 79]. In the presynaptic area, two main components are present: the synaptic vesicles and mitochondria. The synaptic vesicles contain the neurotransmitter proportional to the size of the synapse itself and might be excitatory or inhibitory according to the function of the nerve [80]. The mitochondria are the power house of any cell, in which adenosine triphosphate (ATP) is formed [81]. This energy is consumed in the synthesis of transmitters [73]. As mentioned before (fig. 11), the movement of the pulse is started with action potential, which creates a depolarization state across the axon and until the dendrites causing the synaptic vesicles to be directed to the synaptic gap and release their content [82]. Precisely (fig. 12), the presynaptic membrane contains *voltage-gated calcium channels* [20]. When the action potential reach this membrane, these channels are opened and Ca^{2+} flux into the presynaptic area [79, 71]. Ca^{2+} ions bind to the release site through proteins and this binding leads to opening these gates or release sites [18]. The amount of synaptic vesicles released is proportional to the amount of in-fluxed Ca^{2+} [73, 71].

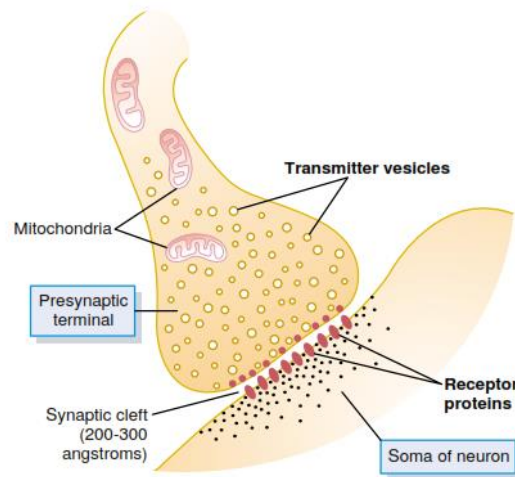


Figure 12: Illustration diagram for a chemical synapse showing the neurotransmitter in the presynaptic area (on top) ready to be released towards the receptors in the post synaptic area (below) through the synaptic gap. Copyright "Textbook of Medical Physiology 11th Edition. by Arthur C. Guyton and John E. Hall. Unit IX: The Nervous System: A. General Principles and Sensory Physiology; P. 560. Fig 45-6 Copyright Elsevier (2006)."

The postsynaptic membrane (fig. 13), contains many of receptor proteins. These receptors (fig. 13) are divided into two components: binding sites and ionophore components. The binding site is responsible to bind to the neurotransmitter released from the presynaptic area. The ionophore part is a compartment and could be in the form of an ion channel or a second messenger activator. [73].

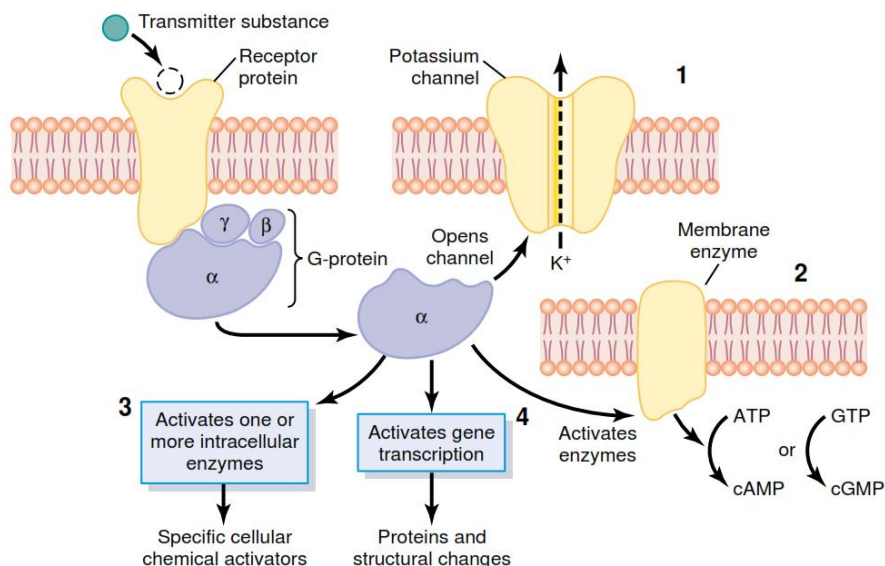


Figure 13: Illustration for the postsynaptic membrane protein-receptors with focus on the roles of the second messenger activator. (1) The activation of K^+ ion channels in the postsynaptic membrane (2) cAMP or cGMP activation (3) Activation of intracellular enzymes (4) Gene transcription activation. Copyright "Textbook of Medical Physiology 11th Edition. by Arthur C. Guyton and John E. Hall. Unit IX: The Nervous System: A. General Principles and Sensory Physiology; P. 561 Fig 45-7 Copyright Elsevier (2006)."

Ion channels are two types, cation channels and anion channels. The cation channels are allowing sodium ions (also some potassium and calcium) to flux in [18]. This happens because these cations channels are lined with a negative charge responsible for attraction of positive ions and repulsion of anions [73]. The anion channels are responsible for the influx of chloride molecules. The opening of the cationic channels and influx of positive charge is exciting the neuron (*i.e. creating action potential*) that is why transmitters which are responsible for opening the cationic channels are known to be *excitatory transmitter* [83]. On the other hand, the entrance of negative charges to the postsynaptic area is inhibiting the neuron and so the transmitter causing such influx are known to be *inhibitory transmitter* [83]. Such activation or inhibition needs sub-milliseconds and this is not suitable in case of memory-function of the nervous system [77]. Here comes the role of the second messenger activator in postsynaptic prolonged activation. One of the most important second messenger activator is the G-protein which consists of three subunits alpha (α), beta (β) and gamma (γ) [18, 84]. The α -subunit is attached to receptor protein where both β and γ are attached to the α -subunit. After impulse activation, the α subunit separate from the β and γ subunits and move in the cytoplasm to start performing other four crucial roles [73] [84]. These roles could be summarized in (fig. 13). One role is activation of certain ion channels in the postsynaptic membrane like k^+ ion channel which keep opened for prolonged time [18]. The second role is activation of cyclic adenosine monophosphate (*cAMP*) or cyclic guanosine monophosphate (*cGMP*) which are crucial in leading metabolic changes in the neuron leading to changing in neuron structure and in turn its excitability [73, 84]. The third role is intracellular enzymes activation which are essential for chemical functions. The last role is gene transcription activation which is a long-term process can cause new proteins formation inside the neuron which subsequently change the metabolic processes and structure of the neurons [73, 85].

1.2.3. Consequences of Vesicles fusions and Vesicles recycling

New transmitters, especially small molecules, are synthesized in the cytosol of the presynaptic area by the existing enzymes [73]. After their formation, these transmitters are being absorbed inside the synaptic vesicles [80]. The release of

neurotransmitter and the action on postsynaptic receptors only need less than or equal to a millisecond for each process [82]. Synaptic vesicles are recycled again after fusion (fig. 14) [86] with the presynaptic membrane and releasing their contents in the synaptic cleft [73, 87]. After fusion, the synaptic vesicle membrane becomes part of the presynaptic membrane, but after seconds or maximum minutes, it introverts again to form a vesicle swimming in the cytosol of the presynaptic area; *kiss & Run theory* [87]. The membrane of this new vesicle contains needed lipids and enzymes to synthesis or to uptake its specific neurotransmitter [73]. One clear example for fusion and recycling process is *Acetylcholine* (Ach). This neurotransmitter is synthesized in the presynaptic area from two components (*Acetyl coenzyme A* and *Choline*) thanks to *choline acetyltransferase* enzyme [88]. After that, A.ch. is transferred inside the vesicles ready for the fusion moment. After fusion and release in the synaptic cleft, it splits again into *acetate* and *choline* thanks to *cholinesterase* enzyme of the *proteoglycan reticulum* [73]. The choline part is returned to the presynaptic cytoplasm to start a new Ach-synthesis cycle [88, 73].

1.2.4. Electrophysiology of Neurons during Excitation and Inhibition

After a series of excitation and inhibition, the nerve must reach a rest state and the potential in this case is called a resting potential (fig. 15a) [73, 89]. To explain this reversible, spontaneous process, we must consider a specific nerve type as it is slight different according to the site and size of neuron [73]. The resting potential of spinal motor nerve is -65 mV.

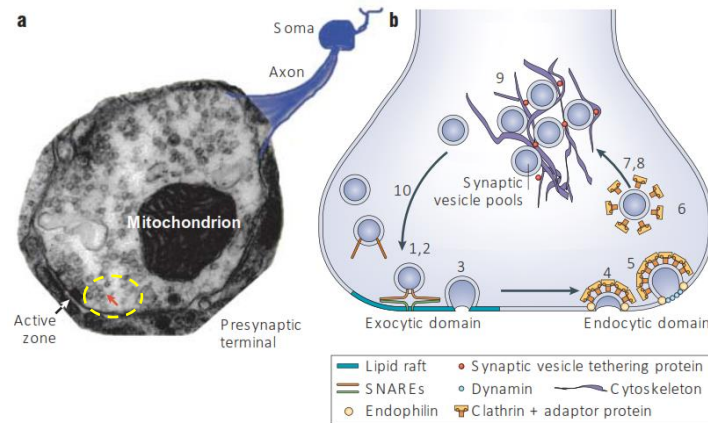


Figure 14: synaptic vesicle exocytosis and endocytosis. (a) An electron microscope image for a presynaptic terminal of *Drosophila melanogaster* showing small synaptic vesicles inside the yellow circle. (b) A life cycle of vesicles starting from SNARE-mediated fusion, transmitter release, endocytosis and filling with transmitter and finally attaching to V-SNAREs for another exocytosis event. Copyright Springer Nature licence number 4855860257106' (Rohrbough, 2005)

Such lower voltage is essential in controlling excitation or inhibition processes of neurons; decreasing such negative voltage is responsible for neuron excitation and vice versa [73]. During excitation (fig. 15b), by excitatory transmitter, the influx of Na^+ inside the neuron body, causes the resting potential to increase in the positive value from -65 to -45 mV [89]. This will create action potential in the excited neuron (figure 15 b). After such excitatory event, the neuron starts the way to return to its normal resting potential through inhibitory synapses (fig. 15c). Due to the less negative potential inside the neuron body, the inhibitory synapses open the Cl^- channels by release of inhibitory substances [90]. Not only Cl^- influx but also K^+ efflux outside the postsynaptic area reaching a potential of -70 mV [73]. This situation is called *hyperpolarization* and this leads to neuron inhibition due to higher negative potential [89]. In addition to such postsynaptic inhibition, there is a presynaptic inhibition caused by a chemical transmitter called *gamma aminobutyric acid* (GABA) [91]. GABA is released on the outside of the presynaptic nerve endings before their contact area with the postsynaptic nerves [73, 91]. This leads to opening anion channels and consequently influx of anions in the terminal part of the presynaptic nerve leading to inhibition of transmission caused by influx of positive charges during the action potential [91].

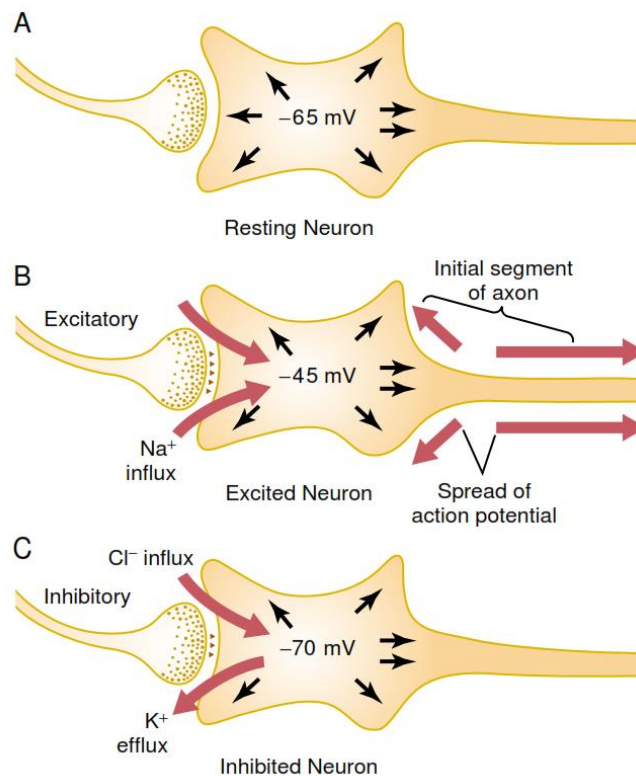


Figure 15: Illustration diagram for different nerve potentials. (A) Is a showing the rest potential of spinal motor nerve (B) is a potential inside the soma after nerve excitation (C) is the inhibition potential following the excitatory events. Copyright "Textbook of Medical Physiology 11th Edition. by Arthur C. Guyton and John E. Hall. Unit IX: The Nervous System: A. General Principles and Sensory Physiology; P. 566. Fig 45-9 Copyright Elsevier (2006)."

1.2.5. Factors affecting Synaptic Transmission

After *long-term excitation* or *over excitation* of a nerve, a situation called 'fatigued synapse' can take place which in severe cases could leads to medical disorders like schizophrenia, retardation or neurodegenerative diseases, for example, a medical case called *Epilepsy* [92, 73]. The case of fatigued synapse is very important in explanation of epilepsy to fade away [93]. The development of such break down; fatigued synapse, after an epileptic attack is a protective mechanism for nerves [73]. Such fatigue occurs due to drainage; full or partial, of excitatory transmitter store [94]. Just exhaustion or drainage can take place in seconds or minutes maximum. In addition to such exhaustion, two more factors are playing roles in such fatigue of the postsynaptic area such as inactivation of membrane receptors or stop over-concentration development of ions inside the cytosol [73]. There are other medical situations are leading to such fatigue. Two of these medical situations are *acidosis* and *alkalosis*. In case of *acidosis*

(blood pH below 7, normal is 7.4), it may lead to coma (loss of consciousness) due to under excitability of nerves like in *diabetes* [73, 95]. On the other hand, in case of *alkalosis* (blood pH above 8), the excitation of nerve is very high and may predispose epilepsy [95]. Another medical aspect is *Hypoxia*, which could in 3 or 7 seconds lead to loss of consciousness due to lack of oxygen which is crucial in neurons excitability [73] [96]. Moreover, some drugs are found to have a direct effect on nerve excitation (like *caffeine* and *theobromine*) or inhibition (like anaesthetics) [73].

1.3. Patch Clamp Techniques

Electrophysiological measurement techniques: such as *patch clamping*, are widely used in studying biological process of cells such as ion transfer, testing ion channels in membrane-like models and so on. In our study, we have used such measurements to check the formation of artificial lipid membranes and ion transfer studies. In simple words, “**Patch**” refers to a small piece of the cell membrane and “**Clamp**” explains the electrical behavior involved in the technique [97, 98]. Patch clamping is considered a unique technique allowing researchers to manipulate, in a quantitative manner, cell membrane voltage and measure electrical current flowing across a membrane. Two main applications are being applied by the patch clamp; the first one is “**Voltage clamping**” in which a defined voltage is being applied to a patch of the membrane to measure the resulting current and consequently calculation of the patch conductance [98]. The second application is “**Current clamping**” and its purpose is to measure voltage across the patch [99]. In “Voltage clamping”; many types of channels are being involved to measure ions flow such as voltage-operated ion channels (*e.g.*, Na⁺, K⁺, Ca⁺⁺ and Cl⁻ channels) [98, 100]. Another examples for channels including second messenger activated channels (*e.g.*, cAMP, cGMP, G proteins as well as phosphatases and kinases) [101, 102]. Also, neurotransmitter activated receptor-operated channels (*e.g.*, ligand gated receptors and G protein coupled receptors) [103, 104]. One example for “current clamping” is membrane potential measurement. This happens by introducing currents, through the electrodes, to the cell and record the voltage generated due to the stimulation [105].

Beside the previously mentioned techniques, scientist had developed more innovative applications mentioning here only “**Capacitance measurements**”, main technique in this thesis. This application is allowing us to accurately measure the thickness of solvent free membrane; and consequently, its area, and to detect exo- and endocytosis; vesicle fusions. For example, the exocytosis was found to increase the capacitance value reflexing the increase in the membrane area. On the other hand, drop in capacitance is a proof of reduction or perforation in the membrane leads to leakage of the capacitive charges [106, 107, 108].

1.3.1. Patch Clamp configurations

Figure 16, is showing all configurations used in either single ion channel recording or whole cell recordings [109]. All patch clamp techniques use “electrode” *i.e.* patch electrode. This electrode is introduced to the system as a glass pipette contains a wire inside. The tip of the electrode is attached to the cell membrane so tightly forming the “giga-seal” (i.e. the resistance between the inside and the outside of the pipette is more than $10\text{G}\Omega$). The small membrane inside the tip of the pipette; the patch membrane, is then being applied to voltage clamping to detect ionic current passed through the membrane patch. Some variations on the patch clamp techniques had been introduced [99, 98].

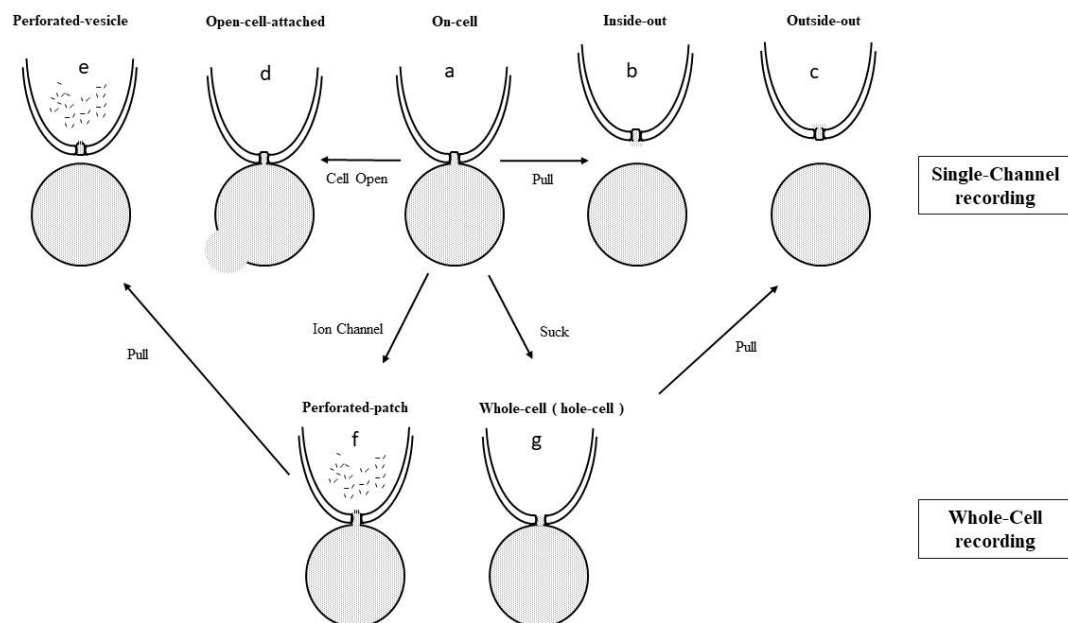


Figure 16: Patch Clamp mode variations. In the upper row, a schematic diagram for single-channel recording with the 2 possible changes that could be done to reach inside-out or open-cell-attached configurations. Whole cell recording configurations. Starting from the upper middle configuration; On-Cell, and by applying modifications to the electrode or the cell itself, all other configurations have been developed to different measurements techniques and for over-passing limitations of the first technique. Self-drawing

In the next few pages, a brief description for each technique with advantages and disadvantages of each techniques. First starting with the Single-Channel Recordings which includes five configurations; on-cell mode, inside-out mode, outside-out mode, open-cell-attached mode, and perforated-vesicle mode.

a. Cell-Attached Mode (On-Cell Mode in HEKA amplifier)

Figure 16a, is the initial configuration mode. It is formed by obtaining the giga seal. In this mode, channel activity is observed with minimum disturbance of the intracellular environment [98]. The main drawback of this configuration is that the resting potential of the cell is unknown as there is no information on the intracellular membrane potential and so the intracellular conditions cannot be controlled [97].

b. Inside-Out mode (In-Out Mode in HEKA amplifier)

Once the giga-seal formed as in the previous mode, the pipette is being withdrawn from the cell resulting in excision of membrane patch with its cytoplasmic side facing the bath solution or the external media in general (fig. 16b). The main advantage in this mode is the accessibility to the intracellular surface of the membrane. By the previous step, it is possible to change the bath solution composition to study its effect of an ion channel in the isolated membrane patch [99]. The disadvantage of this configuration is that, the cytoplasmic components of the original cell are being lost which are essential in observing the behavior of the ion channel [97].

c. Outside-Out mode (Out-Out Mode in HEKA amplifier)

Once you obtained the whole cell mode, will be discussed in the last configuration, slow withdraw of the pipette away from the cell will lead to stretching in the membrane and breaking by the end (fig. 16c). Then the membrane reseals, and the intracellular face is now in contact with pipette solution. This mode, the extracellular condition can be varied and any agent could be tested to exam its effect on the channel activity [98]. On the other side it still has some limitations like as in the previous configuration, cytoplasmic components are being lost which are essential in observing the behavior of the ion channel.

d. Open Cell-Attached Inside-Out Mode

In this mode, part of the cell membrane is being ruptured (fig. 16d). This part is away from the tip of the patch pipette. So, in this technique, it is possible to perfuse

components or control the intracellular environment of the cell. It still showing a limitation in perfusion speed due to the size of the hole [97].

e. Perforated Vesicle Outside-Out Mode

This configuration could be done subsequently to a whole-cell configuration. By attaching the electrode to a membrane and creation of hole by applied suction and then pulling the pipette. This leads to formation of two strips of the membranes attached separately to the margin of the pipette. These two strips attach to each other later to form a vesicle. (fig. 16e).

The next two techniques are dedicated for *whole-cell* recordings and two configurations: *perforated patch* mode and *whole-cell* mode.

f. Perforated Patch Mode (Slow Whole-Cell Mode)

In this mode, it is possible to prevent the washout of important components of the cytosol as there is no rupture for the membrane as illustrated in the diagram. This is achieved by adding artificial ion channels (fig. 16f) (*e.g.* monovalent cation channel-forming antibiotics; ionophores such as “Nystatin” and “Amphotericin B”) to the pipette solution. As long as there is no rupture in the membrane and consequently no loss in cytoplasm, this cell is considered to be “intact cell” and this is allowing voltage- and current-clamping [110, 111, 112]. The limitations of this techniques are in series resistance which is higher and so voltage-clamping which is slower than the classical “Whole-cell mode”.

g. Hole Cell Mode (Conventional Whole-Cell mode)

Instead of withdrawing the pipette away from the membrane, here, the membrane patch between the pipette and the cytoplasm is broken by the application of gentle suction pulse (fig. 16g). Now, intracellular components are being dialyzed with the pipette solution and so the total current across the whole membrane can be recorded. This configuration enables us to record the membrane current “*Voltage Clamping*” and to manipulate and measure the membrane potential “*Current Clamping*” [113]. Limitation of this configuration is in washing out of some cytosolic factors which would

come up and consequently affect the ion channel activity. Due to lower resistance and physical unity between the pipette lumen and cytosol, this is the mode we use for our capacitance measurements.

1.3.2. Electrical Equivalent Circuit (Principles of Patch-Clamp recordings)

Exocytosis and Endocytosis are crucial processes in our experiments, so we used the configuration “Whole-Cell” which, allows as to detect such processes through capacitance measurements. In this section, we explain the equivalent electrical circuit (fig. 17). [114]

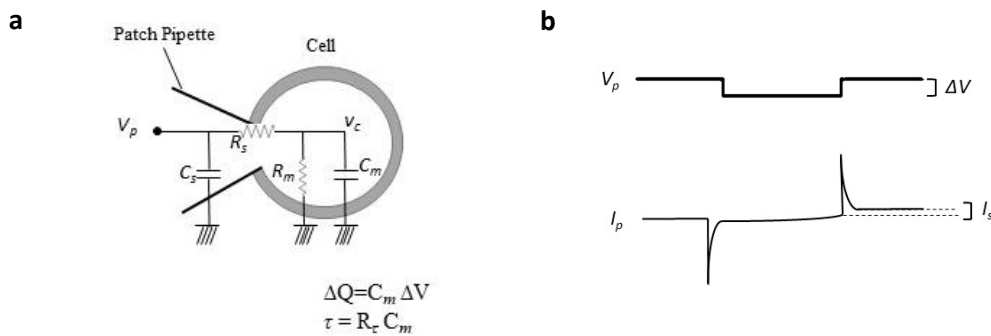


Figure 17: (a) Whole-Cell patch recording (b) Whole-Cell capacitive current recording in response to hyperpolarization pulse ($\Delta V = 10$ mV). Self-drawing

Biological cells contain a very good conductive electrolytes (cytosol) which separated by thin (Nano-range), low- conductive membranes contains ion-channels which are electrically conductive [99]. The biological membrane of a cell includes models for membrane capacitance and resistance, and a model for electroporation. The cell can be modeled by a capacitor and a resistor in parallel (*Parallel Cell Circuit*) of electrical circuit. The membrane is modelled as capacitor and Ohmic resistance in parallel and in series to that we have the micropipette (respectively the ion conductivity) that can be modelled as Ohmic resistance. In a steady state, the membrane potential is held constant, represented by the following relation:

$$V_c = \frac{R_m V_p}{R_m + R_s} \quad \text{Equation 10}$$

where V_c is the intracellular potential, V_p is the electrode potential, R_m is the membrane resistance and R_s is the series resistance between the electrode and the cell. If we applied

a square pulse (ΔV) through the equivalent circuit and considering $R_m \ll R_s$, the current response is represented by Ohm's law [99]:

$$I_{in} = \Delta V / R_s \quad \text{Equation 11}$$

$$I_s = \Delta V / R_m \quad \text{Equation 12}$$

Electrical stimulation of the membrane causes a change in membrane potential which is counteracted by the activation of voltage-dependent ion channels. In case of no ion channels, the rate of changing of lipid membrane potential is controlled by the membrane capacitance C_m with time constant τ explained by the following equation:

$$\tau = R_\tau C_m \quad \text{Equation 13}$$

$$R_\tau = (R_m R_s) / (R_m + R_s) \quad \text{Equation 14}$$

when the specific membrane resistance is constant: $R_m \propto 1/A$ where A is membrane area. Now we can conclude that specific membrane resistance is dependent on the membrane potential.

1.3.3. Capacitance Measurements Technique for lipid bilayer

Electrical model of a cell membrane is divided into a capacitive and a resistive component. In other words, the ion permeation property is representing the resistive component while the electrical capacitor is represented by the lipid bilayer of the cell [115]. The capacitor magnitude (C_t) is proportional to the area of the membrane (A_m), represented by the following equation:

$$C_t = \frac{\epsilon_o \epsilon_m}{d_m} A_m \quad \text{Equation 15}$$

where, ϵ_o is the effective membrane dielectric coefficient ($= 8.854 \cdot 10^{-12} \text{ F/m}^2$), ϵ_m is dielectric constant (≈ 2.2) and d_m is the diameter of the lipid membrane. The micropipette has intrinsic capacitance that in the range of several pico-farads, but it is compensated by the patch amplifier. The unit capacitance (Also known as specific capacitance) is about $1 \mu\text{F}/\text{cm}^2$. Due to Endo- or Exocytosis, the membrane area increases or decreases and so the capacitance.

Two main techniques for recording capacitance are briefly mentioned:

a. Capacitive Surge Measurements (Time-Domain Technique)

Under Whole-Cell configuration, after the application of a square voltage pulse (V_0), the time course of a slow capacitive transient generated is represented by the following equation [116]:

$$I_t = [V_0/(R_m+R_s)] * [1+(R_m/R_s) \exp(-t/\tau)] \quad \text{Equation 16}$$

where $\tau = R_m R_s C_m / (R_m + R_s)$ This equation is valid if R_m , R_s and C_m are not varying during the pulse. The time resolution of the real time C_m measurements depends on the record of the transient (*i.e.* it must be in a sufficient length; 5 times longer than the decay time constant).

b. Sinusoidal Excitation. (Lindau-Neher Technique)

This is the technique we have used in our measurements. Also, could be defined as “Phase-Shift” detection Method [115]. *Neher and Marty*, using Lock-In amplifier, could detect the phase shift in current signal resulted from the presence of cell capacitance when a high-frequency AC voltage had been applied. By using *Whole-Cell Mode* recordings, they have detected the increase in membrane area resulting from fusion of SUVs as increase in cell capacitance. C_m , R_m and R_s are influencing the degree of phase shift which is detected by the lock-in amplifier. When there is a change in C_m , even if small ΔC_m , the PSD can divide the current response into 2 output components: ΔC_m -dependent component and ΔC_m -independent component. The ΔC_m -independent component phase is shifted 90° (*Perpendicular*) from the ΔC_m -dependent component.

Neher and Marty, detected the most suitable “detection phase angle ϕ ” of the PSD. Using *piecewise-Linear* “simple but old-fashioned technique to measure C_m , R_m and R_s ” technique, they could observe ΔC_m associated with exocytosis. They proposed a technique to measure C_m , R_m and R_s through a software referenced to the two outputs. In our case, it is the Lock-In Amplifier in the patch clamp software. This function enables us to resolve the capacitance (C_m) and resistance (R_m) of the pure lipid membrane

and fusion events. In the few following pages, we are presenting a simple equivalent circuit have been used for capacitance measurements:

a. One Membrane Equivalent Circuit

Figure 18, it is equivalent to one simple membrane formed inside a microfluidic chip. The two monolayers are resembling the two conductive plates of a capacitor in a normal electrical circuit. The area A of the conductive plates is equivalent to the area of BLM where the d is the thickness of the BLM. Such capacitance could be calculated using equation 15.

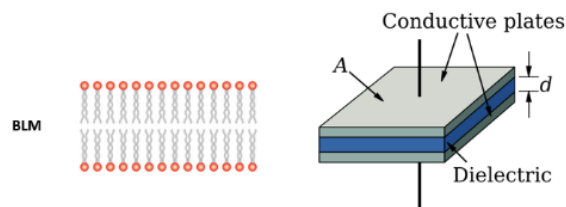


Figure 18: A schematic diagram for a BLM and equivalent capacitor. The Area ' A ' of the capacitor is the area of the membrane and the thickness ' d ' between the two plates is equivalent to the thickness of the membrane.

b. Two-Membranes Equivalent Circuit

This circuit is representing two bilayer membranes in front of each other and this could be represented by two capacitors connected in series (fig. 19).

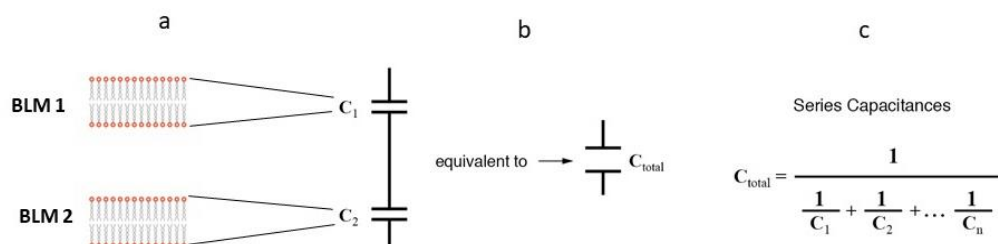


Figure 19: Schematic diagram for electrical circuit equivalent to the 2-BLMs orientation. (a) Two BLMs parallel to each other and this is equivalent to two capacitors connected in series in an electrical circuit (b). (c) The equation is simply showing the effect of connecting capacitors in series on the total capacitance. Self-drawing

As shown in the figure, the total capacitance C_{total} is fully dependent on the area of the two BLMs. In ideal situation, we consider a symmetrical area of the bilayers and as a result the C_{total} is calculated according to the equation in (fig 19).

c. Two-One Membranes Equivalent Circuit

In case we have inserted some ion channels (fig. 20a) in only one of the two BLMs, this will create a little bit complicated situation. We see two BLMs but a higher capacitance as if a single membrane is detected. This is very logic; after addition of ion channels to one BLM, it is not a capacitor anymore (fig. 20b). This results in the circuit in (fig. 20c), one capacitor and one resistor are connected in series despite seeing two capacitors connecting in series.

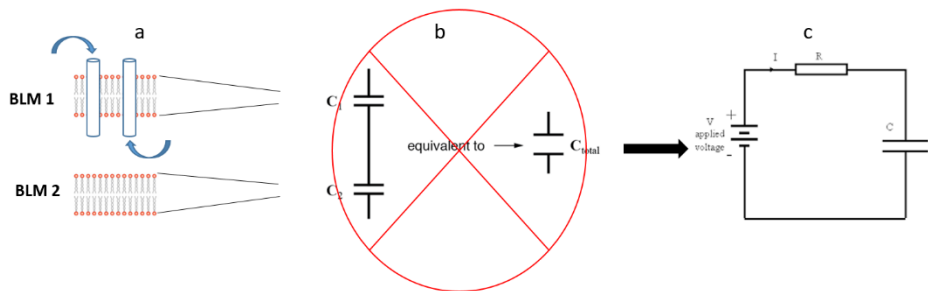


Figure 20: A schematic diagram for the situation of insertion of ion channels in one of the membranes. (a) Is showing two BLMs with ion channels in one BLM. (b) The electrical equivalent for the previous case (two membrane equivalent circuit) which is not applied in the one-two membranes equivalent circuit (c) A simple electrical circuit with a capacitor and resistor connected in series which is considered to be the equivalent modal for this situation. Self-drawing

1.3.4. Patch Clamp Amplifier

Two main amplification circuits in the patch clamp setup:

a. Current-to-Voltage Converter Mode.

The main goal of this mode is to convert small Pico-amperes currents to voltage could be processed by the software. The amplifier in this case could also be defined as “inverted operational amplifier”. It measures the small current as a voltage drop across a resistor [117]. The Main components in this mode [118] are *Feedback Capacitor* to lower the thermal noise intrinsic to resistor, *Differentiator*: to correct frequency respond

resulted from the feedback capacitor, *Switch 1* to discharge the feedback capacitor (current input) and as a result prevent the voltage to rise and to Saturate the operational amplifier and *Switch 2* which connected to a capacitor to freeze the output voltage during the function of the first switch.

b. Lock-in Amplifier.

A lock-in amplifier is consisted of “current-to-voltage convertor” and “adjustable low pass filter”. As mentioned before, it is used to extract quiet, small signals without the previously removed noise data. The devise allows to record signals quieter than the surrounding noise. From the nomenclature, it Locks to a set frequency, filter and discard the others. These high-quality noise-free signals are crucial in single fusion events[119, 120]. Simple circuit is shown below (fig. 21), it consists of *AC Amplifier* (Signal Amplifier), *Voltage Controlled Oscillator* (VCO, is an Oscillator synchronized with an external reference signal with the same frequency and phase) *Phase-Sensitive Detector* (PSD, Multiple circuit, takes in 2 voltages and produce the multiplication sum) *Low-Pass filter* and *DC Amplifier* (Output Amplifier, work at low frequencies $\leq 10\text{KHz}$)

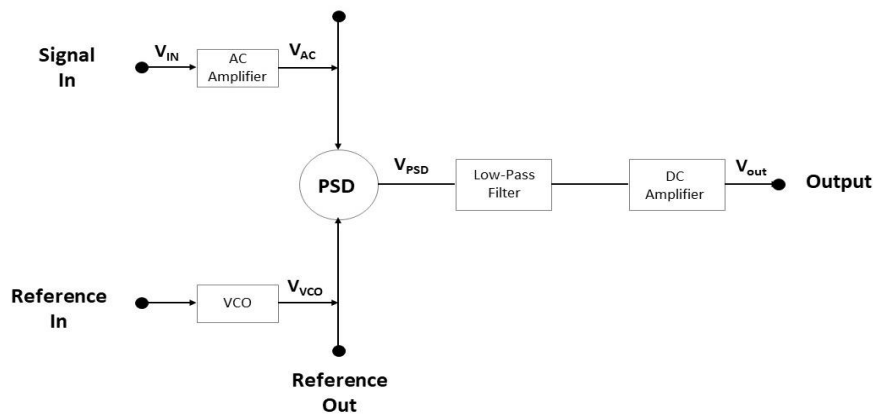


Figure 21: Illustration diagram for the lock-in amplifier showing all built-in components. Self-drawing

1.3.5. Clamp Amplifier Set-up

In our Experiments, we used EPC 10 USB Patch Clamp Amplifier (HEKA, Germany) provided with the acquisition software (*Patchmaster*). The device is equipped with a built-in AD/DA converter. The software provides a powerful data acquisition system for sampling and storage in pulse, ramp, and continuous mode. Moreover, a fully

programmed *pulse generator* and a *digital oscilloscope* are provided beside filters and amplifiers controls. This setup, including the “Lock-in” function, allowed us to record data (*Voltage and current clamping and exocytosis*) with high time resolution and low noise. The device can be synchronized with a high-speed camera (*Detailed in the next chapter*) for optical recording. The main two parts of hardware are the probe and the amplifier main unit (fig. 22):

- a. The Probe (*Head stage*) (fig. 22b). It is responsible for sample signal sampling and amplification after given stimulus. It contains a sensitive *Current-to-voltage* converter amplifier. It is also containing the components for injecting to transferring signals to the amplifier. It is important to notice that the probe is very sensitive for static electricity, so before touching it to install the micropipette or during data acquisition, it is a must to ground ourselves.

- b. The Amplifier Main Unit, (fig. 22a). It contains the power supply, the signal processing electronics, the built-in AD/DC converters, and the connectors for analog and digital input/output. Hardware calibration of the EPC 10 can also be performed in case of findings some undesirable *offsets*. This is done by a *Model Cell* (MC) provided by the company (fig. 22c). The main unit (EPC 10) has a high-quality ground for grounding additional components e.g. a microscope and a micromanipulator. Also, it is important to notice that calibration parameters are unique to each amplifier and probe, so each time changing of the probe it is a must to calibrate the amplifier. Also, before we start the calibration, it is recommended to let the EPC 10 unit to warm up between 30 to 60 min.

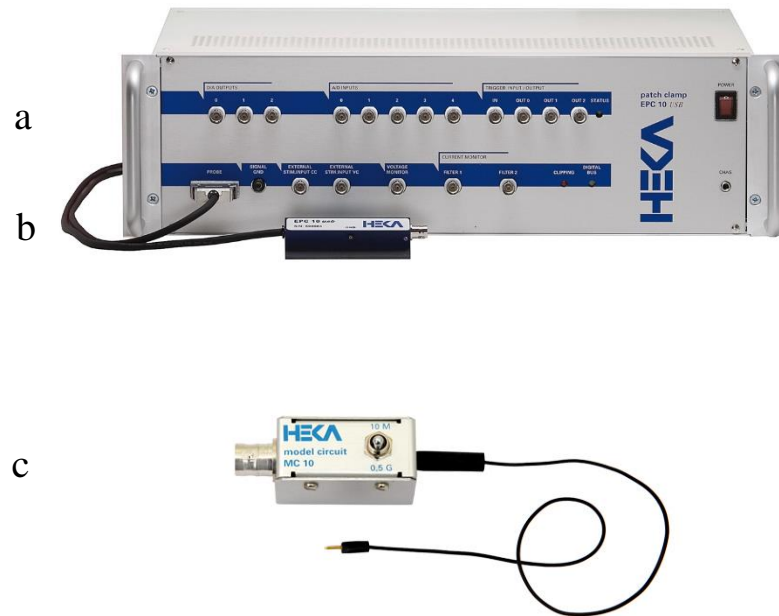


Figure 22: EPC 10 USB Patch Clamp Amplifier from HEKA. (a) The main unit, (b) the probe and (c) the model cell. (HEKA Elektronik GmbH, n.d.)

Chapter 2: Molecules, Materials and Experimental Set-up

In this chapter, we present experimental setup and an outline of all materials that have been used plus all methods that have been applied to achieve the results.

2.1. Experimental Setup

The setup (fig. 21) used to create lipid bilayer membranes and to study molecular interactions with the lipid membranes is sketched in Figure 1. It consists of an inverted microscope; Zeiss Axiovert 25, with interdisciplinary magnification objectives; 5X, 10X, 20X and 40X and a light source (i.e. Halogen). For imaging two cameras were used a CCD PCO 1600 (PCO AG, Germany) providing 30 frames per second was used to capture velocity with a maximum resolution of 1600 x 1200 pixels to record images at low light intensity. The second camera that was used is for fast image series, Fastcam SA3 (PCO AG, Germany), providing up to 2000 frames per second at a pixel resolution of 1024 x 1024. To record images (video) the software provided by the manufacturer was used, i.e. PCO CamWare and Phantom Fastcam, depending on the experimental requirements, we were choosing between the two cameras. To inject all liquids into the microfluidic chips, glass syringes with volumes of 500 up to 2000 μl (Hamilton[®], Switzerland) were used. These syringes are connected to chips by Teflon tubing. Flow was controlled by syringe pumps driven by DC motors and controlled by a software program written in LapView (National Instruments Corporation). Pumps are used to control the volumetric flow. To measure the capacitance of the formed bilayer membrane a patch clamp amplifier (HEKA EPC10, Germany) has been incorporated in the setup and is controlled by the software Patchmaster (HEKA, Germany). The connection between the amplifier and microfluidic chips is through Ag/AgCl or platinum electrodes. The Ag/AgCl electrodes were fabricated or delivered ready-made ones by HEKA (Germany).

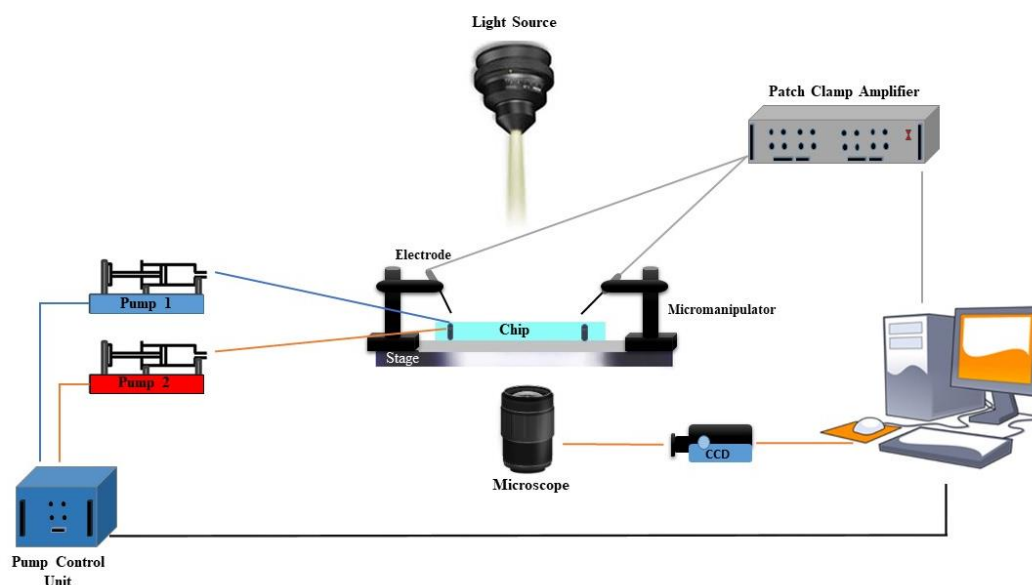


Figure 23: Experimental diagram for setup used for building artificial lipid bilayer membranes in a microfluidic platform. Self-drawing

2.2. Materials

To study artificial lipid membranes in the microfluidic chips, different lipids from two main classes of lipids were involved in all experiments. One lipid belongs to the glycerolipids family while the others are Phospholipids. These lipids are amphiphilic, i.e. they are composed of hydrophobic tail and hydrophilic head, and this amphiphilic nature is responsible for forming the lipid membrane.

2.2.1. Lipids

a. Monoolein:

Figure 24, 1-(cis-9-Octadecenoyl)-rac-glycerol, $\geq 99\%$ of purity, (Sigma Aldrich, Germany) molecule composed of a hydrophilic head and a hydrophobic tail. it's a simple *glycerolipid*; the hydrophilic head consists of the glycerol moiety with two hydroxyl groups responsible for the hydrophilicity of the head group [121]. The hydrophobic tail is a single hydrocarbon chain which is attached to the head group through an ester bond. The two hydroxyl groups of the head are expected to form the hydrogen bond with water in the aqueous phase while the tail is very hydrophobic, leading to the amphiphilicity of the monoolein. In more precise classification, the Hydrophilic-Lipophilic Balance

(HLB) value is 3.8. For our experiments, monoolein is used (5 to 15/mg/ml) when we need to study an interaction between a protein and very stable lipid membrane aiming for characterizing the behaviour of this protein to the membrane. Monoolein is very soluble in oil and chloroform but insoluble in water and alcohol [122].

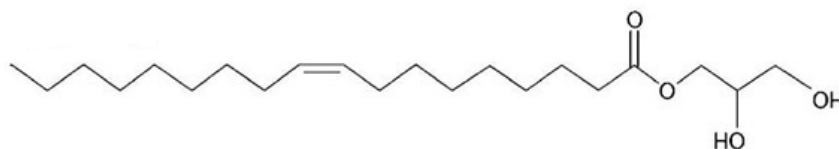


Figure 24: Chemical structure of Monoolein (Conn, 2012)

b. DOPC

Figure 25, DOPC, 1,2-dioleoyl-sn-glycero-3-phosphocholine, $\geq 99\%$ of purity, (Avanti Polar, USA) is a member of Phospholipids that incorporates a choline head group and specifically is a synthetic Phosphatidylcholines. DOPC is known as a major component of biological membranes. As a part of the outer leaflet of cell membranes, DOPC is responsible to insulate the internal chemistry of a cell as a permeable barrier. In a biological cell, DOPC is being synthesized in cGMP (Cyclic guanosine monophosphate). DOPC forms liposomes (Uni-laminar Vesicles, UVs) in aqueous media alone or in combination with other lipids e.g. DOPS (Phosphatidylserine) [123]. Due to the unsaturated hydrocarbon chains, it is more susceptible to photo-oxidation and degradation. DOPC is the main lipid we use to fabricate a lipid membrane with concentration of 5 mg/ml; at least 70% of the bilayer lipid membrane composition is DOPC. It is soluble in most of organic solvents, oil and has limited solubility in water [124].

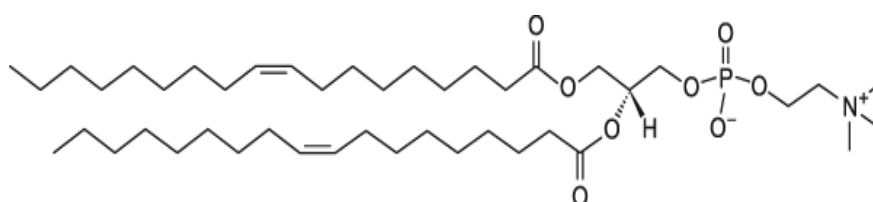


Figure 25: Chemical structure of DOPC (Avanti Polar Lipids, n.d.)

c. DOPS

Figure 26, DOPS, 1,2-dioleoyl-*sn*-glycero-3-phospho-L-serine, $\geq 99\%$ of purity (Avanti Polar, USA) is an unsaturated, negatively charged phospholipid found abundantly in eukaryotic cells. On the contrary to PC, PS is found mainly in the inner leaflet of the plasma membrane. DOPS is an excellent substitution for PS present in brain as it has similar physical properties and is more stable to oxidation [123] due to the negatively charged in the head group. For our experiments, DOPS plays a significant role in directing protein binding and contributes to electrostatic association of poly cationic legends with the membrane when used in molar concentration of 1mM of total lipids [125]. It is being added with a percentage of less than 5% just to play achieve the goal we have just mentioned.

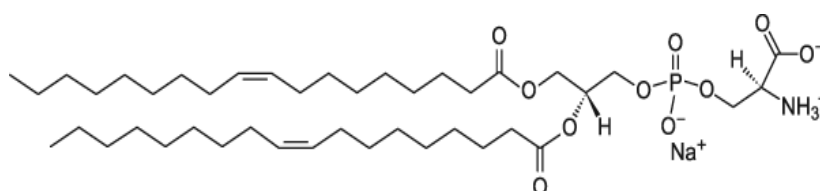


Figure 26: Chemical structure of DOPS (Avanti Polar Lipids, n.d.)

d. NBD PE

Figure 27, (NBD PE) 1,2-dipalmitoyl-*sn*-glycero-3-phosphoethanolamine-N-(7-nitro-2-1,3-benzoxadiazol-4-yl) (ammonium salt) NBD PE; Phosphatidylethanolamines (PE), $\geq 99\%$ of purity, (Avanti Polar, USA), are a class of phospholipids found in biological membranes mainly in the inner leaflet of the cytoplasmic membrane. DOPE is used to generate fluorescent multilamellar vesicles. We have used the fluorescent form of DOPE which is NBD. We used only 1 or 2 μL form 1 mg/ml patch.

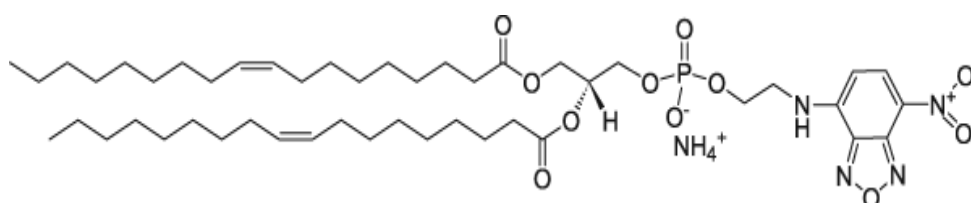


Figure 27: Chemical structure of NBD-PE (Avanti Polar Lipids, n.d.)

e. Cholesterol

Figure 28, Cholest-5-en-3 β -ol, $\geq 99\%$ of purity, (Avanti Polar, Germany) is a lipid molecule that belongs to sterols, found in mammalian cells and is responsible for the membrane structural integrity and fluidity [126]. We are using cholesterol in our experiments because around only 2 mol % of cholesterol are responsible for increasing lipid packing, thickness and rigidity [127, 128].

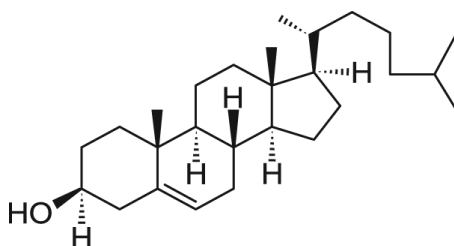


Figure 28: Chemical structure of Cholesterol (Avanti Polar Lipids, n.d.)

2.2.2. Proteins

a. Gramicidin A

Gramicidin A (gA), $\geq 99\%$ of purity, (CAS No.11029-61-1) (Sigma Aldrich, Germany) is a member of Gramicidin D antibiotic. Gramicidin D antibiotic is consisting of three compounds; A, B and C making up 80%, 6%, and 14%, respectively [129, 130]. All of them are obtained from the bacterial species *Bacillus brevis* and called collectively gramicidin D [130]. It is antibiotic active against Gram positive bacteria by forming membrane channels that are specific for monovalent cations [131]. Gramicidin A were purified from natural gramicidin by Sigma. Each gramicidin A channel is consisting of 2 subunits or molecules (fig. 29) [132]. Conductance measurements on gramicidin A ion channel across lipid bilayer membranes which have a uniform height [133]. Also, conductance measurements are depending on the concentration of electrolytes. One more lipid specificity, which has a major effect on conductance measurements, is the thickness of the lipid membrane. It was found that negatively charged lipid as in case of *phosphatidyl serine*, the rate of conductance is decreased. This phenomena was explained as that the repulsion between the negative charges are

causing increase in the thickness and consequently the conductance of the gramicidin channel [133] In our experiments, Gramicidin A is used as ion pore channel due to its *ionophoric* activity.

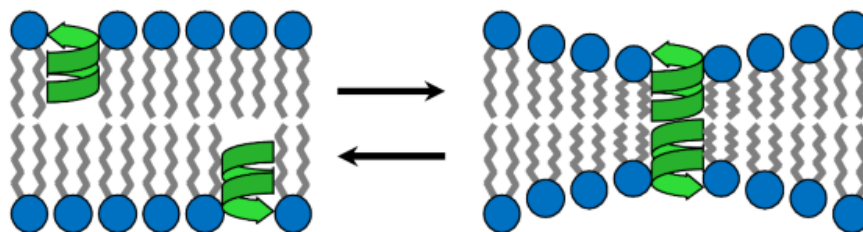


Figure 29: Gramicidin A (in green) insertion into lipid bilayer membrane. In the left part, the two subunits of the gramicidin A are diffusing in the lipid membrane until they find each other to form an ion channel; like in the right diagram. In the right diagram, illustration of one functional ion channel. Copyright © 2015 Justin M. David et al. CC BY 4.0 (Rajasekaran, 2015)

2.2.3. Coenzyme Q10 (CoQ10)

Figure 30, Coenzyme Q10, , $\geq 98\%$ of purity, (CAS No.303-98-0) (Sigma Aldrich, Germany), also known as Ubiquinone, is a chemical cofactor found in cells of majority of organisms [134]. It is a non-protein lipid-soluble compound. The chemical name is 2, 3-dimethoxy-5-methyl-6-multiprenyl-1,4benzoquinone. The nomenclature is derived from the chemical structure; Q refers to the chemical group *quinone* and 10 refers to 10 *isoprenyl* subunits [135, 136].

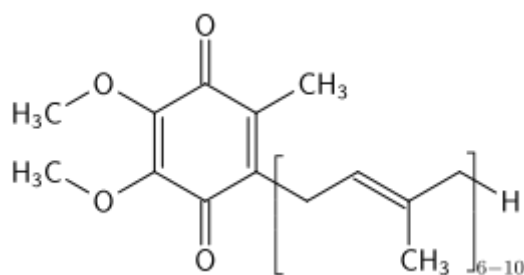


Figure 30: Chemical structure of Coenzyme Q10 (Krishnavedala, 2014)

The main role of CoQ10 is being a transmembrane electron transporter; electron carrier [135], in the electron transport chain of the mitochondria and therefore it is playing a crucial role in production of ATP [134, 136]. CoQ10 was found also to play a role in membrane stabilisation [134]. Despite acting as a vitamin but CoQ10 is not

considered as a vitamin because it is synthesised inside the cell [136]. In addition to the previous crucial roles, in the reduced form; *Ubiquinol 10*, was found to play a role in removing free radicals from lipid membranes and consequently prevents any radical damages to the membrane; functions as anti-oxidant [135]. The deficiency in CoQ10 due to genetic disorder or excessive consumption was found to be associated with increased radical oxidative stress and decreased ATP production [17]. Drugs like statins, anti-hyperlipidaemias, was found also to decrease the circulating CoQ10 [137]. An administration of ubiquinone 10 as a preoperational procedure, was found to increase heart-tolerance to ischemia [138, 139]. In addition to previous bio-importance, increased plasma CoQ10 was found to be important in prevention of bad cholesterol, LDL oxidation, prevent muscle retrogression with age and decrease the risk of heart diseases [139, 140, 141]. Dependently on age and health conditions, the bioavailability of CoQ10 supplements is changed [140].

2.2.4. Oils

a. *Squalene*

Squalene, $\geq 98\%$ of purity (fig. 31) (Merck, Germany) is a natural organic oil we are using as the non-aqueous phase in which we dissolve lipids. It is an intermediate compound in the cycle of cholesterol biosynthesis [142]. Naturally, squalene is obtained from two sources; the main source is the oil of sharks liver while the second source is plant based; mainly vegetable oils [142, 143]. Another source of squalene is biosynthetic technique in which genetically modified-yeast are involved in production of sufficient commercial amounts [144]. The chemical structure of squalene is shown in figure 5, it is consisting of 30 carbons. The chemical formula is simply written as $C_{30}H_{50}$. It is not susceptible for oxidation by lipids and is used in cosmetics production as it's biocompatible [142]. About 60% of dietary squalene is absorbed and transferred and localized mainly in skin; mainly in skin lipids serving as anti-oxidant by quenching singlet oxygen [142, 145].

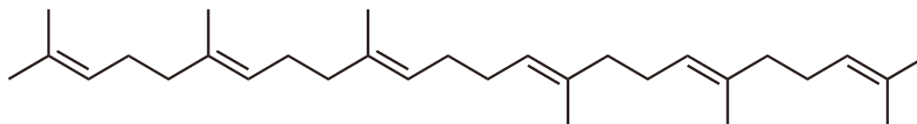


Figure 31: Chemical structure of squalene (Ronco, 2013)

b. Silicone Oil

Silicon oils (Fig. 32), such as Silicon oil AR 20 (CAS No. 63148-62-9) (Merck, Germany) are any siloxane liquids with organic side chains. The polymer chain consists of silicon and oxygen molecules alternating with each other. It is used in our experiments to decrease membrane tension and so increase the stability and lifetime of bilayer membranes. Phospholipids are not dissolved in such oils [58].

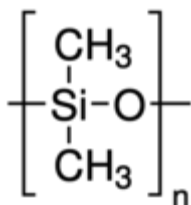


Figure 32: General Chemical structure of any Silicon oil. (20Si)

2.2.5. Polydimethylsiloxane (PDMS)

PDMS or *Dimethicone* is a silicon-based organic polymer its chemical structure is characterized by a siloxane backbone of silicone bonded to oxygen atoms. PDMS is chemically inert, non-toxic and non-flammable in general. Concerning the properties that make PDMS our first choice, PDMS is optically clear and has hydrophobic behaviour. Optical clarity is very essential for observation of fluids in the chip and hydrophobicity is helping in generate unsupported lipid membranes. Also, PDMS is relatively cheap and easy in microfluidic chips fabrication. The PDMS elastomer Sylgard™ 184 (Dow Corning GmbH, Germany) is the one used in all our experiments. The pack is composed of two bottles, one of them is the polymer (silicon rubber base) where the other is the cross linker (catalytic agent; mixture of platinum complex and copolymers of methylhydrosiloxane)[146]. We Mix the two previously mentioned components (base and linker) in a container in a ratio of 10:1, respectively. For about 5 minutes, mix the previous mixture properly for insuring uniform mixing.

2.3. Methods

2.3.1. Formation of Small Unilamellar Vesicles (SUV)

The protocol used in this purpose is for Morrissey Lab (dept. of Biochemistry, university of Illinois, Urbana, USA) for preparation of SUV from phospholipids using sonication. Stock lipid solutions chloroform for DOPC (25 mg/ml) DOPS (10 mg/ml) and DOPE (10 mg/ml) are prepared. In case we need PC: PS SUV, we mix 63 μ l of DOPC with 42 μ l DOPS giving a molar ratio of 80:20 respectively. Also, in case of PC: PS: PE, we mix 79, 42 and 80 μ l respectively. Then we dry under nitrogen and then put in a vacuum chamber for at least one hour. Later on, we add 2.6 ml of buffer to the dried film, let them rest for one hour after that we shake vigorously until we have a white solution. The last step is to put in the sonicator for about 10 to 30 min. After that we keep this stock in 4° C fridge. In case we need fluorescent SUV, we add 5 μ l PE-NBD to the lipid mix and then follow the same technique.

2.3.2. Microfluidic chips fabrication

The fabrication of microfluidic chip is divided into two steps; the first step is to produce a master by photolithography and followed by the second step, to replicate the chip from the master by soft lithography.

a. Photolithography Technique

The most important technique to fabricate microscale structures; microfluidic devices, is lithography. Two-dimensional structures are the result of patterning process of the photolithography which is used to fabricate our chips [147] as shown in figure 33. To fabricate a microfluidic chip, we must first design the desired channels using a drawing software. In our case, we are using AutoCAD® 2016. After designing the pattern, the next step is to print this pattern to a film photomask (Printing step, JD Photo Tool, UK). The photomask is an opaque polyester film with transparent structures, our channels. These transparent channels allow the UV light of lithography to be transferred to the photoresist.

We prepare the silicon wafer on which the structure will be transferred during the photolithography by cleaning and coating. To clean the silicon wafer, we first rinse the silicon wafer with isopropanol and acetone to remove any undesirable particles on the surface. According to the size of the silicon wafer, we add the desirable amount of SU-8 100/50 (Microchem, USA) also about the preferred height, which is about, 1ml / inch. No air bubbles should be seen on the wafer surface before spin coating. The next step is Spin coating; we place the wafer on the spin coater for uniform coating of the whole chip. This is a crucial step to obtain the desired height (channel thickness). According to the manufacturer we adjust the speed and time of spinning. (Table 1)

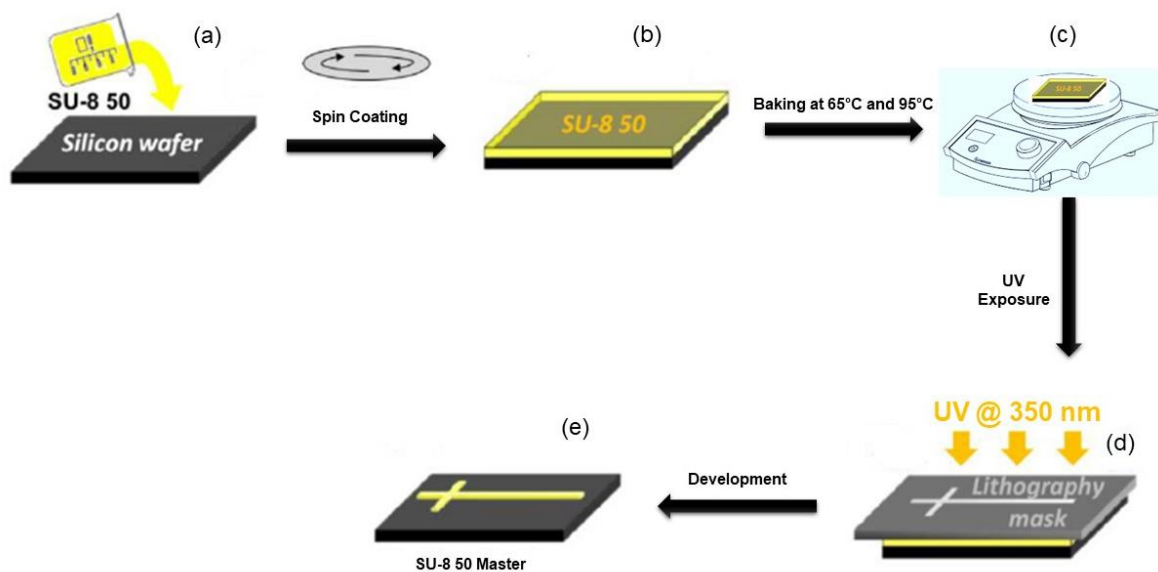


Figure 33: photolithography procedures (a) addition of SU-8 50 to pre-cleaned silicon wafer (b) after spin coating, the SU-8 is uniformly distributed (c) soft baking to evaporate the solvent of the photoresist (d) the mask is on top of the silicon wafer then starting UV exposure (e) the final SU-8 master after development. Self-drawing

After uniform coating of the wafer, we transfer it to the hot plate for soft baking (pre-exposure backing) at 65°C and 95°C. This allows the photoresist to dry which improves the adhesion to the wafer. Directly and immediately, we transfer the wafer to the UV exposure machine and place it in the specified place. Then, on top of the wafer, we add the photomask and start the UV exposure for certain time according to the desired height (table 1).

Table 1: Microfabrication parameters

	Unit	SU8-50		SU8-100	
Channel height	μm	30	50	80	120
Spin Velocity	Rpm	2000	1500	2000	1700
Pre-bake (65 °C)	Min	4	5	10	13
Pre-bake (95 °C)	Min	13	15	30	37
Exposure (15 mW/cm ²)	Sec	30	30	30	30
Post bake (65 °C)	Min	1	1	1	1
Post bake (95 °C)	Min	2	2	5	7
Development	Min	2	5	5	8

After exposure, the wafer is then subjected for post exposure baking, also at 65 and 95° (table 1). After the post exposure backing, the exposed structure (on the chip) is developed. We place the wafer in a beaker contains SU-8 developer (1-Methoxy-2-propyl acetate) on a shaking plate. After around 5 minutes, we could see the desired structure of the chip on top of the wafer (table 1).

b. Soft lithography (PDMS Moulding)

In this step, (fig. 34) we use the previously prepared SU-8 master to fabricate the final chip by moulding the PDMS on top of the mask, then peeling out the PDMS after baking. In the following sentences, step by step description of the soft lithography procedures:

Before pouring the PDMS mixture on top of the master, we place the PDMS mixture in a desiccator to remove air bubbles being formed during the mixing step. After complete removal of air bubbles, we pour PDMS (fig. 34b) on top of the exceptionally cleaned SU-8 master, then we put it back again in the desiccator for any further bubble's removal.

We placed the petri dish on a hot plate at 70 °C for about 2 hours (fig. 34c). The aim of this step is the cross-linking between the polymer and the linker resulting in solidification of the mixture. The cross linked PDMS is peeled off from the SU-8 master

and holes (inlets and outlets) are being done using set of pinchers with different diameters (fig. 34d).

We bind the PDMS chip to a glass slide (fig. 34e). To achieve that, we clean the PDMS chip and the glass slide carefully with alcohol (Isopropanol). Then we apply plasma cleaning, using Plasma cleaner (Diener electronic GmbH, Germany).

Upon this process, both surfaces are cleaned from any impurities and contaminants. The two surfaces are being bounded to each other to achieve irreversible binding; this bind irreversibly to each other. Finally, we put the chip over night at 135 °C to compensate the acquired hydrophilicity from plasma treatment (fig. 34f).

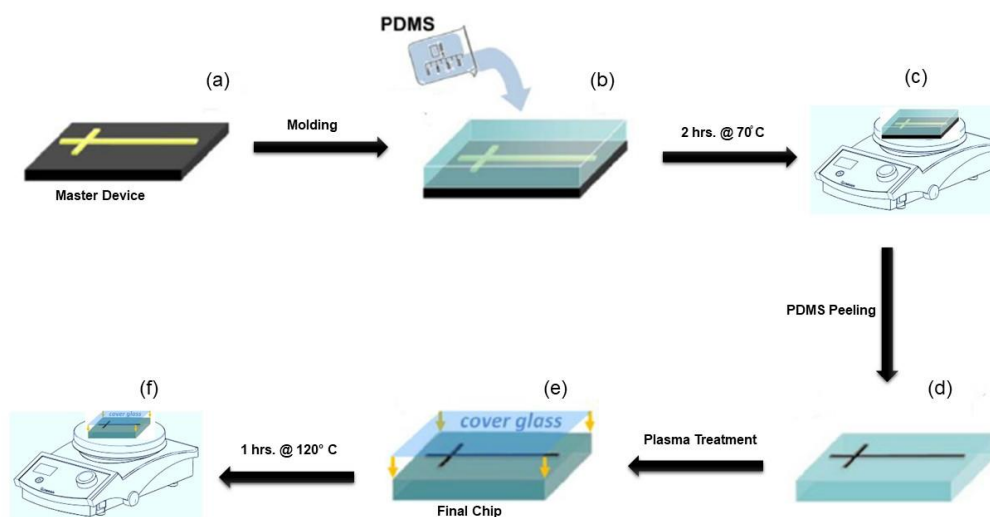


Figure 34: Soft lithography procedures (a) Cleaned SU-8 50 master prepared by photolithography (b) addition of PDMS mixture to the master (c) baking of the PDMS mixture (d) the PDMS is peeled from the master (e) plasma treatment for PDMS and glass followed by attaching both part to each other (f) heating the chip to insure irreversible bonding. Self-drawing

2.3.3. Microelectrode Fabrication

In our experiments, we need two electrodes; a *reference electrode* in contact with the buffer solution and a *test electrode* which is attached to the head stage of the patch clamp amplifier. By these two electrodes, we were able to apply voltage and measure the electric capacitance of the lipid bilayer membrane. Not only electrical capacitance but also, we were able to measure the electrical properties of the membrane if there are some proteins inserted in to the membrane.

In this research, we have used two types of electrodes; carbon electrodes provided by Heka[®] and silver chloride electrodes fabricated by us in our chemistry lab. In the next few pages, a step-by-step description for the fabrication process of the silver chloride electrodes:

A silver wire with diameter 0.25 mm (Goodfellow[®], Germany) with purity 99.99% were immersed in ethanol 99.8% for 15 min for complete removal of any undesirable particles. Then we rinse with Millipore water and dry it by nitrogen gun under hood to avoid dust particles as much as we can [148]

To chlorinate the silver wire, we prepare a 150 mM NaCl solution (sometimes we use 100 mM KCl). Using a power supply (Voltcraft VLP 1303 pro, Germany) we immerse the Ag wire in the NaCl solution and contact it to the positive terminal of the power supply and a second silver wire to the negative terminal. A voltage of 2.5 V is applied for about 25 minutes (Current $A \approx 1.5 \text{ mA/cm}^2$). The successfully chlorided part is turning into darker or blackish colour results from deposition of Ag on the wire. After that we remove it from the NaCl solution and place under the hood in a closed petri dish, then repeat the same procedure for the second wire for the other electrode.

We choose an appropriate glass pipette where we will insert the silver wire. Due to movement of charges upon voltage application, thermal noise is generated (dielectric noise). To overcome this noise, we used *Borosilicate* glass pipettes (SUTTER INSTRUMENT[®], USA) with dimensions of 1.5 mm outer diameter and 0.86 inner diameter and another dimension of 1.00 mm and 0.50 mm outer and inner diameter, respectively with 10 cm length for both [148].

After the selection of the proper pipette, we used a PN-31 Pipette Puller (NARISHIGE[®], Japan) to provide a sharp tip for both electrodes that can be inserted into the microfluidic channel. The device is motorized and allow many different pulling options according to the required diameter for the tip of the electrode. The pipette polar device is fixing the glass pipette from both sides and in the middle, there is a heat source. The holder is pulled by a magnetic force while the heater is on. Once the pipette is melted from the middle, one half of the pipette being pulled away from the other part. Hereby we have formed a glass pipette for one electrode: parameters shown in table 2.

Table 2: Micropipette Pulling Parameters (Tritech Research, 2020)

Parameters	Value
Heat	792 (100 = Heater Voltage 1V)
Magnet Sub (weaker pulling force)	17 ± 3 (100 = Magnetic Voltage 1V)
Magnet Main (stronger pulling force)	70 ± 3 (100 = Magnetic Voltage 1V)
Time	10 – 15 sec.

Inside the glass pipette there is the “pipette solution” which is agarose solution or agarose salt bridge (i.e. it is key element in patch clamp measurements). This solution is prepared by dissolving 0.5% agarose (= 0.5 g) in 25 ml of the same buffer that is used in the experiment, *e.g.*, in our case, we used KCL and NaCl, so when we used NaCl as aqueous media, we prepared the agarose with 25 ml of 150 mM NaCl. For dissolving the agarose completely, place the beaker on the hot plate (= 135 °C) and stirred for about 30 minutes with magnetic stirring until having a clear solution.

After preparation of the agarose solution, we fill the two glass pipettes half. This is simultaneously happened when you insert the pipette in the beaker. For precise measurements it is important to make sure that there is no air bubbles. Then the Ag/AgCl electrodes are gently inserted in the pipettes to avoid any deviation in the electrodes.

The two glass pipettes were sealed with epoxy glue to avoid leakage of the agarose or the buffer during the experiment. After that, the *test electrode* is fixed to the head stage *i.e.* the micropipette holder provided by HEKA (fig. 35).

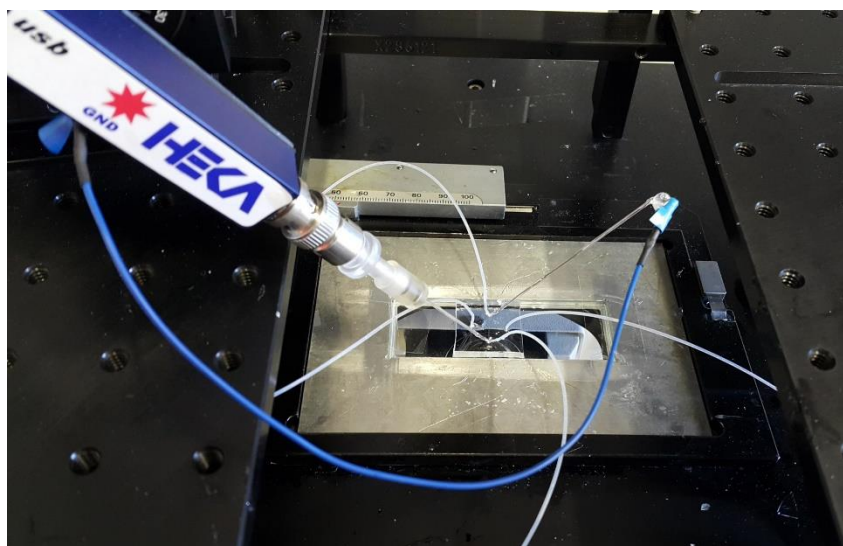


Figure 35: our setup for electrical measurements. Electrodes sealed to the PDMS chip and connected to the amplifier through the head stage of the HEKA setup.

Chapter 3: Different Microfluidic Designs for Bilayer Membrane Formation and Membranes Interactions

In this chapter, we present different microfluidic schemes have been used for production of one and/or two lipid bilayer membranes (BLM). For each scheme, we are presenting pros and for the formation and exploration of bilayer.

3.1. One Lipid Bilayer Membrane

These frequently used schemes are dedicated to study stability of certain lipids or to insert some ion channel-forming proteins to study their functions. Such single membrane can be fabricated into different designs, we discuss in this chapter the most reproducible and applicable techniques. The description is based on the geometry of the microfluidic chip.

3.1.1. Cross-Geometry

As shown in (fig. 36a), this design is consisting of two perpendicular and intersecting channels with three inlets and only one outlet. This design with firstly introduced by Funakoshi in 2006 for protein analysis [149]. It provides an easy platform for quick and reproducible lipid membrane formation. The lipid membrane is fabricated in the middle gap by letting the two water fingers face each other. Injection of water figures is done using a syringe pump. Before starting the experiment, we perfuse some oil-lipid mixture to the chip for about one hour to insure the hydrophobicity of the chip. Once we have introduced the two water fingers slowly (fig. 36b), both are decorated with the lipid molecules. Due to the amphiphilic nature of the lipid molecule, the hydrophilic head is inserted into the water finger where the hydrophobic tail is immersed in the oil phase. After few minutes, each water finger is covered with a monolayer of the lipid. Once these fingers touch each other (fig. 36c), they start the formation of the lipid membrane (fig. 36d). As mentioned before, the contacting process must be done very carefully regarding the velocity of the water finger. Such velocity is controlled through two issues: the injected volume and geometry of the channel/finger. The outlet

is controlled by a valve to prevent the outflow of the water fingers. With such geometry, we can produce large lipid membrane with diameters up to 500 μm .

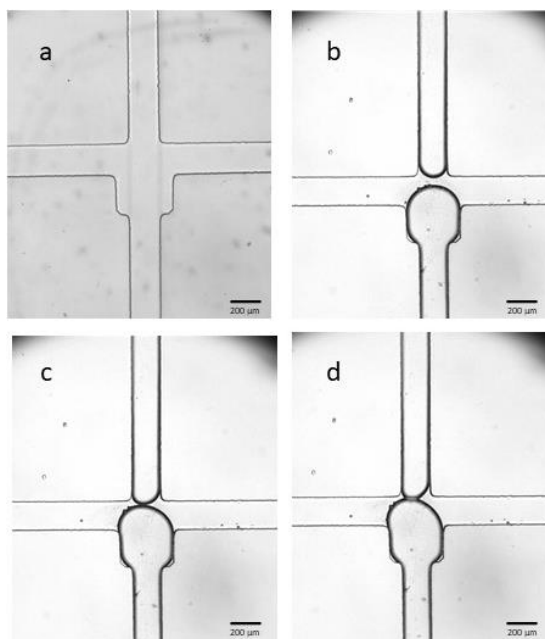


Figure 36: Cross-Geometry microfluidic chip; a) an image for empty chip, b) insertion of water from 2 facing-inlets, c) the two water finger touch each other to form a bilayer, d) a lipid bilayer membrane formed in the middle between the fingers

The formation of a lipid bilayer membrane is proofed using electrophysiological technique. As mentioned in the previous chapter, the aqueous fingers are the electrodes with Ohmic resistance, and the bilayer is considered as a capacitor in an electrical circuit. We use such property to ensure the formation of the bilayer. Figure 37 is showing the capacitance signal obtained during membrane formation and deformation. As shown in (fig. 37a), once the two bilayers touch each other and before the zipping, we have recorded a small capacitance. Once zipping started (fig. 37b), we can see a rapid increase in capacitance. In (fig. 37c), the bilayer is formed and reached almost a plateau capacitance, indication of stable membrane area. Figure 37d, the two monolayers started to set apart from each other gradually represented in the rapid fall in capacitance value.

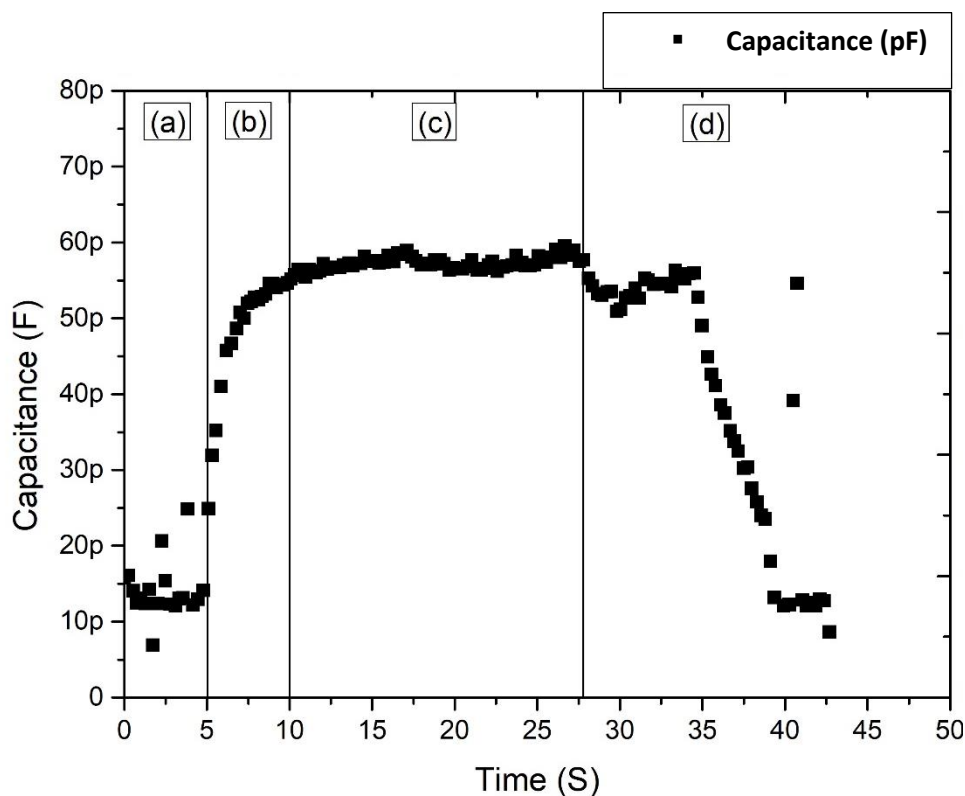


Figure 37: Capacitance measurement graph for bilayer membrane formation. Section (a) is showing the first stage in BLM formation in which the 2 monolayers touch each other but no BLM formed yet. Section (b) is the jump in capacitance once the zipping starts. Section (c) is almost a fixed membrane is formed and yielding a stable capacitance. Section (d) the 2 monolayers are separated again from each other and capacitance drops to reach almost zero with time.

Despite reproducibility and applicability of such design, it still has serious limitations. One serious limitation is the difficulty to keep the membrane in the middle gap; where the membrane is formed, for long time as it will tend to deviate in the horizontal channel. Moreover, in case of testing some biomolecules, like ion-channel forming proteins, we must insert them from the start of the experiment, so it fits in the monolayer then form the whole ion channel after zipping. The third limitation is resembled in no possibility to insert ion-channel blockers to reveal their effects; the change of the aqueous fingers' composition is not possible once the bilayer is formed.

3.1.2. Parallel-Channels Geometry

To overpass the previous drawbacks of the cross geometry, we are using the parallel-channels geometry (fig. 38a). This design consists of two inlets for water, one inlet for oil and two outlets. The two water channels are separated from each other except

in a gap in a range of few hundred microns (fig. 38a). Like before, prior for starting the experiments we perfuse the oil-lipid mixture into the PDMS chip to guarantee hydrophobicity. To start the bilayer formation, we perfuse the two water fingers by two separate pumps but with the same volume flow rate. Both fingers surfaces are being decorated by the amphiphilic lipid molecules until they reach the gap, and then start touching each other to start zipping process (fig. 38c).

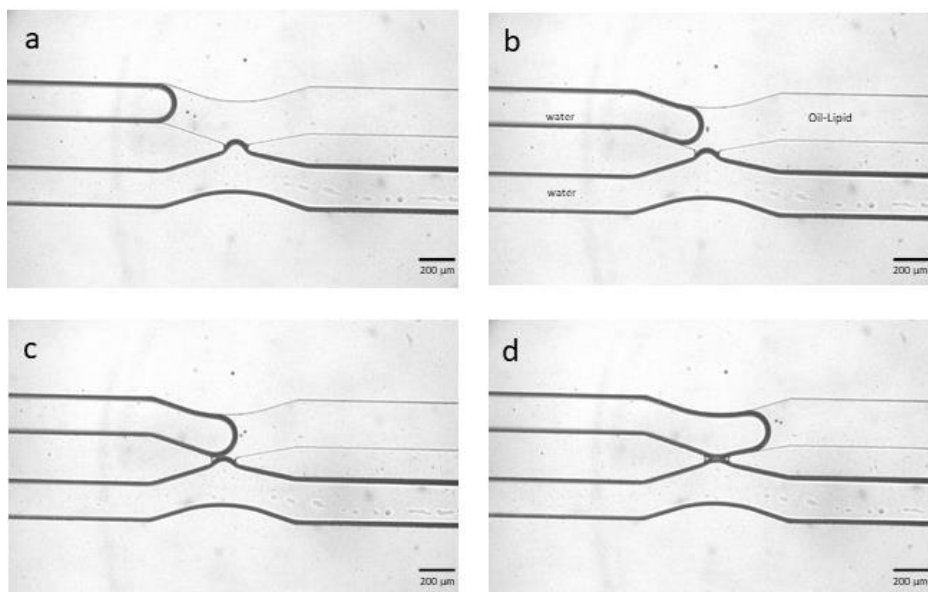


Figure 38: Two parallel-channels geometry. (a) The start of the experiment by introduction of the aqueous phase from both sides. (b) The two water fingers are getting close to each other to start the fusion. (c) The fusion has started in a small area and continue to form a BLM. (d) The BLM extend until it reaches a specific area according to the gap width.

As in the previous geometry, we have applied an electrophysiological measurement to ensure the formation of the BLM. Figure 39, these sections represent steps of formation of a BLM starting by forming a stalk, then increasing the area of the BLM until it reaches a plateau area. Before zipping, we can see some electrical noise which disappeared after the zipping and membrane formation. With time, it is noticeable that the area of the BLM is getting larger; represented in the slight upward direction of the capacitance curve.

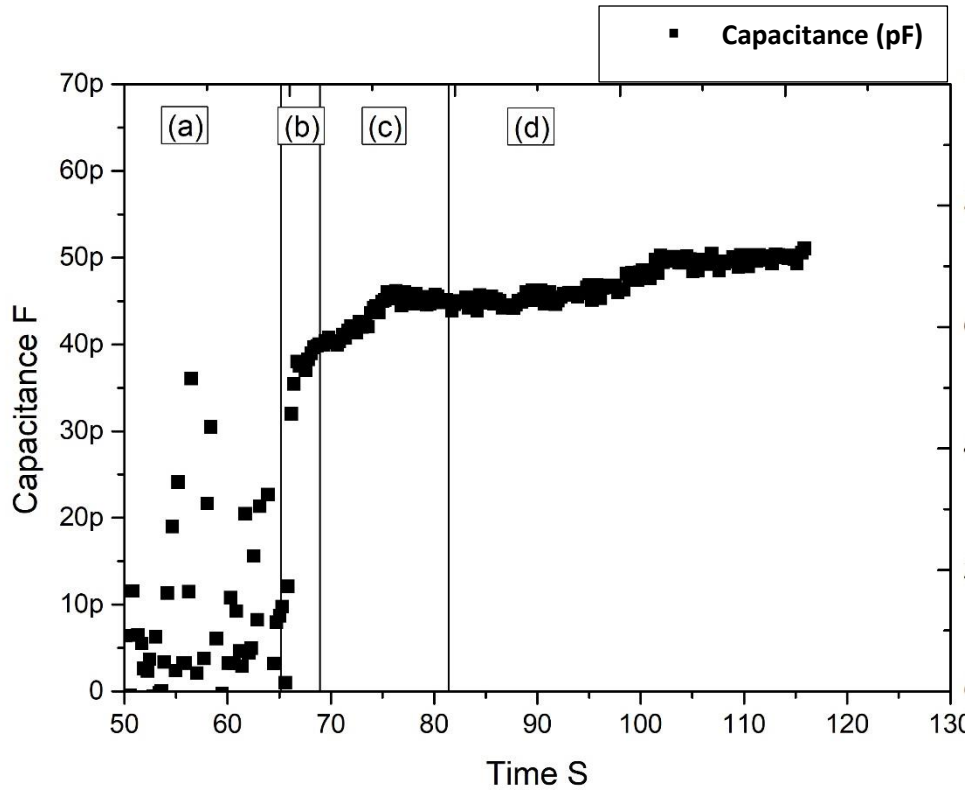


Figure 39: Electrophysiological measurements for BLM formation in the parallel-channels geometry. Section (a) is showing the first stage in BLM formation in which the 2 monolayers touch each other but no BLM formed yet. Section (b) is the jump in capacitance once the zipping starts. Section (c) is showing slight increase in BLM area. Section (d) is showing a slower increase in the formed BLM.

This design has many advantages over the previous cross geometry. First, the control of the flow is easier because the two fingers are parallel and not opposing each other; this way we escape the pressure produced by opposing buffer fingers. The second advantage is in the easiness of testing biomolecules. Once we formed the bilayer, slowly we can add any biomolecules to study their interaction with the BLM. During the application of biomolecules, the BLM remains stable and fixed in its place. The main disadvantage of this design is that the membrane would leave its place in case of any pressure differences on both sides or in one of the outlets; like in the cross geometry but with little probability, and as a result the membrane would be ruptured.

3.1.3. Tube Geometry

This is a quite simple technique in case we need to fabricate a bilayer membrane. As in (fig. 40), the design is composed of a tube; PDMS or any polymer, two electrodes plus oil-lipid mixture and the electrolyte solution. We have applied different techniques

to form a bilayer. The first one was to fill the whole tube with electrolyte solution then, with a syringe, to push some oil-lipid mixture in the middle of the electrolyte solution and this leads to formation of two opposing electrolyte fingers; as the newly generated oil-water interfaces get decorated with lipids, they merge and form a lipid bilayer when sufficient amounts of the oily phase drained into the PDMS tube. We can control the oil-lipid gap between the two fingers by pushing in/sucking out using by the syringe. The rest of the oil could be removed by drainage over time. That is why we have thought about PDMS tubes. We covered cylindrical solid tube with PDMS and after solidification we removed the solid tube from the middle (Fig. 40c). This results in better drainage of oil and more control for the experiment.

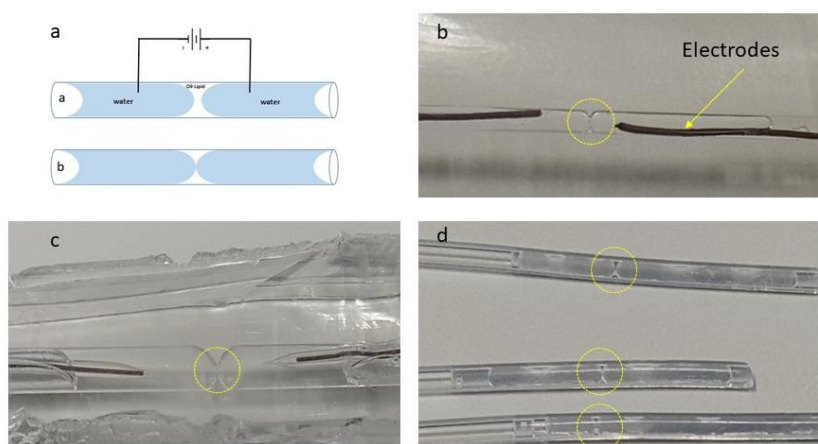


Figure 40 schematic diagram of the Tube scheme for building a BLM. (a) Schematic diagram showing the concept of the design, two opposing electrolyte solutions separated by oil-lipid mixture, with time the oil drain and the two monolayers fuse and form the BLM. (b) In a PTFE tube, we have tried first to build a BLM (inside the yellow ring) and record capacitance of the formed membrane. (c) In homemade PDMS channel, we have applied the same procedures to build a BLM. (d) We were able to build many BLMs in a parallel way with different lipid composition.

Another procedure to build a BLM in the same tubes, was to fill the oil first and then to generate two separate electrolyte solution fingers. With the same technique we were able to control the size of the gap.

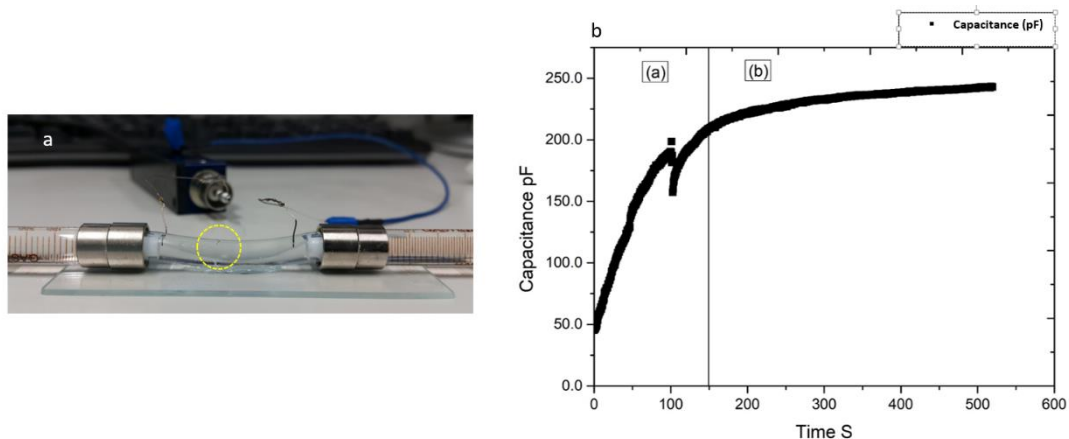


Figure 41: A real image for a more professional 'Tubing' system. (a) A tube with 4 mm diameter connected from both sides with 2 glass syringes to push the electrolyte solution from both sides and prevent its leakage, on top of the tube from both sides, there are 2 electrodes were inserted through 2 holes and connected to the HEKA amplifier, in the middle; inside the yellow circle, the BLM was formed. (b) An electrical capacitance curve was recorded to ensure the formation of a BLM; in section 'a' the gradual increase in the bilayer area is exported as increase the capacitance value until reaching a fixed membrane area as in section 'b' N.B: top and right scale have the same labels as lower and left scales respectively.

In a more advanced way, we have produced a BLM inside larger tube (with a diameter of 4 mm) (fig. 41a). There is a tiny hole on top-middle the channel, this is allowing the oil to get out once we push the oil. Consequently, from right and left, we push the buffer in a slow technique. The oil started to get out from the middle, both buffer fingers are being decorated with lipid molecules forming two opposing monolayers. Once these two monolayers touch each other, zipping started to form a BLM (fig. 41b). This bilayer formation is proofed by electrical measurement. The gradual increase in membrane area is reflecting as increase in the membrane capacitance. Such gradual increase is explained by the hard and slow drainage of oil from the tiny hole. After reaching a certain area size we could notice a slight increase in capacitance over time (fig. 41b). Such tubing design offer a rapid way to build a bilayer or many in parallel (fig. 40d) to study, for example, a formation of ion-channel for conductance measurements. Unfortunately, due to the curved interface optical access is limited and hardly possible with optical microscopy. Also, we could not give a precise

membrane area. Moreover, we cannot change the electrolyte solution composition because of the sensitivity of the membrane.

3.2. Two Lipid Bilayer Membranes

With the previous approaches it was possible to build bilayer membranes, while in the following we describe a microfluidic approach to fabricate two bilayers in one microfluidic chip.

3.2.1. Parallel Channels

This is the most direct idea to build two free-standing BLMs opposing each other simply by slight modification in a two-parallel channels chip. Instead of two buffer inlets we need three inlets and subsequently three outlets. In case we use a chip with one or two outlets, this means a shortcut connection between electrodes and this will result in a one BLM situation, even if we see two membranes. The simple design is shown in (fig. 42).

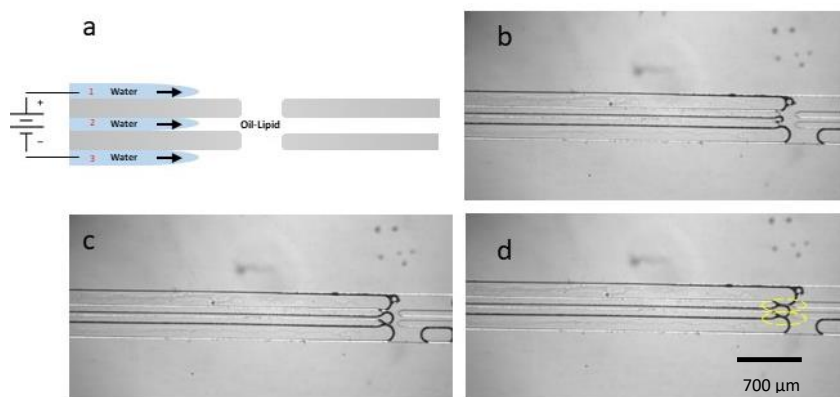


Figure 42: Schematic Diagram for microfluidic chip to generate 2 free-standing BLMs. (a) A schematic diagram describing the concept of design, three channels separated by 2 walls and 2 middle gaps where the three water fingers meet each other to form parallel membranes. The diagram is also showing the positioning of electrodes to. (b) After perfusion of the chip with the buffer. (c) The three water fingers started to touch each other to form 2 BLMs. (d) The 2 BLMs are already formed and highlighted by the yellow circles.

The above presented microfluidic scheme enabled us to study a situation which is like two adjacent cells interacting with each other. If we considered that inlet 1 (fig. 42a) is a cell, we can send some ions to inlet 3 through fusion of some SUVs; carrying these ions, with the BLM between inlet 1 and 2. The second BLM; between inlet 2 and 3, should be carrying ion-channels that somehow interact with the released ions. The gap in the middle, is considered like a synapse between the cells where the ions travel from the first to the second BLM.

For electrophysiological measurements, we positioned two electrodes in channels 1 and 3 (fig. 42a). The two membranes are equivalent to two capacitors connected in series. In a basic situation, no ion-channels, the capacitance C_{total} recorded is founded to be half of a capacitance recorded for a single BLM according to the equation (fig. 19c). The area of each BLM is important in calculating the separate capacitance; $C_1, C_2 \dots etc$. In the ideal case, we assume that both BLMs have the same area and consequently we assume that each membrane is carrying a double value of C_{total} .

In (fig. 43a), we created two BLMs and then started the capacitance recording. We recorded an average of 30-35 pF. Once one of the two BLMs was ruptured (fig. 43b), we have noticed a jump in capacitance due to formation of single-membrane situation. If the two BLMs had identical area, we would expect a jump to exactly double of the first value; where we had two BLMs, ($\approx 60-70$ pF) but because the broken BLM was smaller than the remained, we recorded a slight higher value (≈ 75 pF).

Another case to be considered is when we have added an ion channel to one of the two BLMs. In this case we have no longer two capacitor plates (Section 1.3.3.) but instead we have a capacitor and resistor connected in series.

This geometry was the first attempt to generate two BLMs in a microfluidic chip. One of the most important advantages of this geometry is the ability to keep the flow after generating the bilayer. Unfortunately, due to the number of inlets and outlets to be controlled, this design lacks the stability to build a new system with two BLMs for long time, for buffer changing or for introduction of certain molecules.

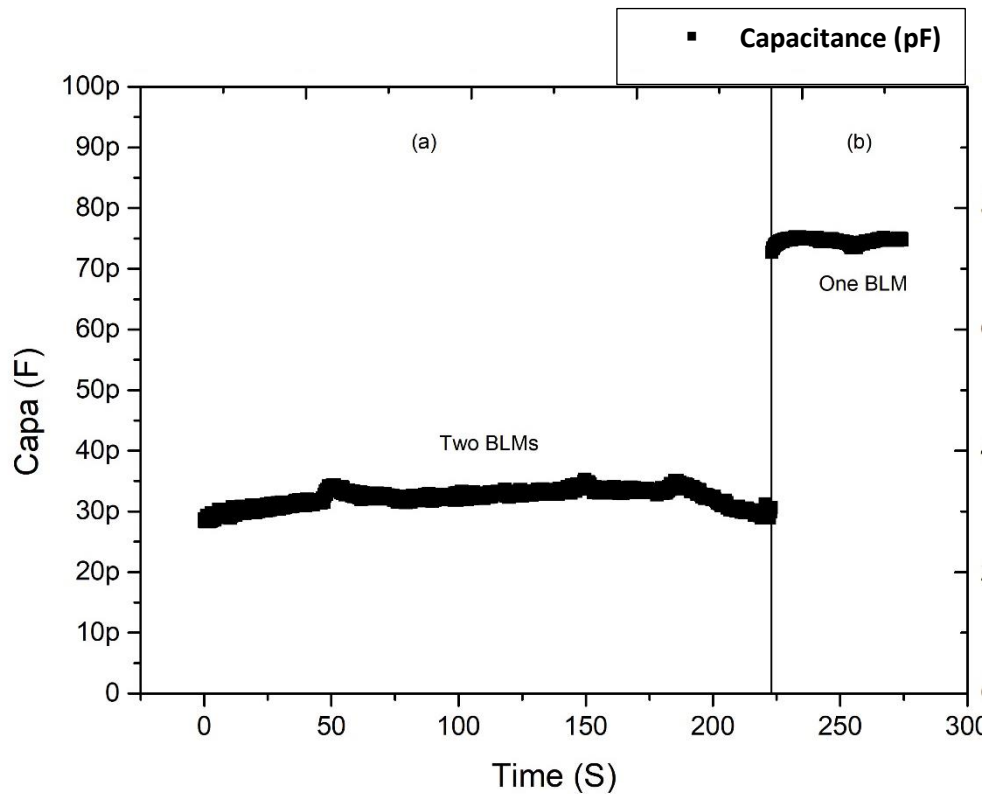


Figure 43: Capacitance measurement for 2 BLMs connected in series. (a) The 2 BLMs are connected in a series connection and giving a capacitance in the range of 30-35 pF. (b) One BLM has ruptured and creating a situation of single BLM represented by the jump in capacitance. N.B: top and right scale have the same labels as lower and left scales, respectively.

3.2.2. Parallel Channel Geometry with Different Electrodes Orientation

This parallel channel geometry is close to the previous one but with different electrodes accesses (fig. 44). The idea behind this modification is to get the electrodes closer to the free-standing membranes. Before we start the experiment, we insert the two AgCl electrodes (100 μm in diameter) from both sides (fig. 44 a-c). The experiment starts by filling the channel the oil-lipid mixture for about one hour to ensure hydrophobicity. After that, we perfuse the three buffer fingers slowly through inlets 1, 2 and 3 (fig. 44c). During the slowly perfusion, the amphiphilic lipid molecules are decorating the buffer fingers. Once the three buffer fingers reach the middle gap, the BLM start the formation process (fig. 44d). The electrical measurement is started before the formation of the two BLMs to record the zipping and formation of the membranes. The technique is also providing the advantage of flushing the buffer solution after

formation of the BLMs or inserting some ion channels. It still lacks the stability over long time and need a careful handling for buffers. The three outlets must be identical otherwise the pressure will not be the same on the three channels and this would lead to more membrane instability. The second difficult part is in the insertion of the electrodes; it must be done under the microscope to avoid occlusion of channels if electrodes were over-inserted. In this experiment, we used a non-identical channel width; the outer two channels are wider than the middle one, this has led to difficulty in pressure control and consequently the lifetime of the membrane.

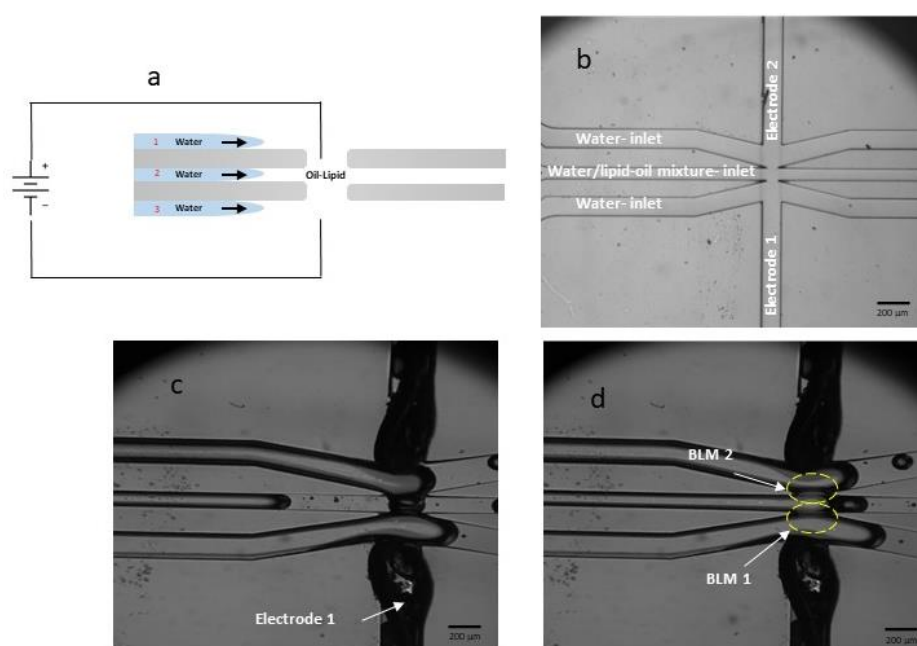


Figure 44: Schematic Diagram for microfluidic chip to generate 2 free-standing BLMs. (a) Schematic diagram for the design of the chip showing the inlets for buffer solution and oil-lipid mixture with orientation for electrodes inlets. (b) Microscopic image for empty chip with illustration for inlets. (c) After filling the chip with oil, the perfusion of the chip with buffers from the three channels started. The 2 black electrodes (100 μm diameter) are inserted from both sides. (d) The middle buffer finger is reaching the middle gap area and form 2 free-standing BLMs inside the yellow circles.

Electrical capacitance measurements for this design had been recorded (Figure 45). The graph is divided into three phases: ‘a’ before zipping, ‘b’ two BLMs phase and ‘c’ one BLM phase. In phase ‘a’ the monolayers are not zipped to form BLMs yet. Once the zipping started, we have noticed a jump (Phase b Figure 45) in the capacitance curve to about 100 pF due to formation of the BLMs; which are capacitor plates. After some

time, one of the two BLMs was ruptured and we moved back to one BLM state (fig. 45c). The jump in capacitance has reached 140 pF and not to double because the two membranes had not the same area and so the capacity of each was different from the other.

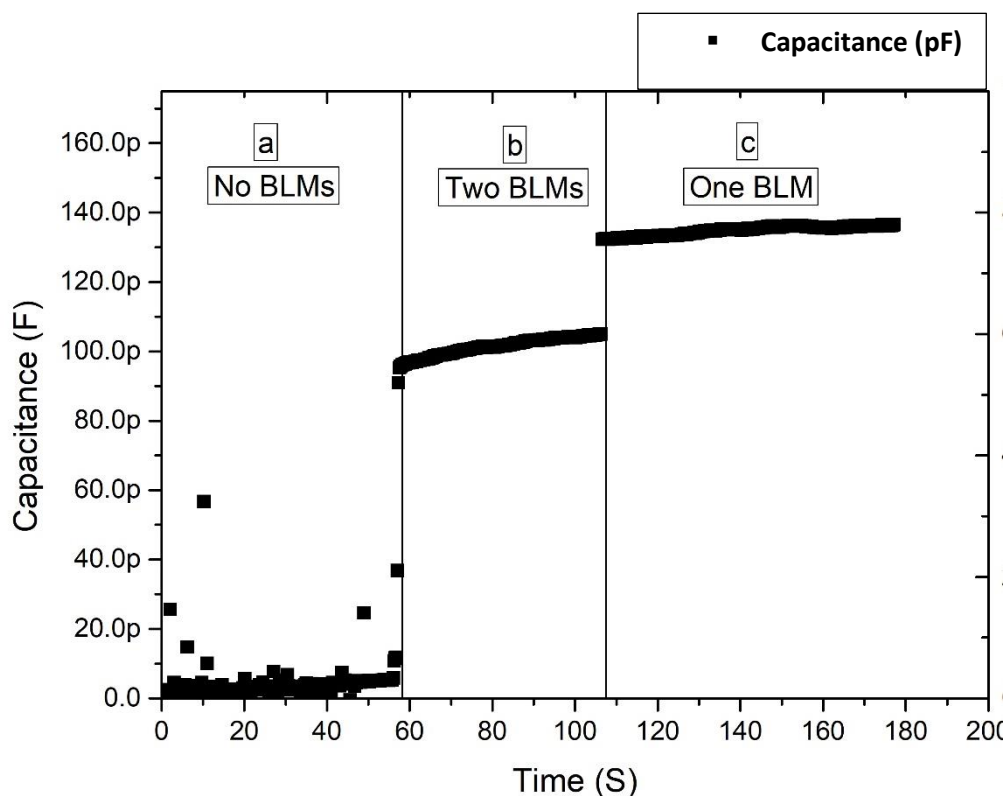


Figure 45: Capacitance measurement for 2 BLMs connected electrically in series. (a) In the first phase no BLMs are being formed yet and no capacitance was recorded. (b) The 2 BLMs are connected in a series connection and giving a capacitance in the range of 30-35 pF. (c) One BLM has ruptured and creating a situation of single BLM represented by the jump in capacitance. N.B: top and right scale have the same labels as lower and left scales, respectively.

3.2.3. Cross Geometry

These geometries have showed better stability for the unsupported BLMs over the parallel channels' chips. The main advantage of this geometry is decreasing the number of outlets to one or two outlets according to the purpose of the experiment.

a. Cross-Geometry one-outlet Design

Figure 46 is showing the most preferred structure in case we needed two unsupported BLMs with a gap in between each other. This design has only one outlet,

which make it easy to control. Three water inlets are needed in this structure in addition to one oil-lipid mixture inlet which is in the middle channel. The size of the middle channels and gaps are controllable according to the purpose of the experiment. Like before, we perfuse the chip with oil-lipid mixture for about one hour before starting the experiment to ensure hydrophobicity. After that, we start pushing the three buffer fingers slowly and gently to let the lipid molecules decorate the interfaces. Once they reach the middle gaps, they touch, zip, and form the two unsupported BLMs. After that, we were able to push the middle water finger only to flush or to add molecules; the two perpendicular channels are no longer movable. The two electrodes are being inserted through the two perpendicular channels to record capacitance and conductance of bilayers.

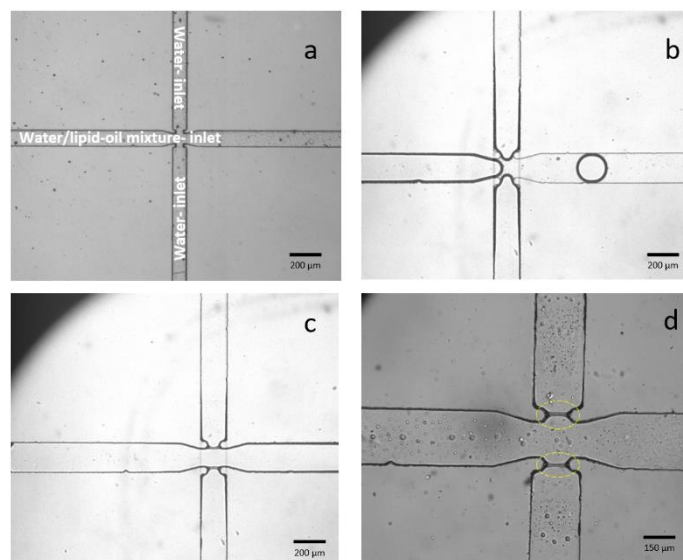


Figure 46: Microscopic Images for Cross-Geometry one-outlet Design. (a) Empty chip with illustrations for the different inlets. (b) After insertion of water fingers, the three interfaces, covered with lipids, come close to each other's to start zipping and formation of the BLMs. (c) The 2 BLMs are formed in the specified gap and the middle channel is still moving. (d) A closer look for the formed BLMs highlighted with yellow circles.

Despite the advantage of stability, the main limitation of this design is resembled in fixation of the two perpendicular channels. Being unable to flush the two channels is limiting the application of biomolecules to study their behaviour in lipid membranes. This is due to the one outlet design.

b. Cross-Geometry Two-outlets Design

This design is an update for the previous design. Instead of one outlet, we have designed another outlet with keeping the main features of the cross geometry (fig. 47). With this design we can change, if needed, the composition of the buffer solution for two fingers.

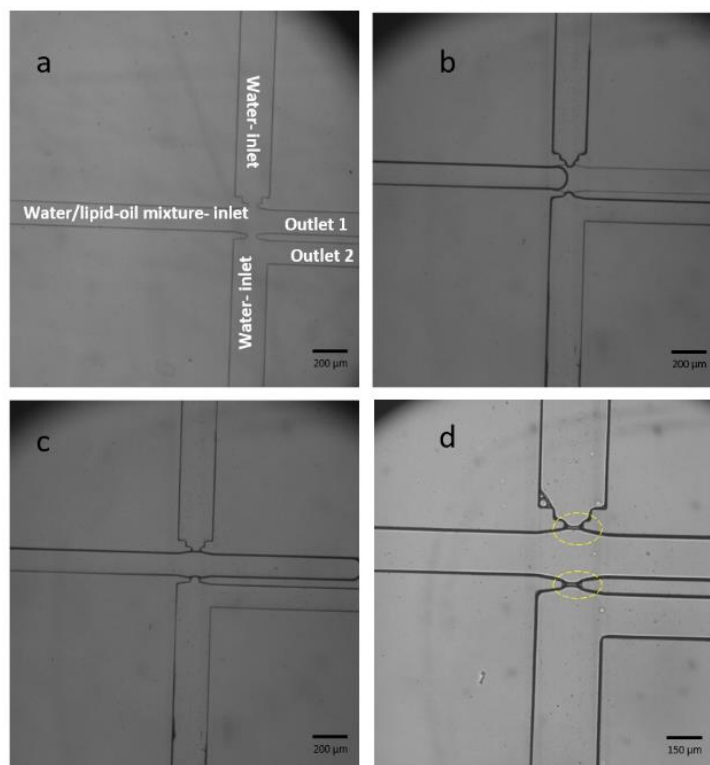


Figure 47: Microscopic Images for Cross-Geometry two-outlet Design. (a) Empty chip with illustrations for the different inlets and outlets. (b) After insertion of water fingers, the three interfaces, covered with lipids, come close to each other's to start zipping and formation of the BLMs. (c) The 2 BLMs are formed in the specified gap and the middle channel is still moving. (d) A closer look for the formed BLMs highlighted with yellow circles.

Chapter 4: Microfluidic Scheme for Studying the Interaction between Apatite Nanoparticles Loaded with Trehalose and Red Blood Cells¹

In this part, we used our microfluidic chip to study the transport of a drug across a free-standing lipid bilayer. In this case, we are measuring the transport properties of trehalose, a drug used as a cryoprotectant, through a lipid bilayer. In particular, we study how these transport properties are influenced by dispersing some apatite nanoparticles around our free-standing bilayer [12].

3.3. Red Blood Cells Cryopreservation

Cryopreservation of red blood cells (RBCs) is a fundamental process in prolonging the life time and availability of the RBCs for clinical and research needs [150, 12]. Not only RBCs, but also other living tissues. Without cryopreservation, RBCs can be conserved about 42 days, which means that the RBCs stock of hospital should be re-filled constantly. Indeed, RBCs have no nucleus and cannot self-replicate themselves. To overcome this problem, RBCs could be conserved by cryopreservation. Currently, Glycerol; a cryoprotectant, is used extensively in cryopreservation of RBCs [151]. However, glycerol should be removed from RBCs before transfusion to avoid intravascular haemolysis [12, 152]. Glycerol should be removed via dialysis, which makes this process slow (so not suitable for emergencies) and expensive. As a possible alternative, Trehalose, a biocompatible cryoprotectant, was used in many studies however its loading in cell is in general too small to allow stable cryopreservation. Due to this problem, we investigate to employ colloidal apatite nanoparticles (NP) to enhance a larger loading of trehalose in RBCs. Apatite NP have been found not to cross the membrane but to modulate its physical state [12]. As a result, the apatite NP promoted the Trehalose to move across lipid bilayers.

¹ *Stefanic M, Ward K, Tawfik H et al 2017 (Biomaterials)*

3.4. Experimental set-up

3.4.1. Formation of a free-standing lipid bilayer in the presence of apatite NP

Inside a microfluidic chip (fig. 48), a free-standing lipid bilayer membrane of DOPC or Monoolein has been formed and investigated in presence of increasing concentration of apatite NP in 2 different pH media, 6.5 and 7. To achieve this set-up, the apatite NPs are water soluble and were dispersed in the 2 aqueous fingers which are separated by a bilayer (DOPC or Monoolein). Optical microscopy and electrophysiological measurements were combined to determine the bilayer physical properties. It was found that, when the concentration of apatite NP was greater than 4-5 mg/ml, no bilayer could be formed. The larger NPs concentration to form a stable bilayer were, for our case, from 0.1 to 3 mg/ml. The bilayer formation was confirmed by electrical capacitance measurements C_s .

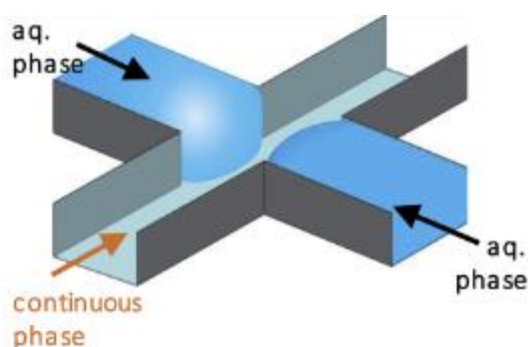


Figure 48 Illustration diagram for formation of free-standing lipid membrane in microfluidic chip, apatite NPs are dispersed in the aqueous phase, while the continuous phase is the oil in which the lipid molecules are dissolved. Copyrights Approved (Author). Stefanic M, Ward K, Tawfik H *et al* 2017 (Biomaterials)

3.5. Interactions between Apatite NPs and RBCs and Fluorescent Evidence

3.5.1. Interaction energy between apatite NP and synthetic lipid bilayers

Using the previous set-up enabled us to extract the average *free energy* (fig. 49). This method estimates the surface coverage with apatite NP. This is extracted from the change in magnitude of the electrical capacitance C_s which is also depends on NP

concentration. Then, the surface coverage is plotted as a function of NP concentration. By the assumption of dynamic equilibrium between free and adsorbed NP, then the *Langmuir Adsorption Model* could be applied and analyzed (table 3). According to this model, the surface is composed of series of distinct sites capable of binding the NP and giving the relationship between the surface coverage θ and NP concentration C :

$$\theta = \frac{K_L \cdot c}{1 + K_L \cdot c} \quad \text{Equation 17}$$

From the previous equation, we were able to obtain the equilibrium constant K_L . The corresponding free energy (ΔG°) for the adsorption of the apatite NP to the lipid bilayer surface is calculate by the following equation:

$$\Delta G^\circ = -RT \ln K_L \quad \text{Equation 18}$$

Table 3: Calculated value of equilibrium constant (Langmuir) K_L for the system NP/bilayer and related value of the standard free energy of interaction ΔG°

	Medium pH	K_L (L.mol ⁻¹)	ΔG° (KJ.mol ⁻¹)
DOPC	6.5	4. 10 ⁵	-32.0
DOPC	7.4	1.5. 10 ⁵	-29.5

Where R is the gas constant (8.314 JK⁻¹ mol⁻¹) and T the absolute temperature (in Kelvin). This procedure was applied for the two different pH we used (6.5 -7) and then we were able to measure adsorption behaviour of NP according to the pH. Results showed a larger adsorption at pH 6.5. This is indicating that apatite NP showed greater interaction with lipid molecules in more acidic medium. The measured interaction energies show a strong physico-absorption but still allowing a reversible NP adhesion.

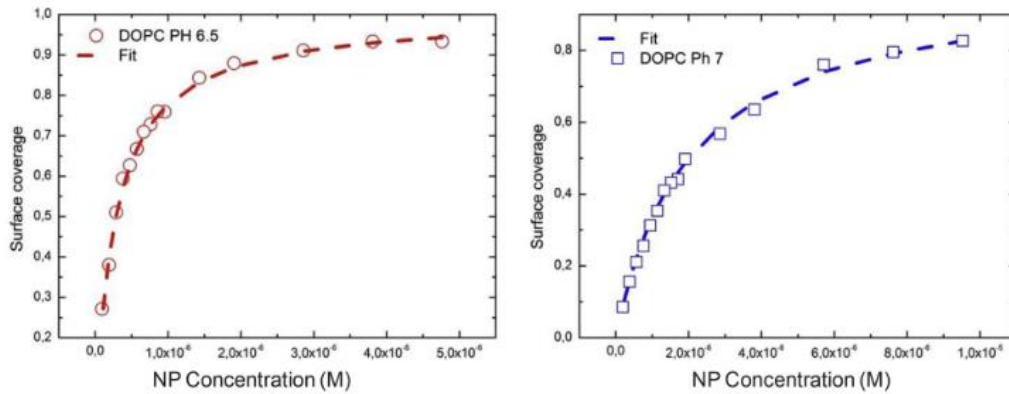


Figure 49: Langmuir isotherms describing the bilayer coverage as function of NPs concentrations and medium pH. Copyrights Approved (Author) Stefanic M, Ward K, Tawfik H *et al* 2017 (Biomaterials)

3.5.2. Translocation of Eu-doped apatite NP through the lipid bilayer

For more confirmation, we repeated the same procedure with fluorescent Eu-doped apatite NP (fig. 50). In that case, one droplet was composed of a medium with fluorescent Eu-doped apatite NP while the second one was composed of the same medium but without these fluorescent NPs. Under a fluorescent microscope we directly observed that the EU-NP remained in their compartment and did not cross the bilayer. We used three different lipids for more confirmation: Monoolein, DOPC and DPHPC. Even after several hours of observation with increasing the concentration of NP, no translocation was observed.

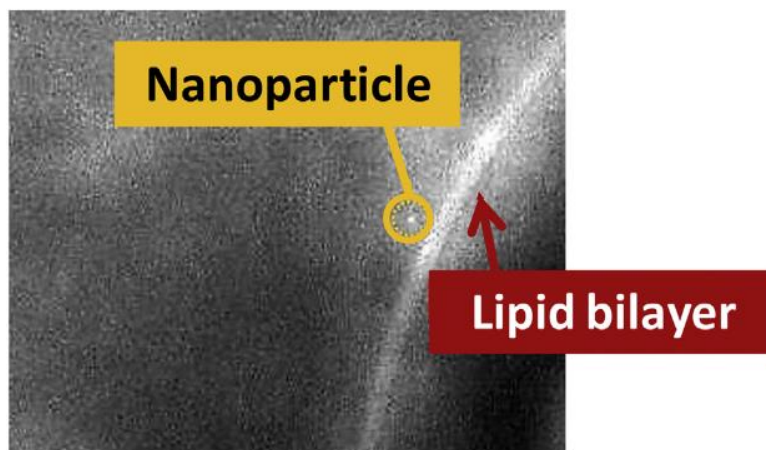


Figure 50: Fluorescing Eu-doped apatite NP attached to the lipid bilayer as evidence of non-crossing the lipid membrane. Copyrights Approved (Author) Stefanic M, Ward K, Tawfik H *et al* 2017 (Biomaterials)

3.5.3. Translocation of FITC through the lipid bilayer

As a Trehalose substitute, we used fluorescent FITC in the same previous set-up. One droplet contained the apatite NP (in pH 6.5 – 7) and solved FITC 2 mM (fig. 51). The second droplet contained only the medium without NP and FITC. Two outcomes have been noticed, the first one was transferring of FITC through the bilayer and the second observation was that the amount of FITC transferred seems to be proportional to the concentration of NP.

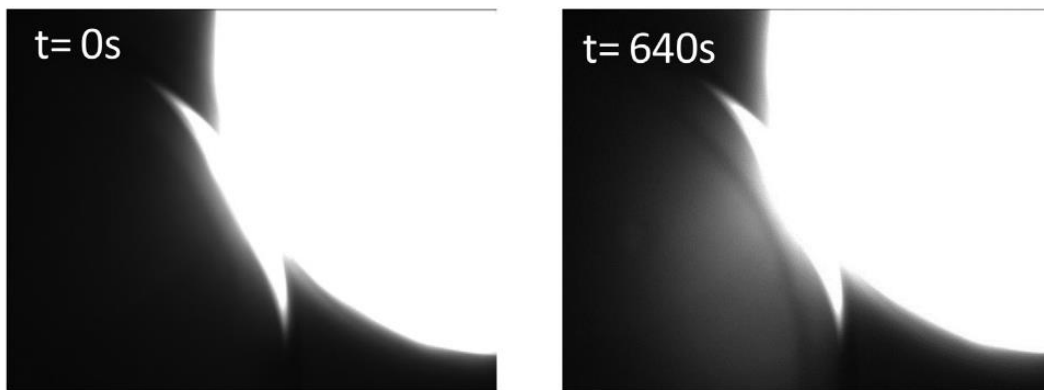


Figure 51: Two water droplets with their interfaces separated by a DOPC lipid bilayer one of them contains fluorescent FITC loaded on apatite NPs while the other is empty, at time= 0, the empty droplet is not fluorescent while over time a fluorescence is appearing as an evidence of translocation of FITC to the other droplet with help of the NPs. Copyrights Approved (Author) Stefanic M, Ward K, Tawfik H **et al** 2017 (Biomaterials)

Chapter 5: Effect of Different Proteins, compounds, and Oil Compositions on the Behaviour of Artificial Bilayer Lipid Membranes

In this chapter, we present the functional changes of ion channels embedded in artificial bilayer membranes in presence of oil inclusions.

5.1. Introduction and Concepts

In the first part of this chapter, we have studied the consequence of the addition of Silicone oil; Si AR20 (Sigma Aldrich, Germany), on the physical properties of a bilayer lipid membrane. [153, 154].

In the second part, we have studied the consequence of an oil inclusion; Si AR20, on the ion channel-functionality, like Gramicidin A ion channel, embedded in a heterogeneous lipid bilayer.²

In the third part, we have studied the interaction of Coenzyme Q10 CoQ10 (Sigma Aldrich, Germany) on artificial bilayer lipid membranes. CoQ10 is a fat soluble compound and so it is present in the lipid membrane as an electron carrier [134, 135]. The importance of CoQ10 in biological processes; such as being a member in Electron Transport Chain (ETC) and stabilization of cell membrane [134], is leading to dedication of more researches to explore its interaction within lipid membranes [134].

5.2. Effect of Silicone Oil on Membrane-Tension of Artificial BLM

Here, we present interfacial tension (IFT) γ measurements and free energy gain measurements to study, quantitatively, different silicone oil concentrations effect on artificial BLM. For this purpose, we have used the same silicon oil composition but from two different manufacturers: Sigma Aldrich (Si AR20) and Wacker Silicones (Si AK20). We have used two different concentration of Si AR20 0.1% and 1% volume ratio to squalene. Also, we have used for this purpose three different electrolyte

² *Transport properties of Gramicidin A ion channel in a free-standing lipid bilayer filled with oil inclusions. Harvey Tawfik, Sevede Puza, Ralf Seemann, Jean-Baptiste Fleury (Front. Cell Dev. Biol. 2020)*

solutions: lithium chloride (LiCl), sodium chloride (NaCl) and potassium chloride (KCl). All of them are containing monovalent charges to suit gramicidin A ion channel. The lipid oil mixture is DOPC in squalene 5 mg/ml. The different electrolyte solutions (100 mM each) contained 10^{-6} M gramicidin A.

5.2.1. Interfacial Tension of LiCl Droplet in DOPC/Squalene.

In this experiment, using pendant droplet technique, we compared the effect of the two different Si AR20 concentration (0.1 and 1%) on interfacial tension of LiCl droplet. We have found that, with the increase of Si AR20 concentrations from 0 to 1%, there was a decrease in interfacial tension of the electrolyte solution droplet. We tried to fix the droplet volume to a $45 \mu\text{l} \pm 5 \mu\text{l}$. Also as shown in (fig. 52, 53 and 54) each one had been measured about 8 times for each concentration and an average were calculated in (table 1). All experiments were done in room temperature of 22°C . IFT is measured as a function of time.

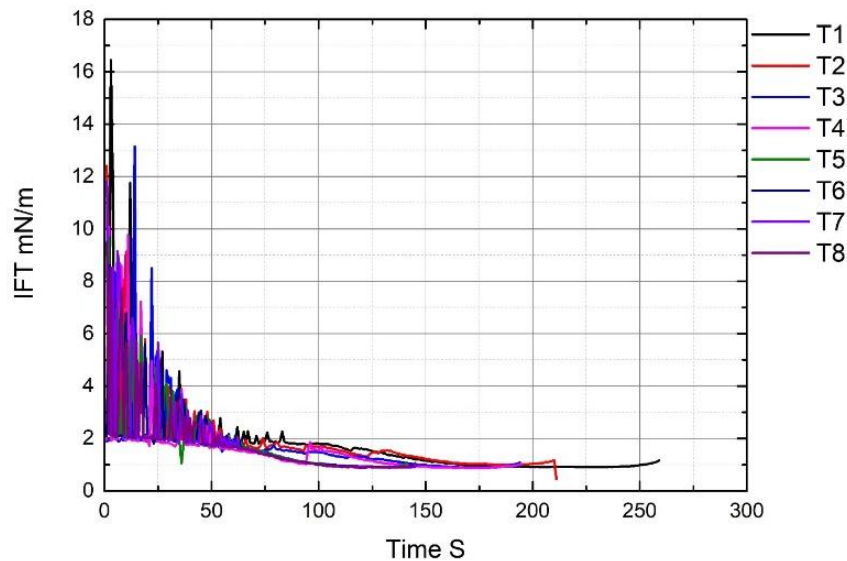


Figure 52: Interfacial Tension Measurements of LiCl droplet in DOPC/Squalene/Si Ar20 0%. 8 different trails T1 to T8 were done to make an average with standard error.

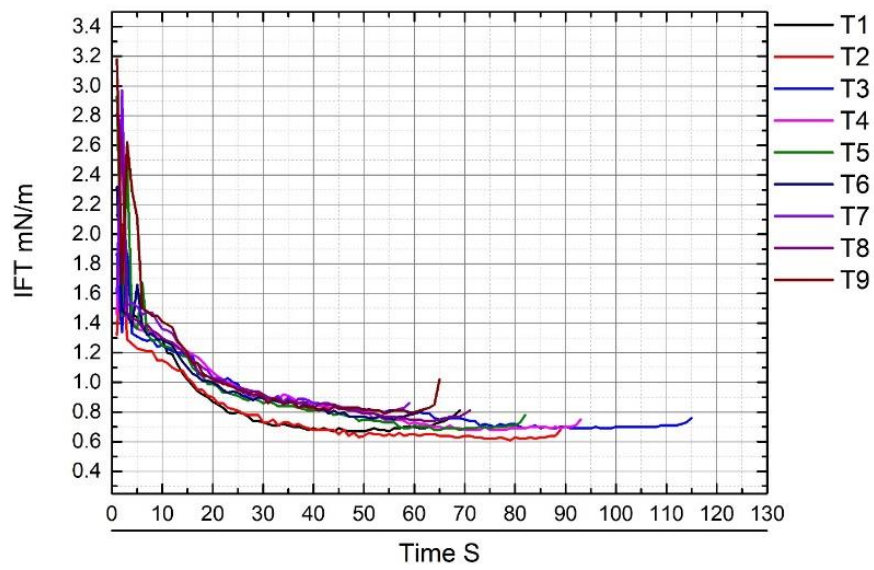


Figure 53: Interfacial Tension Measurements of LiCl droplet in DOPC/Squalene/Si Ar20 0.1%. 9 different trails T1 to T8 were done to make an average with standard error.

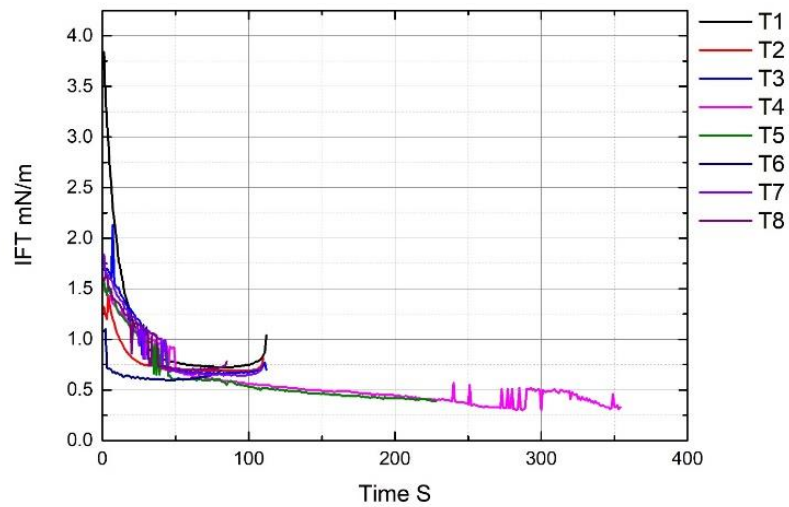


Figure 54: Interfacial Tension Measurements of LiCl droplet in DOPC/Squalene/Si Ar20 1%. 8 different trails T1 to T8 were done to make an average with standard error.

In (table 4), we have summarised the average of each IFT measurements for LiCl 100 mM with three different concentrations of SI AR20 0, 0.1 and 1% with standard error (SE):

Table 4: Interfacial tension measurements of LiCl droplets as a function of Si AR20 percentage:

Si. oil %	IFT (SE)
0% Si AR20	1.16 ± 0.26 mN/m
0.1%Si AR20	0.70 ± 0.05 mN/m
1% Si AR20	0.66 ± 0.04 mN/m

5.2.2. Interfacial Tension of NaCl Droplet in DOPC/Squalene

In this experiment, we compared the effect of the two different Si AR20 concentration (0.1 and 1%) on interfacial tension of NaCl droplet. We have found that, with the increase of Si AR20 concentrations from 0 to 1%, there was a decrease in interfacial tension. We tried to fix the droplet volume to a $45 \mu\text{l} \pm 5 \mu\text{l}$. Also as shown in (fig. 55, 56 and 57) each one had been measured about 8 times for each concentration and an average were calculated in (table 5). All experiments were done in room temperature of 22 °C. IFT is measured as a function of time.

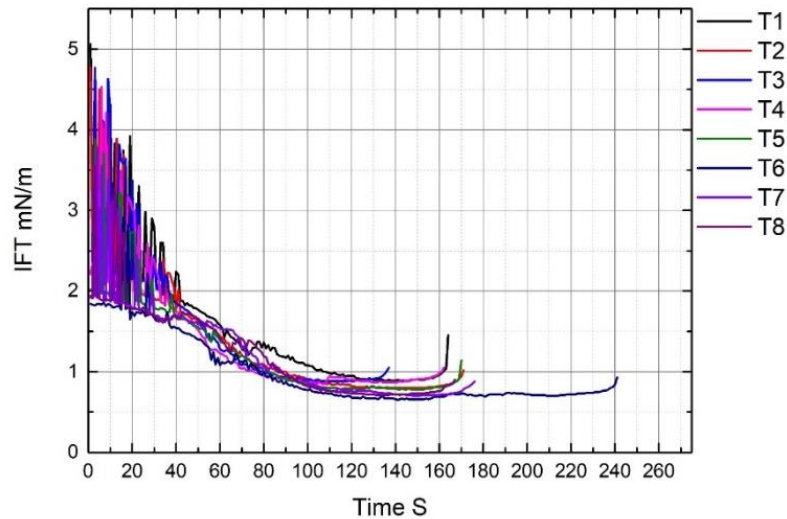


Figure 55: Interfacial Tension Measurements of NaCl droplet in DOPC/Squalene/Si AR20 0%. 8 different trails T1 to T8 were done to make an average with standard error.

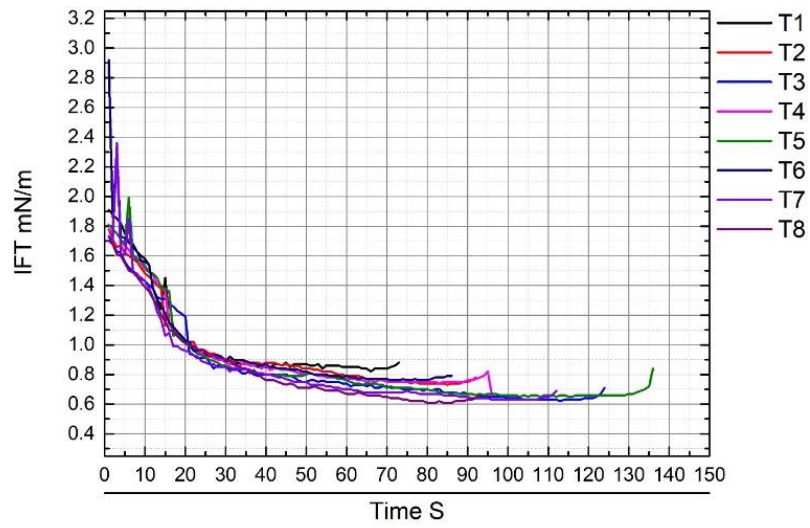


Figure 56: Interfacial Tension Measurements of NaCl droplet in DOPC/Squalene/Si AR20 0.1%. 8 different trails T1 to T8 were done to make an average with standard error.

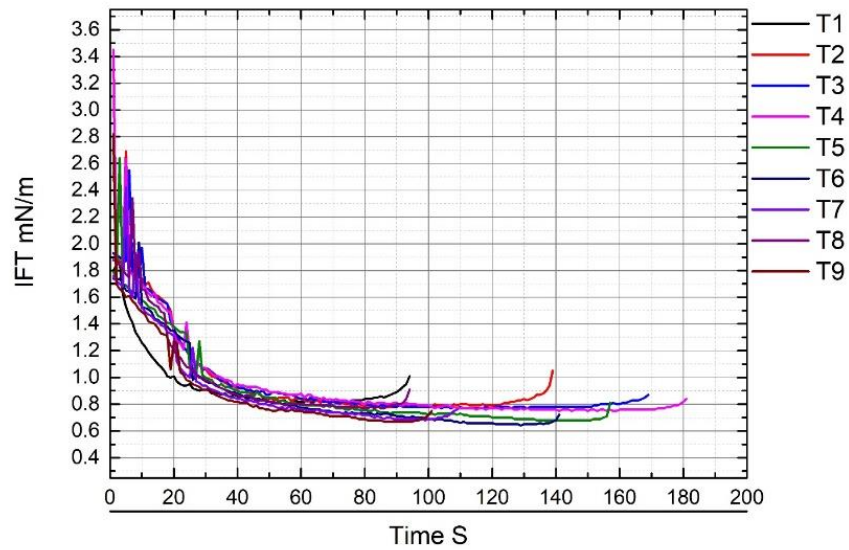


Figure 57: Interfacial Tension Measurements of NaCl droplet in DOPC/Squalene/Si AR20 1%. 8 different trails T1 to T8 were done to make an average with standard error.

In (table 5), we have summarised the average of each IFT measurements for NaCl 100 mM pendant droplet with three different concentrations of SI AR20 0, 0.1 and 1% with standard error (SE). We have noticed a slight increase in γ for the 1% Si AR20 over the 0.1% Si AR20 because of slight increase in the droplet volume of first droplet (in 1% Si AR20) by $\pm 7 \mu\text{l}$.

Table 5: Interfacial tension measurements of NaCl droplets as a function of Si AR20 percentage:

Si. oil %	IFT (SE)
0% Si AR20	0.82 ± 0.08 mN/m
0.1%Si AR20	0.77 ± 0.05 mN/m
1% Si AR20	0.79 ± 0.04 mN/m

5.2.3. Interfacial Tension of KCl Droplet in DOPC/Squalene

In this experiment, we compared the effect of the two different Si AR20 concentration (0.1 and 1%) on interfacial tension of KCl droplet. We have found that, with the increase of Si AR20 concentrations from 0 to 1%, there was a decrease in interfacial tension. We tried to fix the droplet volume to a $45 \mu\text{l} \pm 5 \mu\text{l}$. Also as shown in (fig. 58, 59 and 60), each one had been measured about 8 times for each concentration and an average were calculated in (table 6). All experiments were done in room temperature of 22 °C. IFT is measured as a function of time.

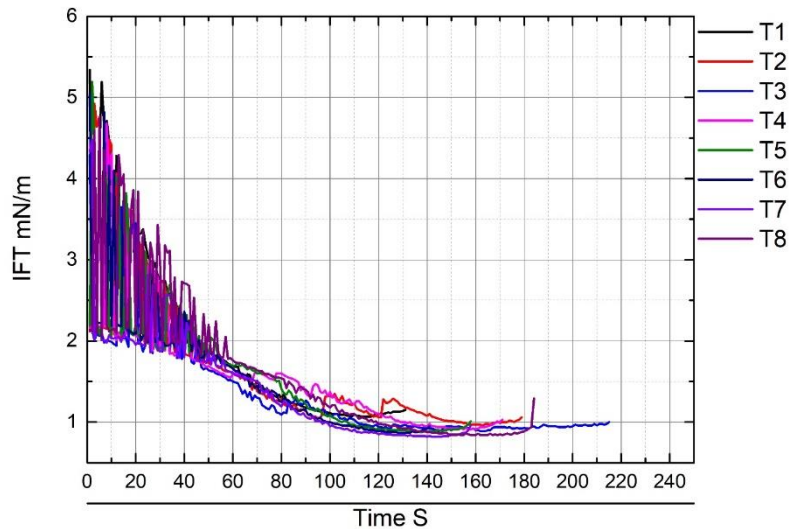


Figure 58: Interfacial Tension Measurements of KCl droplet in DOPC/Squalene/Si AR20 0%. 8 different trails T1 to T8 were done to make an average with standard error.

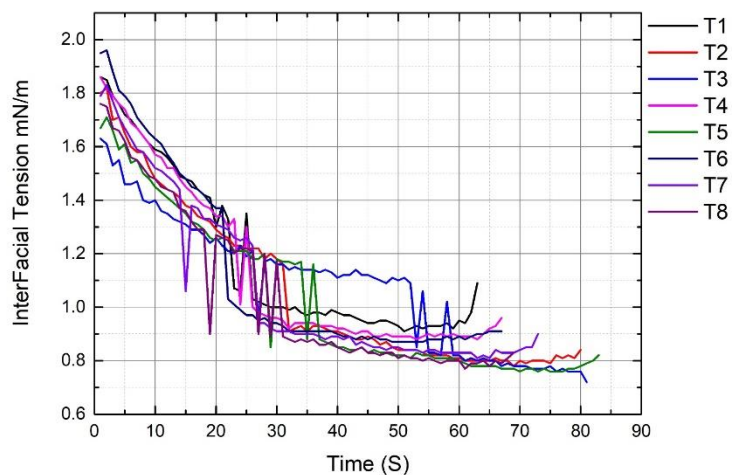


Figure 59: Interfacial Tension Measurements of KCl droplet in DOPC/Squalene/Si AR20 0.1%. 8 different trails T1 to T8 were done to make an average with standard error.

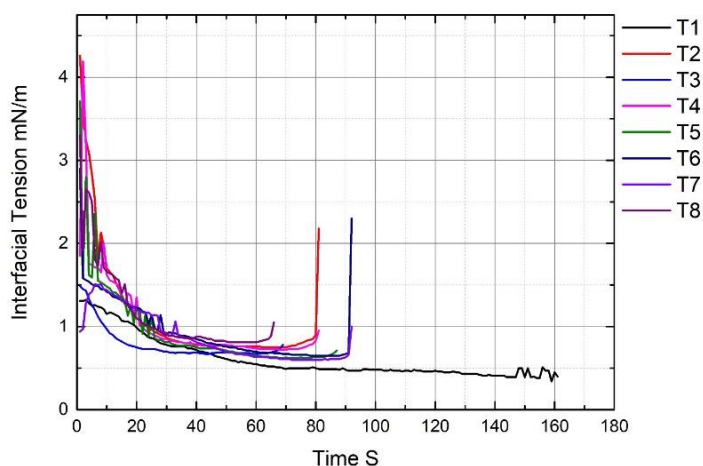


Figure 60: Interfacial Tension Measurements of KCl droplet in DOPC/Squalene/Si AR20 1%. 8 different trails T1 to T8 were done to make an average with standard error.

In (table 6), we have summarised the average of each IFT measurements for KCl 100 mM pendant droplet with three different concentrations of SI AR20 0, 0.1 and 1% with standard error (SE). Average of droplet size was fixed to $45 \pm 7 \mu\text{l}$:

Table 6: Interfacial tension measurements of KCl droplets as a function of Si AR20 percentage:

Si. oil %	IFT (SE)
0% Si AR20	1.06 ± 0.12 mN/m
0.1%Si AR20	0.88 ± 0.07 mN/m
1% Si AR20	0.72 ± 0.07 mN/m

We tried different electrolyte solutions with different molecular size from the smallest Li to K according to the period table. We noticed a decrease in surface tension of electrolyte droplets with the increase of Si AR20 concentration; generally, below 88 mN/m.

5.2.4. Contact Angle Measurements and Free-Energy Gain Calculations.

More measurements were dedicated to study the effect of silicone oil on bilayer lipid membranes. After measuring the interfacial tension, we measured the contact angle θ (Figure 61) to calculate membrane tension Γ . We used two-channel chip, to calculate the contact angle θ for the three electrolyte solutions: Li⁺, Na⁺ and K⁺.

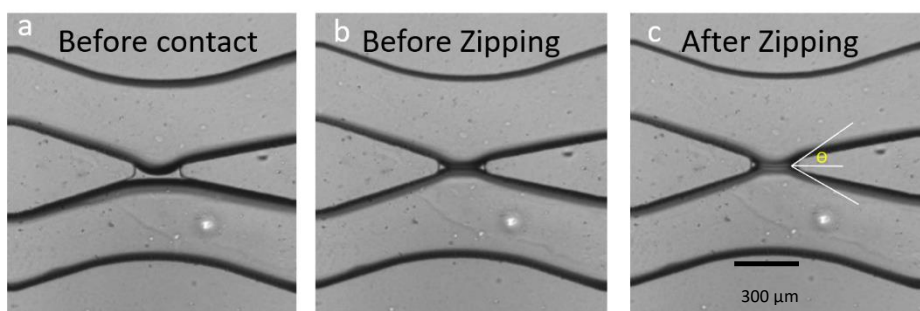


Figure 61: Formation of a bilayer lipid membrane for measuring membrane tension. A) The two monolayers are decorating the two electrolyte solutions before contacting each other. B) The two monolayers touched each other but not zipped yet to form a BLM. C) The BLM formed by zipping and contact angle was measured.

Regardless the electrolyte solution and oil composition, figure 10 is showing the exact setup was used to measure membrane free energy; membrane tension (Equation 19) and consequently the free-energy gain (Equation 20):

$$\Gamma = 2\gamma \text{Cos } \theta \quad \text{Equation 19}$$

$$\Delta F = 2\gamma - \Gamma \quad \text{Equation 20}$$

By using the above equations, we found out that the contact angle with 0% Si oil is lower than the contact angle with 0.1% and 1% Si oil. Table 7 is showing the difference in free energy gain between a BLM formed in absence of Si oil and in presence of 1% silicon oil:

Table 7: the free energy-gain before formation of a BLM in presence/absence of Si AR20:

Si Oil %	Free Energy Gain	S.Err	BLM Formation
0%	1.12	± 1.05	After
1%	1.9	± 1.2	After

In case of no silicone oil, we noticed that after the formation of the BLM, the free energy gain has decreased due to increased membrane tension. On the other hand, due to decrease in membrane tension as no effect of silicone oil, the free in energy gain has increased. To reach a conclusion with this section, we have found that silicone oil is decreasing interfacial tension, membrane tension and free energy gain, respectively.

5.3. Effect of Silicone Oil on Gramicidin A Functionality in BLM.

In this section, we demonstrate our results after the addition of silicone oil, Si AR20, to DOPC or Monoolein/Squalene system in presence of a two-subunit ion channel; gramicidin A (gA). Such addition has led to *nanoscopic oil inclusions* between lipid molecules. Consequently, this created nano-lipid domains that have altered the behaviour of gA ion channels.

We studied such behaviour from a different perspective; we have used five different electrolyte solutions to check their transport through gA ion channels in absence/presence of and see if they would be affected. For this purpose, we used the

same geometry as before and the lipid/oil composition is DOPC 5 mg/ml or monoolein 8 mg/ml in squalene and the electrolyte solution is 100 mM: LiCl, NaCl, KCl, RbCl and CsCl.

5.3.1. Effect of Silicone oil on Current Measurements through Gramicidin A Ion Channels.

Gramicidin A ion channel (gA), as mentioned in chapter 2, is composed of two subunits that found each other in both leaflets of the BLM and fuse to form an ion channel. This ion channel is transporting monovalent ions and blocked by divalent ions. Utilizing the current measurement option in our patch clamp, we were able to measure the presence of functional gA inside a BLM (fig. 62).

In (fig. 62a), we have generated electroporation by applying a large voltage across a lipid bilayer. When we applied a higher voltage like 200 mV, certain pores had been formed in the membrane and yielded a current that hit the 120 nA. In figure 62 b, we have inserted gA ion channels with average concentration of 10^{-6} M. This led to measuring current proportional to the applied voltage according to Ohm's law.

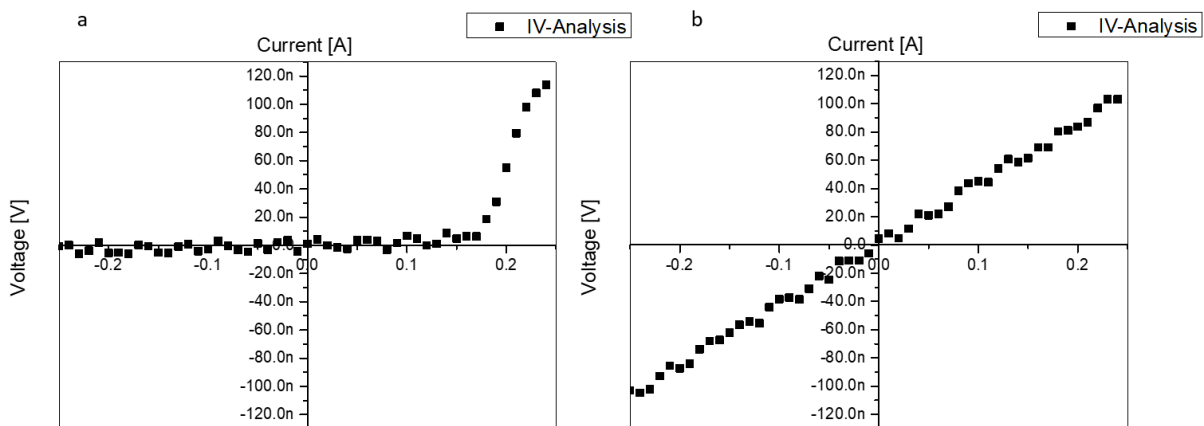


Figure 62: IV-Analysis of monoolein BLM with and without gramicidin A. A) Electroporation curve due to absence of ion channel through which current would flow from one side to the other. The increase by application of 200mV is indicating the existence of pores in the membrane but not due to gA. B) IV-Curve showing the effect of gA on current measurements. The current measured is proportional to the applied voltage.

We repeated the same experiment with gA but with addition of Si AR20 5% to check whether it would affect the IV-curve. Figure 63 is showing a comparison between the (fig. 62b) and the new IV-curve for the same Lipid/oil/buffer composition with addition of Si Ar20 5% in presence of gA 10^{-6} M.

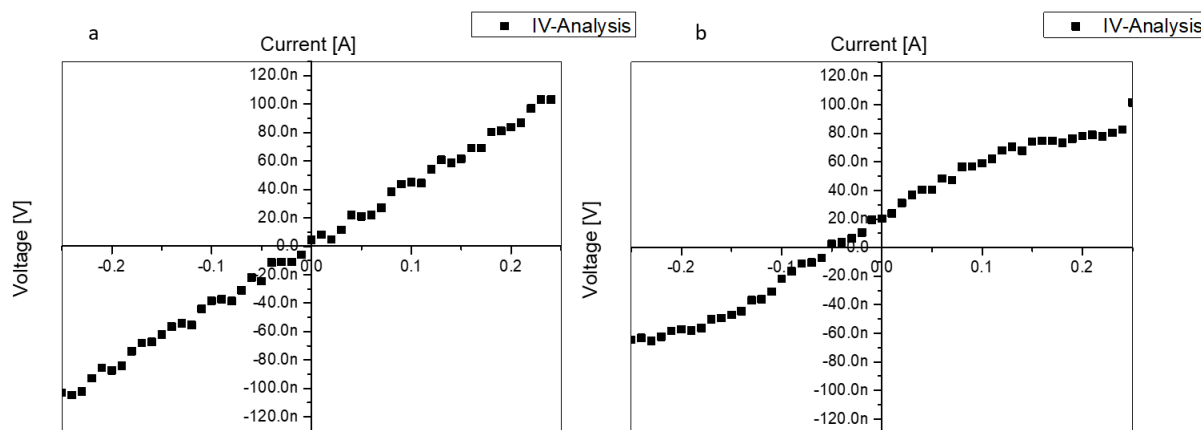


Figure 63: IV-Analysis of monoolein BLM with and without silicon oil in presence of gramicidin A. A) IV-Curve showing the effect of gA on current measurements. The current measured is proportional to the applied voltage. No Si AR20 was added during this measurement. B) In presence of Si Ar20 there is a minor shift in the IV curve. This is an indication for the assembly of Si Ar20 between lipid molecules which may affect the functionality of gA ion channels.

Figure 63a, is an IV-analysis for monoolein/squalene BLM with gA ion channels inserted in the membrane. In (fig. 63b), is an IV- analysis curve we recorded after repeating the same experiment in presence of Si AR20 5%. We observed a shift in the IV analysis with lower current recorded upon applying the same voltage. This shift we could refer to the contention and competition of Si AR20 and gA molecules in BLMs. From (fig. 63b), we have concluded that the addition of Si AR20 is somehow changing the behaviour of BLM.

Step-by-step, we recorded the insertion of gA in BLM utilizing the IV-analysis technique (fig. 64). In figure 64a, the green points are the recorded current upon application of voltage during zipping of the two monolayers and of course before formation of gA ion channels. After a while, after zipping, we have recorded a slight proportional current-voltage curve due to starting the assembly of gA ions within the

BLM (fig. 64b). After few seconds, we repeated the measurements to find out that gA ion channels were formed and functional (fig. 64c).

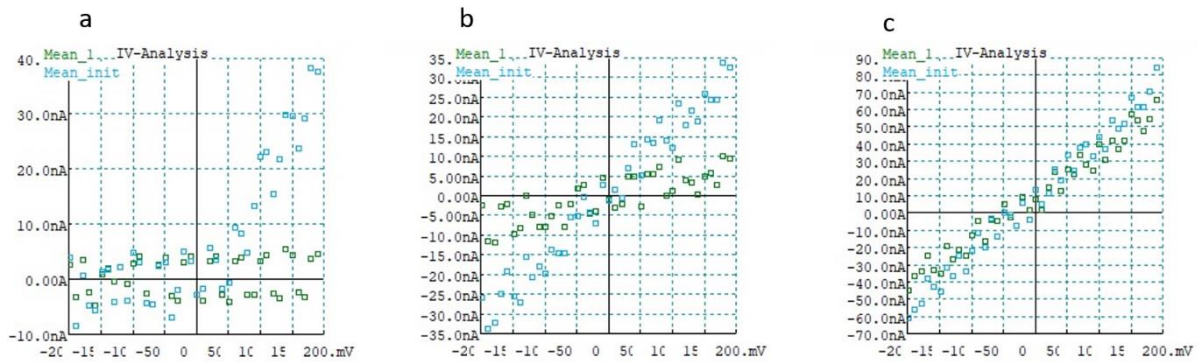


Figure 64: Patchmaster-Software images for IV-analysis of monoolein BLM in presence of gA ion channels. A) The green points are indicating the current measured upon application of voltage during membrane zipping process. B) After the zipping, gA ion channels started the assembly process and this could be noticed from the slight current (10 nA) recorded. C) After the assembly of gA ion channels, the proportional IV relation started to be noticed.

5.3.2. Effect of Calcium Ions on Functional gA Channels in BLM.

To make sure that all these gA ion channels inserted and functioning, we changed the buffer composition around the formed lipid bilayer, via our microfluidics pumps. After dispersing a buffer containing Ca^{+2} ions in both sides of the bilayer, we measured a disappearance of the bilayer conductance (fig. 65). In this experiment the silicone oil effect was neglected.

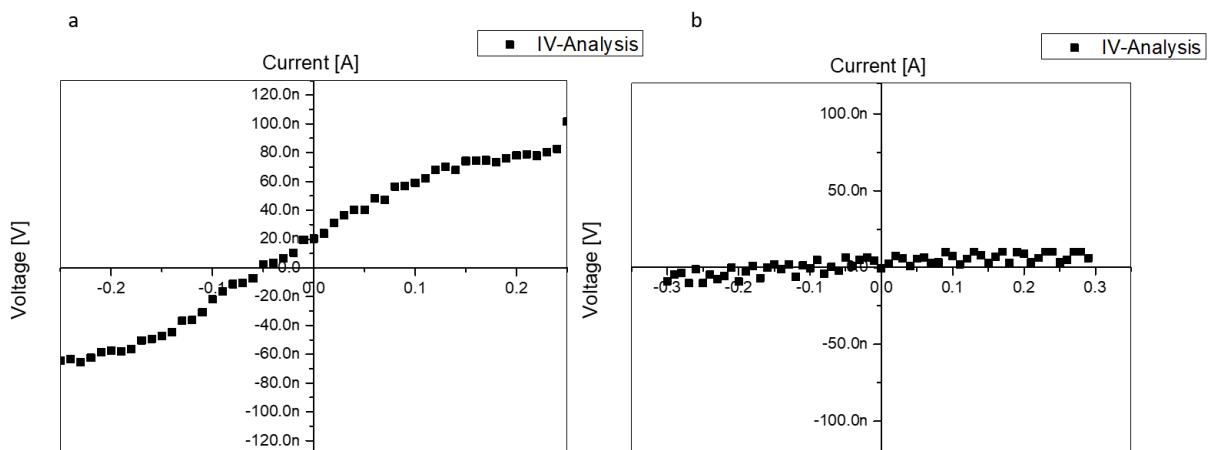


Figure 65: IV curves for monoolein BLM + Squalene + Si Ar20 in absence and presence of Ca^{+2} . A) IV analysis for monoolein BLM in presence of Si AR20 and functional gA ion channels. B) After addition of Ca^{+2} to the system, all gA ion channels were blocked by Ca^{+2} to reach almost zero ampere.

5.3.3. Different Ions Transfer Through Gramicidin A Ion Channels in BLM

To study the effect of SiAR20 oil inclusion in a lipid bilayer containing functional gA ion channels, we used five different monovalent ions (from group 1 in periodic table). These ions are: LiCl, NaCl, KCl, RbCl and CsCl and they increase in atomic weight from Li⁺ to Cs⁺.

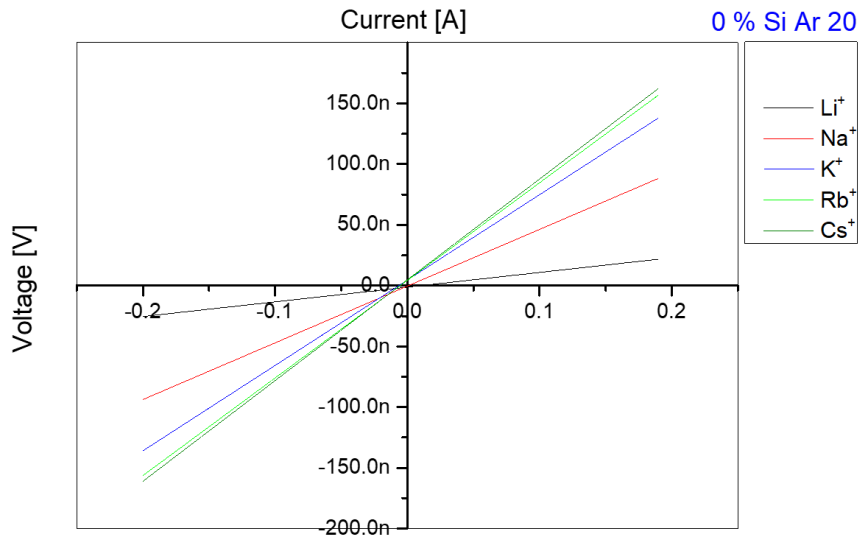


Figure 66: IV-Analysis for different ions transfer through gA ion channels in absence of Si Oil. According to the atomic weight, the transfer velocity from through gA ion channels is increasing with increase in atomic weight until reaching Rb⁺ and Cs⁺ which have a very close transfer rate and sometimes Rb⁺ is faster than Cs⁺.

In (fig. 66), we tried the five monovalent ion-transfer through gA ion channels (10^{-10} to 10^{-12} M) fitted in monoolein BLM. We found that with increasing the atomic weight, the ion transfer velocity is increasing too; except with Cs⁺ and Rb⁺. This means that in most of cases Rb⁺ > Cs⁺ > K⁺ > Na⁺ > Li⁺ [15]. In our measurements we found that Cs⁺ and Rb⁺ have close conductance, so we were measuring other ions in comparison to each other and in comparison, with Cs⁺ and Rb⁺.

We used Si AR20 in different volume concentrations: 0.1%, 0.2%, 0.3%, 5% and 10%. For each oil concentration, we used the five ions to study their transfer through the gA ion channels. We compared the conductance elements of each ion with the other

and for each ion in different Si oil concentrations through measuring the slope in IV curves.

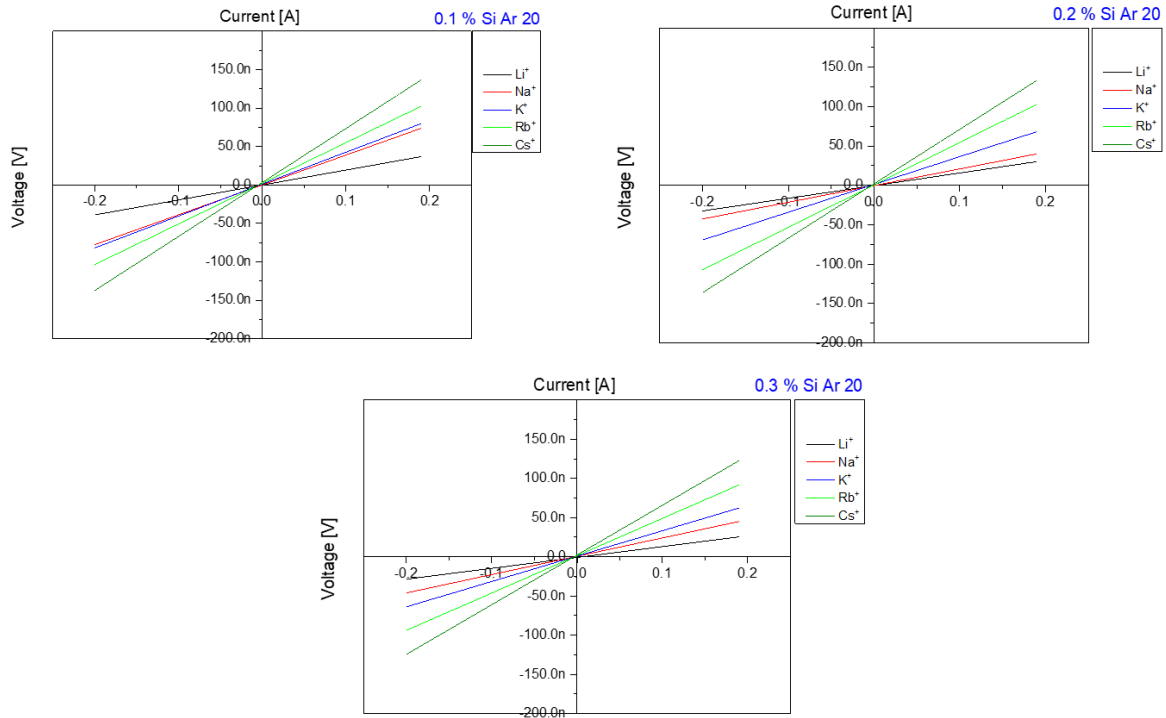


Figure 67: IV-Analysis of different ions transfer through gA ion channels in monoolein BLM. Upon addition of very low concentrations of Si AR20; 0.1, 0.2 and 0.3%, we did not notice a major difference in conductance of gA ion channels. All conductance measurements are within the same order like in 0% Si Ar20.

In (fig. 67), we slightly increased Si AR20 concentration from 0 to 0.3% to see if it would lead to major change in gA conductance. We have notice very slight or minor change in gA conductance for all ions. For this reason, we compared the slope; change in conductance, for each ion in each Si AR20 concentration (fig. 68). From the graph, we can conclude that, at 0% Si AR20, all ions have higher conductance when compared to 0.1, 0.2 and 0.3% Si AR20 despite having close conductance to each other's.

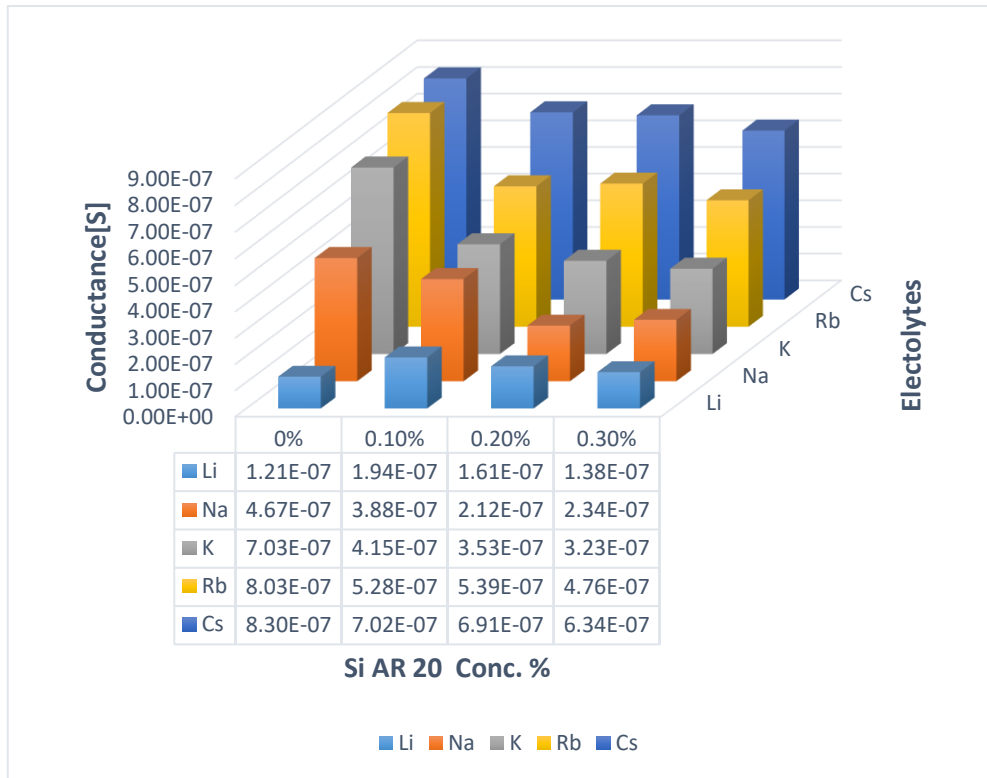


Figure 68: The difference in conductance between the 5 ions in 4 different oil compositions. We can notice that Li^+ have the lowest conductance in all oil compositions, while Rb and Cs are the higher in conductance. K^+ conductance had decreased after the addition of Si AR20. In general, there is a decrease in conductance for all ions after the addition of Si AR20 except in Li^+ which has the lowest conductance.

To test the effect of more Si oil concentration, we increased the percentage of Si Ar20 to 5% and 10% and measured the conductance again for all ions (fig. 69).

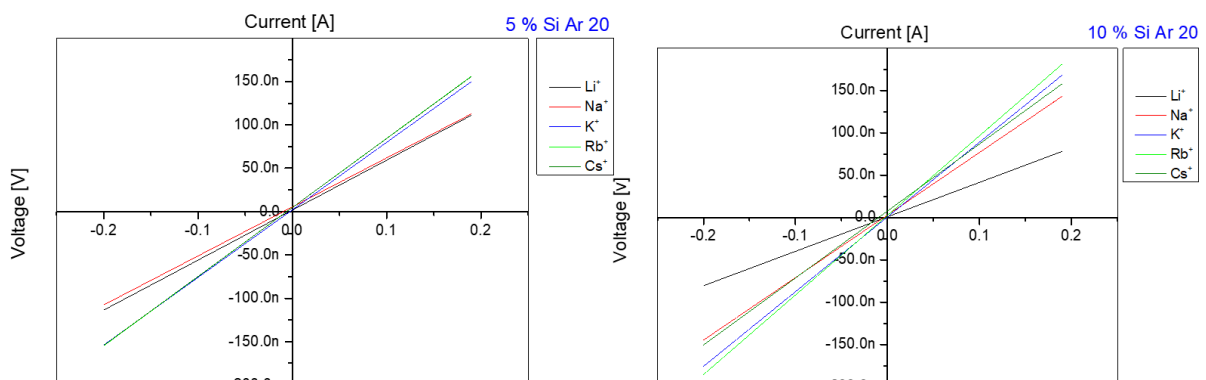


Figure 69: IV-Analysis of different ions transfer through gA ion channels in monoolein BLM. Upon addition of higher concentrations of Si AR20; 5 and 10%, we noticed a major differences in conductance of gA ion channels. The predicted conductance for each has increased and lost the stated order for conductance. An increase in Li^+ conductance was detected. There is increase in the conductance of K^+ higher than Cs^+ in both 5 and 10%.

As previous, we involved change in conductance; slope, to see the difference between 0% Si AR20 and 5 and 10% Si AR20 as shown in (fig. 70):

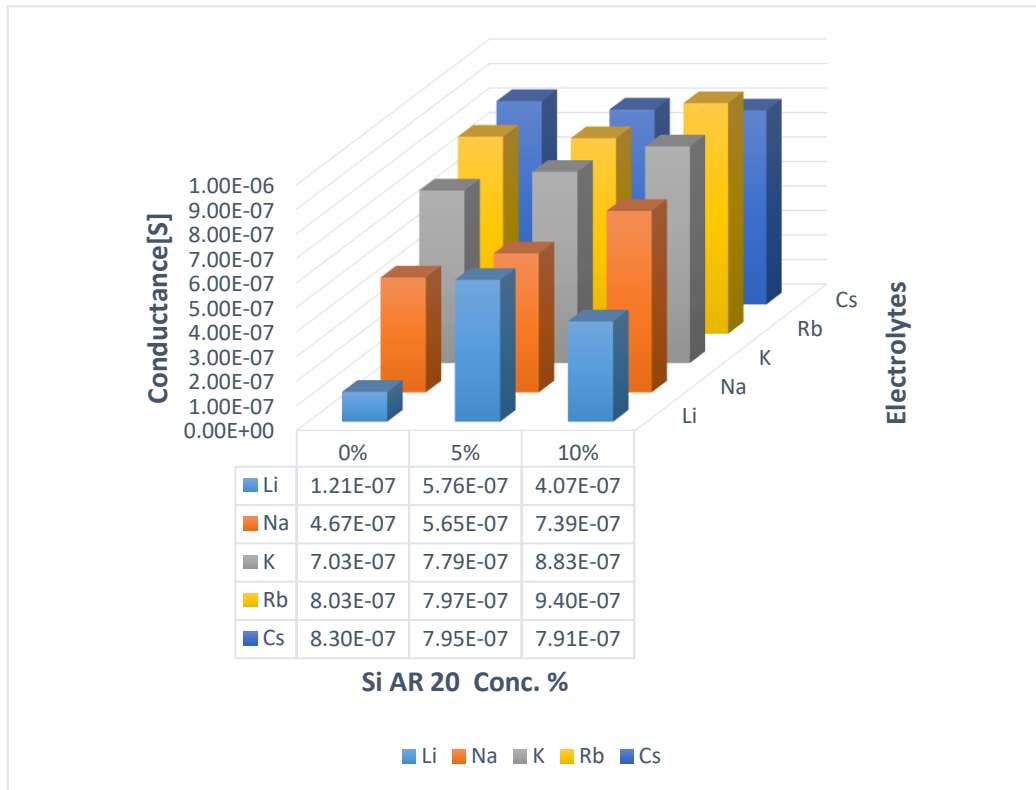


Figure 70: The differences in conductance between the 5 ions in 3 different oil compositions. Li^+ conductance has increased by folds while still the lower in conductance when compared to the other ions. There was also an increase in the conductance of Na^+ and K^+ with increase of Si AR20 concentration when compared to 0%. K^+ has recorded higher conductance than Cs^+ with 5 and 10% Si AR20 concentrations. Rb^+ has recorded the higher conductance at 5 and 10% Si AR20.

We recorded some capacitance measurements to check whether the thickness of the membrane (d_m) (Equation 15) has been changed after the addition of Si oil or not. We created a BLM of DOPC (5 mg/ml) in squalene (95% and 90%) and Si AK20 (5% and 10%), respectively. We have recorded capacitance for 0%, 5% and 10% Si oil and what we found out is that, in the presence of silicone oil, the thickness (d) of the DOPC BLM was higher by about 1 nm; 6 nm (Normal DOPC membrane thickness is 5 nm) despite the fact of lower membrane tension. All previous results have confirmed our assumption that Si AR20 inclusion within the bilayer membrane has created micro- or nano- lipid-domains which consequently have changed the behaviour/functionality of gA ion channels in transporting ions across a bilayer lipid membrane.

5.4. Effect of Coenzyme Q10 on Unsupported Bilayer Membranes.

As mentioned in chapter 2 (Section 2.2.2.b), coenzyme Q10 (CoQ10) is a fat-soluble compound and due to this feature, we were able to dissolve with the lipid/oil mixture to study their effect on lipid membranes. For such experiments, we are using DPhPC dissolved in squalene (15 mg/ml) in the cross-geometry microfluidic chip (fig. 71). The electrolyte solution for these experiments was NaCl 100 mM. We tried to use CoQ10 in different, wide range of concentrations but in higher concentrations (0.1, 0.01, 0.005 and 0.002 mg/ml), we failed to have a stable BLM; we used 0.001 and 0.0005 mg/ml.

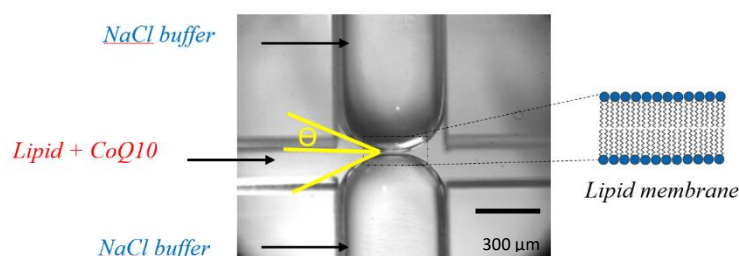


Figure 71: A microscopic image for the setup used for studying the effect of CoQ10 on BLM. Due to lipophilic nature of CoQ10, it is being dissolved in the lipid/oil mixture and perfused in this chip. The contact angle θ was measured to calculate membrane tension.

We have measured the capacitance C and specific capacitance C_s for three different oil compositions: 0, 0.001 and 0.0005 mg/ml CoQ10. We found out that C_s is increasing with the increase of CoQ10 concentration (fig. 72). Contact angle measurements have confirmed the previous assumption; we have found that with increasing the concentration of CoQ10, the membrane thickness (d) is decreasing and consequently the contact angle θ increases (table 8). We have measured the interfacial tension; using pendant droplet technique, for each CoQ10 concentration; 0, 0.001 and

0.0005 mg/ml, to calculate the membrane tension Γ . For each concentration, we measured three different times and the averages were calculated (fig. 73).

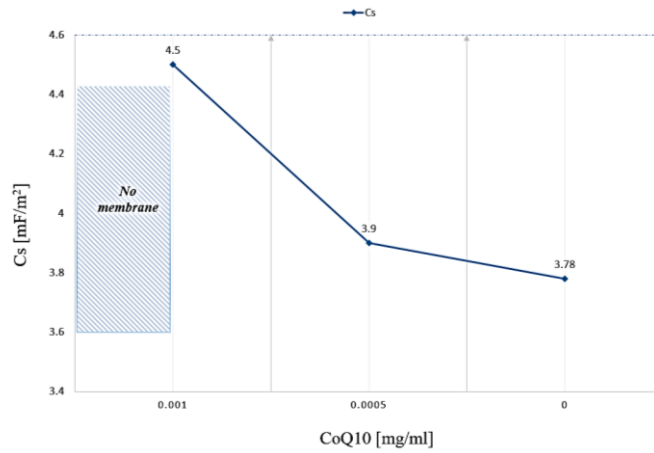


Figure 72: Specific capacitance plotted as a function of CoQ10 concentration in the BLM. Cs was found to be increasing with the increase CoQ10 concentration. Above CoQ10 concentration of 0.001 mg/ml there were no membranes formed due to higher concentration

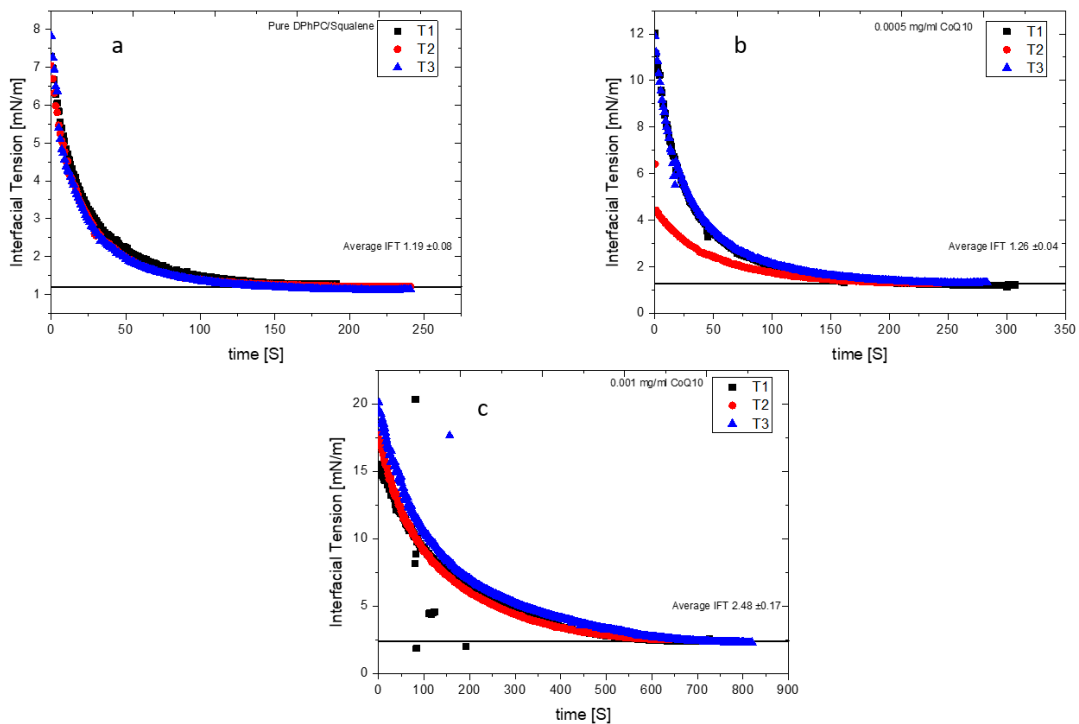


Figure 73: Interfacial tension measurements for different CoQ10 concentrations in DPhPC/Squalene system. A) Three different measurements and average extraction of pure DPhPC/Squalene droplet. B) Three different measurements and average extraction of 0.0005mg/ml CoQ10 in DPhPC/Squalene droplet. C) Three different measurements and average extraction of 0.001mg/ml CoQ10 in DPhPC/Squalene droplet. From the above measurements, the interfacial tension of DPhPC/Squalene is increasing with increase of CoQ10 concentration.

From the interfacial tension measurements, we have reached an explanation for the observed phenomena. We found that, with the increase in concentration of CoQ10 to 0.0005 mg/ml, there is a slight increase in interfacial tension (fig. 73b). This increased has continued with the increase of the added concentration CoQ10 to 0.001 mg/ml (fig. 73c). As a result, to these increases, the contact angle θ has increased because of decreased membrane thickness d .

Figure 74, the averages of interfacial tensions (fig. 74a) and membrane tensions measurements (fig. 74b) were plotted as a function of CoQ10 concentration. In (table 8), a summary for all obtained results:

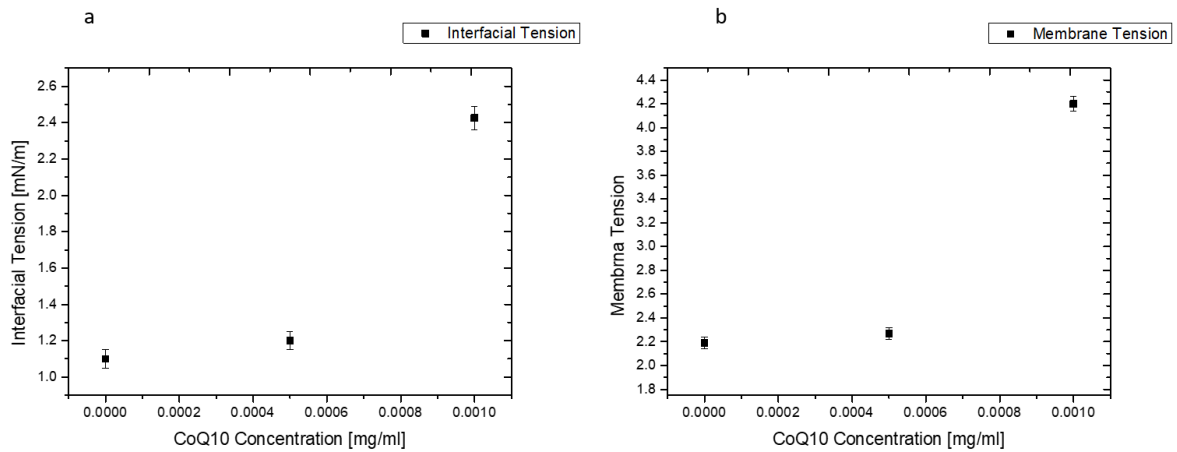


Figure 74: Effect of CoQ10 on interfacial tension and membrane tension of DPhPC/Squalene system. A) Plotting for interfacial tension for three different concentrations as a function of CoQ10 concentration with standard error. With the increase in CoQ10 concentration, there was increase in interfacial tension of DPhPC/Squalene droplet. B) Membrane tension for the three different concentrations as a function of CoQ10 concentration with standard error. Due to increase in interfacial tension with the increase in CoQ10 concentration, there were also increase in membrane tension of DPhPC/Squalene BLM.

Table 8: The effect of CoQ10 on membrane thickness, specific capacitance, Surface tension and membrane tension.

CoQ10 Conc. mg/ml	Contact angle (θ)	Surface tension (γ) mN/m	Specific Capacitance (Cs) mf/m	Membrane Tension (Γ) $\Gamma = 2\gamma \cos \theta$	Membrane Thickness (d) nm
0	23 ± 1	1.19 ± 0.08	3.7	2.19 ± 0.08	5
0.0005	25.9 ± 1	1.26 ± 0.04	3.9	2.27 ± 0.04	4.9
0.001	27.3 ± 1	2.47 ± 0.17	4.5	4.2 ± 0.17	4.15

From all these measurements, we have reached a conclusion that, CoQ10 is penetrating the BLM and affecting its membrane tension and consequently its membrane thickness. The result of increasing membrane tension is decreasing of membrane fluidity and this is highly considered in formulation of CoQ10 preparations in pharmaceutical industry.

Chapter 6: Modelling an Artificial Synaptic Communications in Microfluidic Platform³

In this chapter, a detailed demonstration and description for artificial synaptic modal in a microfluidic platform. Also, possible applications utilizing such platforms.

6.1. The Need for Artificial Synapse.

Synapses are the connection- and communication-gaps between organelles, cells, and neurons. For any functional disorder in this gap, there is a well-defined disease. For such a disease, there are many clinical trials and drug research attempts to treat such disorder. To be able to conduct successful treatment, scientists need a mimicking model on which they apply clinical trials. Our artificial synapse provides an *in-vitro* platform to study proteins and drugs interactions with such synaptic membranes before *in-vivo* trials on animals. For example, our red blood cell model mentioned in chapter 4, has provided a clear image for the interaction between apatite nanoparticles and RBCs in case of cryopreservation of RBCs [12]. For neurodegenerative disorders, our approach would give a platform to study synaptic-vesicles release disorders [155]. Furthermore, our modal is flexible and suitable for membrane composition changes to suit the specific conducted trials; this artificial synapse could be generalised to study immunological synapse for studying the exocytosis process where toxic materials are ejected towards the target cells.

6.2. The Experimental-Mimicking of Neuronal Synapse

When it comes to organ-on-chip or even smaller than an organ like a synapse-on-chip, the set-up becomes more difficult. The reason behind this is the sophistication and complexity of the biological system which achieve its structure-activity relationship (SAR). Building an *artificial synapse* is a kind of trending between organ-on-chip research efforts [155]. To build a synapse-on-chip that is different from the previously

³ Harvey Tawfik, Ralf Seemann, Jean-Baptiste Fleury (To be Submitted 2020)

successful efforts [156, 157], we present here our effort to build a model of artificial synapse with unsupported bilayer lipid membranes in a microfluidic chip.

6.2.1. The Concept of Artificial Synapse

In (fig. 75), a simple diagram for neuronal synapse showing our concept to how to simplify it and convert it into an artificial system inside a microfluidic chip.

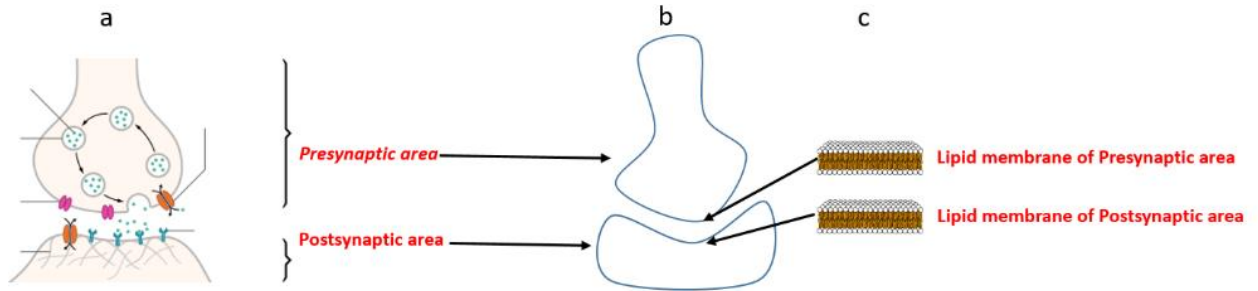


Figure 75: Concept of building artificial synapse into a microfluidic chip. a) A schematic diagram for neuronal synapse. b) An empty schematic diagram showing the pre- and postsynaptic membranes. c) A schematic diagram for the pre- and postsynaptic membranes.

The pre- and postsynaptic membranes can be modelled by two face-to-face free-standing bilayers. The microfluidic chip allows to control the buffer composition arounds these bilayers and to analyse the properties of this model synapse via electrophysiological and optical measurements.

6.3. Designs for Artificial Synapses.

By looking to a neuronal synapse (fig. 75a), we can divide the synaptic structure into three main zones: the presynaptic area, the synaptic gap, and the postsynaptic area. To create such system in a microfluidic platform, we have simplified this complex system into three main channels separated via two unsupported bilayer membranes. These two membranes representing the pre- and postsynaptic membranes. One of the most challenging points was how to keep on, at least, the flow of the buffer in the presynaptic area. In the previous trials (Chapter 4), it was difficult to change the presynaptic-finger content. To reach a higher level of stability for mechanical processes like buffer changing, ion channels insertions or liposomes fusions, we have developed

a new microfluidic protocol in the middle channel rather than previous techniques. In the middle channel there is a hanged droplet stabilized manually using volume-based pumps.

6.3.1. Three-Parallel Channels Artificial Neuronal Synapse-Like Model

This design is not new (fig. 76), but the addition of a new protocol, specifically, in the middle channel has changed the usage and capability of the chip to produce a functional artificial synapse.

This chip consists of four different inlets and three outlets. The middle channel has two different inlets: one for the lipid/oil mixture while the other for the buffer. Before we start the experiment, we fill the chip with lipid/oil mixture for about one hour. The experiment starts by pushing the buffer (one or different compositions) through inlets.

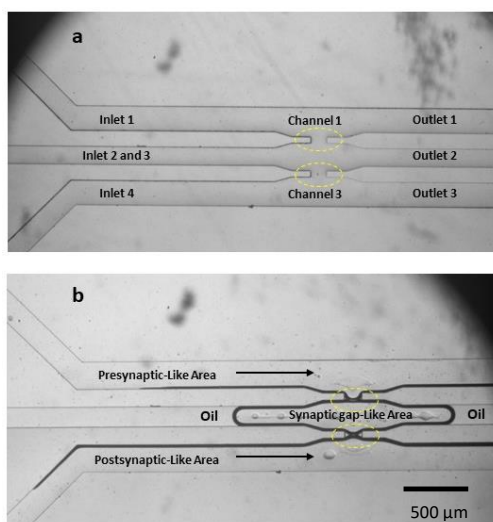


Figure 76: Design 1 for a neuronal synapse-like model. a) An empty chip showing different inlets and outlets. The yellow circles are highlighting the functional area; where the unsupported bilayer membranes are formed. b) A succesful attempt to build a synaptic structure showing the pre-/postsynaptic free-flow of buffers and a fixed middle droplet representing the synaptic gap.

From inlet 1 and 4 (fig. 76a), we start the flow of the buffer and meanwhile we push the oil finger. After reaching a stable flow, we create a buffer droplet in the middle channel and push it forward or backward by the oil-pump. For more control, we connected the outlets to three different volume-dependent pumps. This enabled us to

restrain the flow of all inlets. Once the middle droplet reaches the middle gaps area, it starts to form two opposing unsupported bilayer membranes representing the pre-/postsynaptic membranes. Once the two unsupported BLMs were formed, we can push new buffer, ion channels or liposomes through the presynaptic buffer that consequently will reach the presynaptic membrane to start an interaction with it.

The main drawback of this chip is the three outlets. It is not easy to move the seven volume-based reservoirs: inlets and outlets. This is coming from the free-flow postsynaptic buffer finger which requires an independent outlet. Such difficulty has raised the need to lower number of outlets, which was achieved in the next design.

6.3.2. Two-Parallel One-Perpendicular Artificial Neuronal Synapse-Like Model

As mentioned, in the previous technique, having three outlets is adding some difficulties in controlling the system despite being a successful and functioning system. To overpass such difficulty, we have designed a modified chip from model one to build an artificial neuronal synaptic model. In this design (fig. 77), the postsynaptic-like area has two features; the first one is being fixed i.e. no free-flow, and the second feature is being perpendicular on the middle drop.

The experiment starts as before by filling the chip with lipid/oil mixture. After one hour we push the buffer fingers slowly to the middle gap area (fig. 77b). Once the upper and lower fingers reached the middle gaps, we start generating and pushing the middle droplet until it reaches the middle gaps area to start interacting with the upper and lower monolayers of the upper and lower buffer fingers, respectively (fig. 77c). Once all monolayers touch each other, they start the zipping process and the formation of the bilayer membranes (fig. 77d). As before, the middle-gap droplet, representing the synaptic cleft, is being controlled from the two directions as shown in (fig. 77d). This technique is enabling us to keep the flow in the upper presynaptic-like area while having a better control rather than model one.

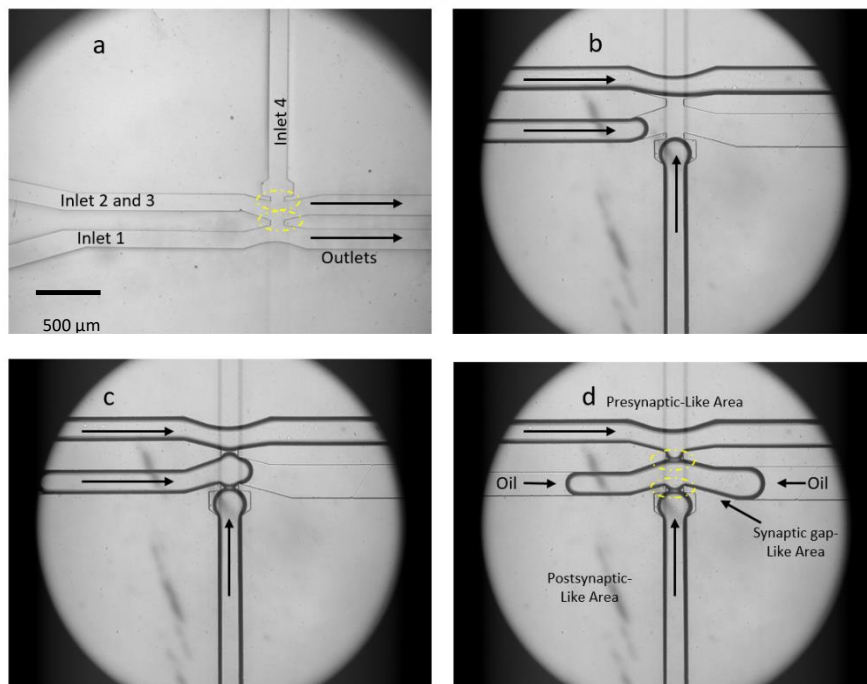


Figure 77: Design 2 for a neuronal synapse-like model. a) An empty chip showing different inlets and outlets. The yellow circles are highlighting the two opening where the two BLMs will be formed. b) the arrows are showing the directios of movements of each channel. The middle channel is composed of to intersecting inlets to generate the middle buffer droplet. c) the middle droplet has reached the middle area to start forming the 2 opposing membranes. d) After few seconds, the 2 BLMs have been formed while the flow in the upper channel (the presynaptic area) is contineous.

6.4. Step-by-Step Formation of Artificial Neuronal Synapses

In the next pages, we present a stepwise-manner progress for building an artificial functioning neuronal synapse in a microfluidic platform.

6.4.1. Formation of Two Stable unsupported BLMs

The first step was to ensure the formation of two opposing unsupported membranes that lasted for hours and were accepting shocks without rupturing of membranes. By using the second design (fig. 77), we were able to build the two opposing unsupported membranes. To proof the formation of very stable BLMs, we have dedicated electrical measurements using Heka patch master amplifier. The two BLMs are mimicking two capacitors connected in series and so we expected lower capacitance

record than in case of a single BLM. As shown in (fig. 78), after the formation of the two BLMs we recorded a jump in capacitance to 50 pF indicating the formation of two BLMs. In (fig. 79), a quick demonstration to the effect of a single break in one of the two BLMs. After losing one BLM, we have reached a situation of a single capacitor and this could be seen in the jump of the capacitance from 40 pF to about 80 pF.

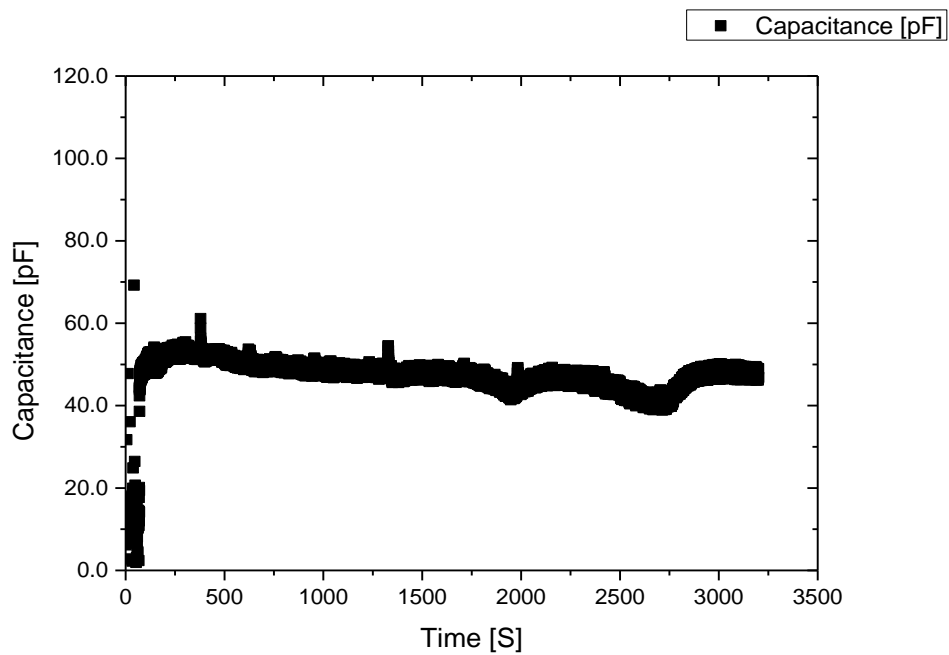


Figure 78: Capacitance measurements for 2 unsupported bilayer membranes opposing to each other. These minor fluctuations resulted from movements in BLMs positions slightly over time. The average of 50 pF is a proof for the formation of the needed system and stability for long time.

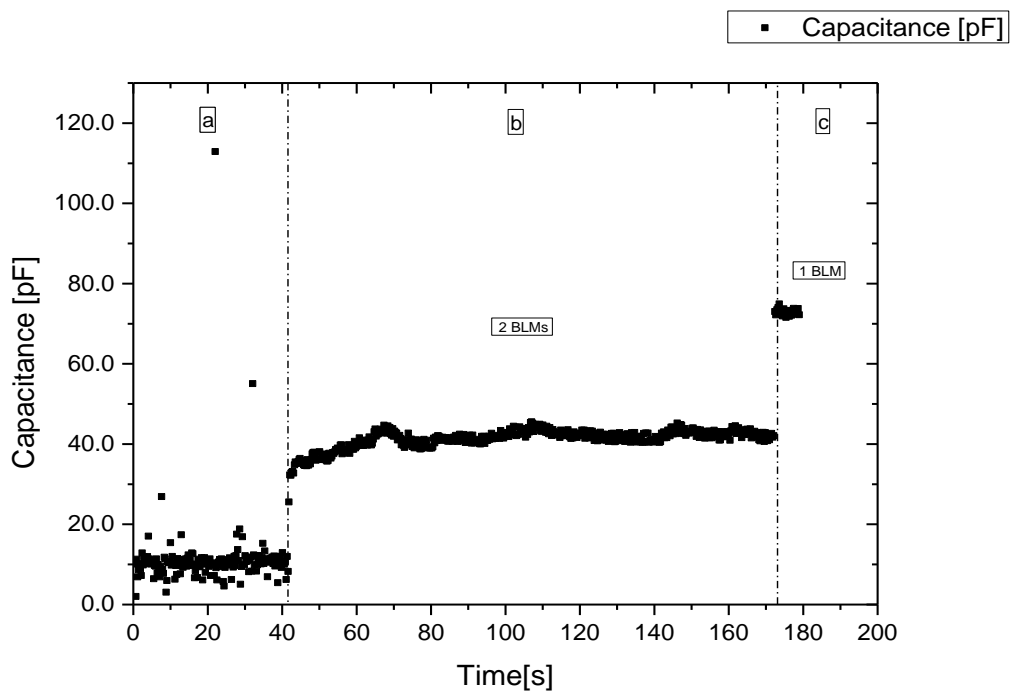


Figure 79: Capacitance measurements for 2 unsupported bilayer membranes. This graph is showing the case of rupturing of one of the two BLMs. a) one membrane is formed but the other membrane is not yet. b) After the zipping of the second membrane, the capacitance has recorded about 40 pF for few minutes. c) After rupturing of one of the two membranes, the capacitance jumped to almost 80 pF.

6.4.2. Insertion of Gramicidin A Protein as a Membrane Receptor-like

After formation of very stable two opposing unsupported BLMs, we have tried to insert some membrane receptors to ensure the functionality of the synapse. For our current model, we have used *Gramicidin A* (gA) as membrane receptors. From the detailed description of gA and how it works; in chapter 2, we had to insert them into two channels, so they form functional ion channels in the BLM which was separating these two channels (Figure 80).

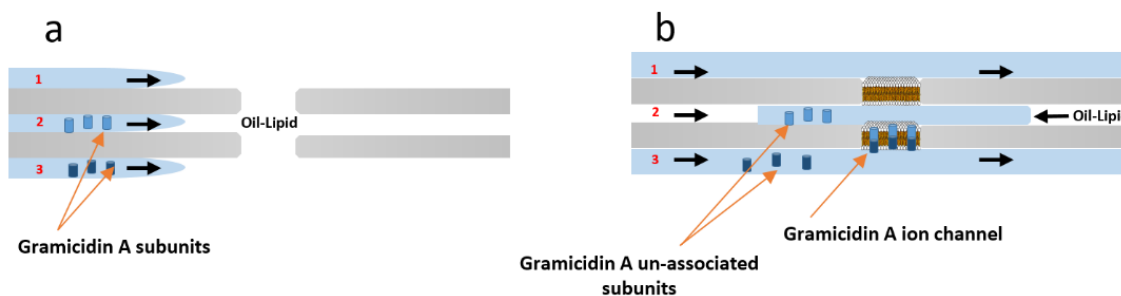


Figure 80: Assembly of Gramicidin A subunits into a BLM. A) In the beginning of the experiment, the two subunits of gramicidin A are distributed in the buffer of channels 2 and 3. Channel 3 is playing the role of postsynaptic area. B) After continuous flow in the chip, 2 BLMs were formed while the gramicidin A channels are formed only in the lower BLM, because there is no any subunits from the protein in channel 1.

This process starts by loading gA into two channels, one of them is the middle channel (fig. 80a). The molar concentrations of gA was about 10^{-9} molar. After formation of the two BLMs (fig. 80b), the two subunits forming the gA ion channel, starts to associate together to form an ion channel. These ion channels are in dynamic equilibrium; they associate/dissociate in seconds. After formation of ion channels in one BLM, we have reached an electric-circuit model in which a capacitor (the upper BLM) and a resistor (the lower membrane) are connected in series. Application of voltage (around 50 mV) and measuring the capacitance (fig. 81) of the BLMs have showed the formation of a single capacitor with around 100 pF (one membrane) while optically we could see two formed membranes. This is a solid proof of insertion of gA in the lower membrane (fig. 80b) which is representing the postsynaptic membrane. This technique is very ideal for insertion of gA despite being difficult; this is because the possibility of movement of some gA molecules to the upper channel in case a rupture happened for the upper BLM. This may cause uninstallation of all connections to clean the upper channel; because keeping the flow on to remove all molecules was not successful every time.

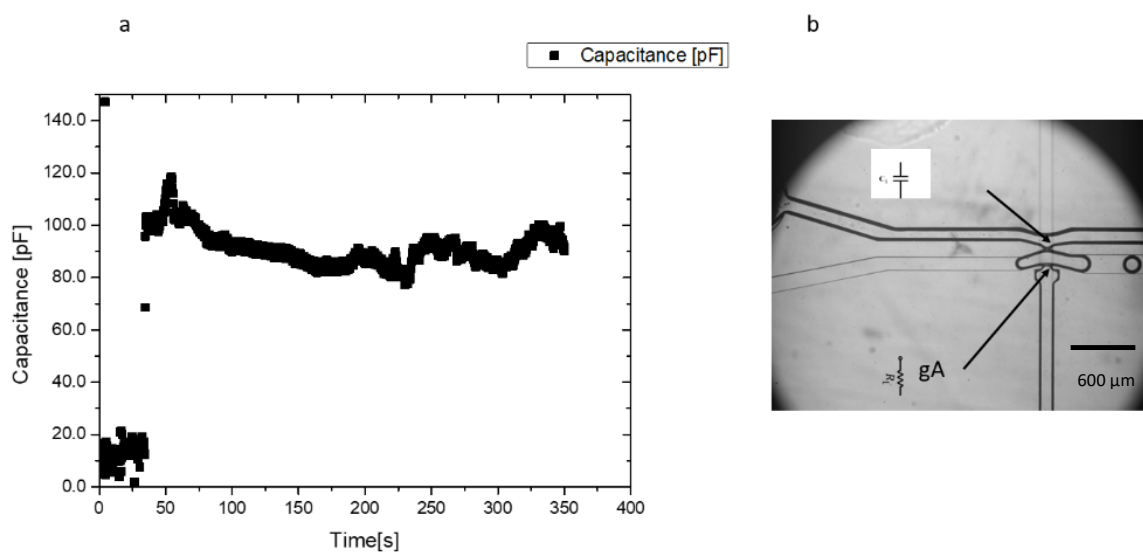


Figure 82: Capacitance measurements for two membranes in presence of gA. A) The capacitance measurement recording around 100 pF while optically there were two BLMs formed. B) A microscopic image with illustration of the position of the gA and the equivalent electrical component. The upper membrane is representing the presynaptic membrane and the lower membrane is representing the postsynaptic membrane.

We have also inserted gA using a different technique. This is a simple technique to start the experiment. As shown in (fig. 81), we suspend gA molecules in all channels and this has led to formation of gA ion channels in both BLMs resulting in drop in capacitance after the formation of the two BLMs. Due to formation of gA channels in both BLMs, we have recorded a drop in capacitance from around 50 pF to almost 0 F. The capacitance of 50 pF is indicating the formation of 2 capacitors and as a result, the capacitance did not reach 100 pF like the case in figure 81. One more feature was recorded which is the velocity of capacitance drop. As shown in (fig. 82a), it took a little bit above one minute to reach the lowest capacitance. Also, we have noticed that sometimes the jump in capacitance; indicating formation of the two BLMs, would take more time than expected (fig. 83).

This could be simply explained due to delay in zipping in one of the two BLMs or even in both.

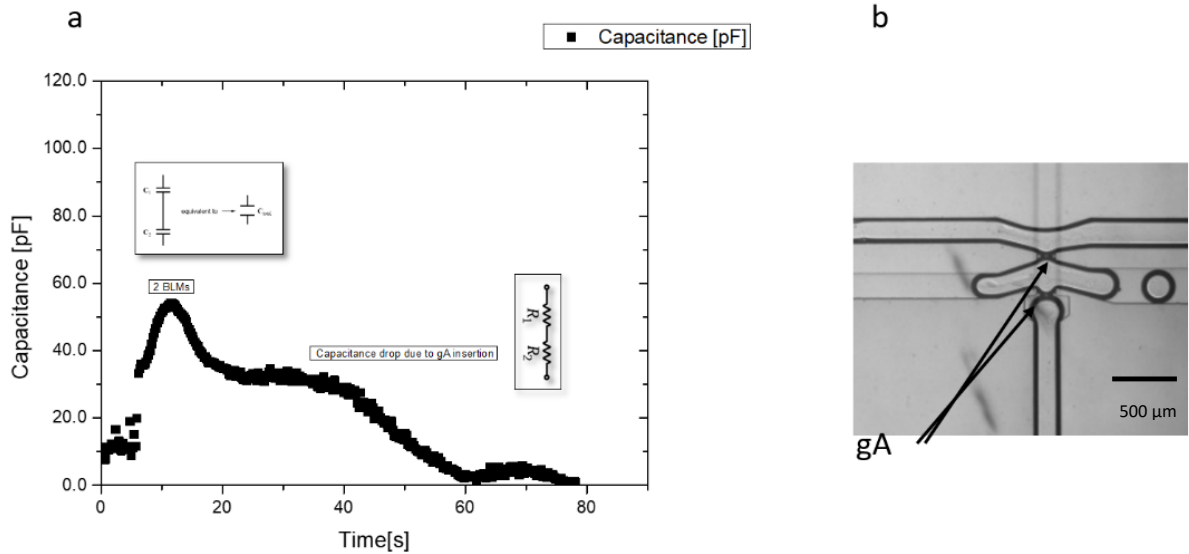


Figure 83: Capacitance measurements of 2 BLMs with gA in all channels. A) Capacitances jump after 10 seconds then drop from 50 pF to almost 0 F after formation of the 2 BLMs and assembly of the ion channels, respectively. B) A microscopic image for stable 2 BLMs with illustration to the position of gA in both channels.

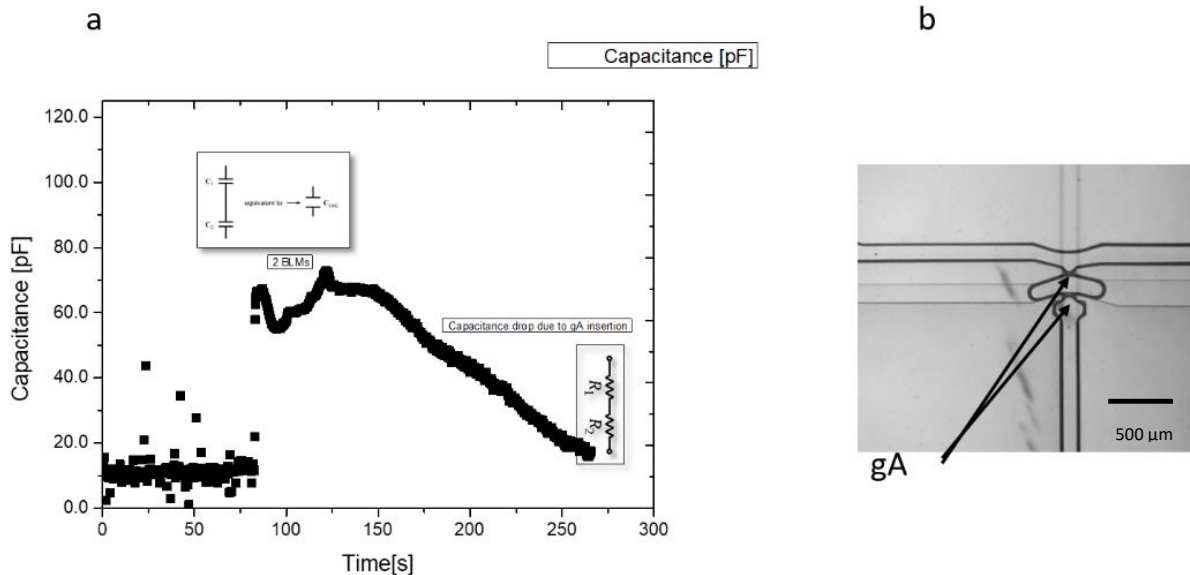


Figure 84: Capacitance measurements of 2 BLMs with gA in all channels. A) Capacitance jump delayed about 75 seconds until the jump to about 60 pF indicating the formation of the 2 BLMs. B) A microscopic image for stable 2 BLMs with illustration to the position of gA in both channels.

6.4.3. Blocking of Gramicidin A Ion Channels in the Presynaptic Area

We have used the second technique for insertion of gA into the preferred postsynaptic area. As mentioned in the previous step, we inserted gA ion channels in all 3 buffer fingers which has resulted in drop of capacitance due to diminishing of the 2 capacitors properties by the ion channels (fig. 84).

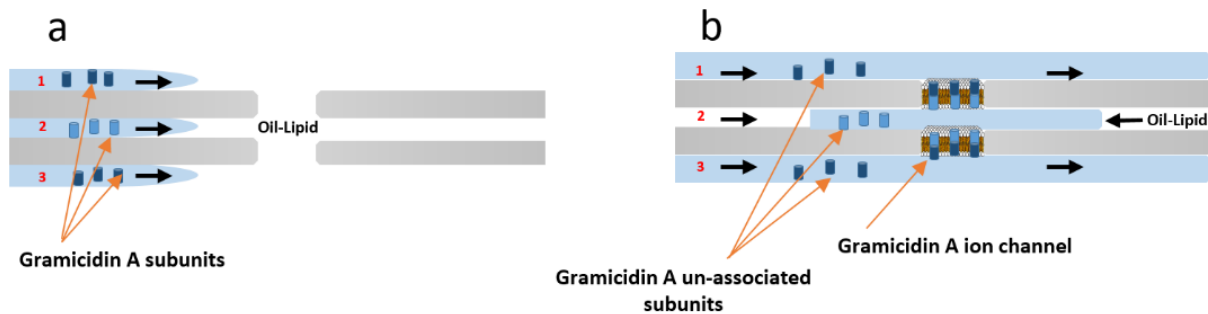


Figure 85: Assembly of Gramicidin A subunits into the 2 BLMs. A) In the beginning of the experiment, the two subunits of gramicidin A are distributed in the buffer of the 3 channels. Channel 3 is playing the role of postsynaptic area while channel 1 is representing the presynaptic area. B) After continuous flow in the chip, 2 BLMs were formed and gramicidin A ion channels are being formed in both BLMs.

To re-build the presynaptic area, calcium ions with molar concentration of 20 mM were added to the continuous-flowing presynaptic area. Calcium ions (not only but also all divalent ions) are blocking functional gA channels. (fig. 85).

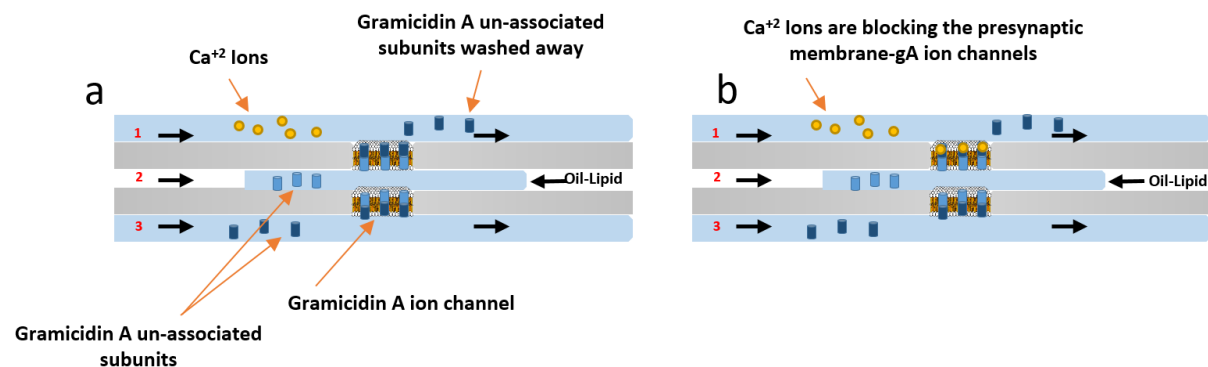


Figure 86: Assembly of Gramicidin A subunits into the 2 BLMs in presence of Ca^{+2} ions. A) gA ion channels are being inserted into both BLMs. B) Ca^{+2} ions started to reach the presynaptic-membrane area and block any gA channels.

To proof the previous theory, we have conducted capacitance measurements to check the possibility of changing membranes compositions. Figure 86, showing three crucial steps towards a successful functional synapse.

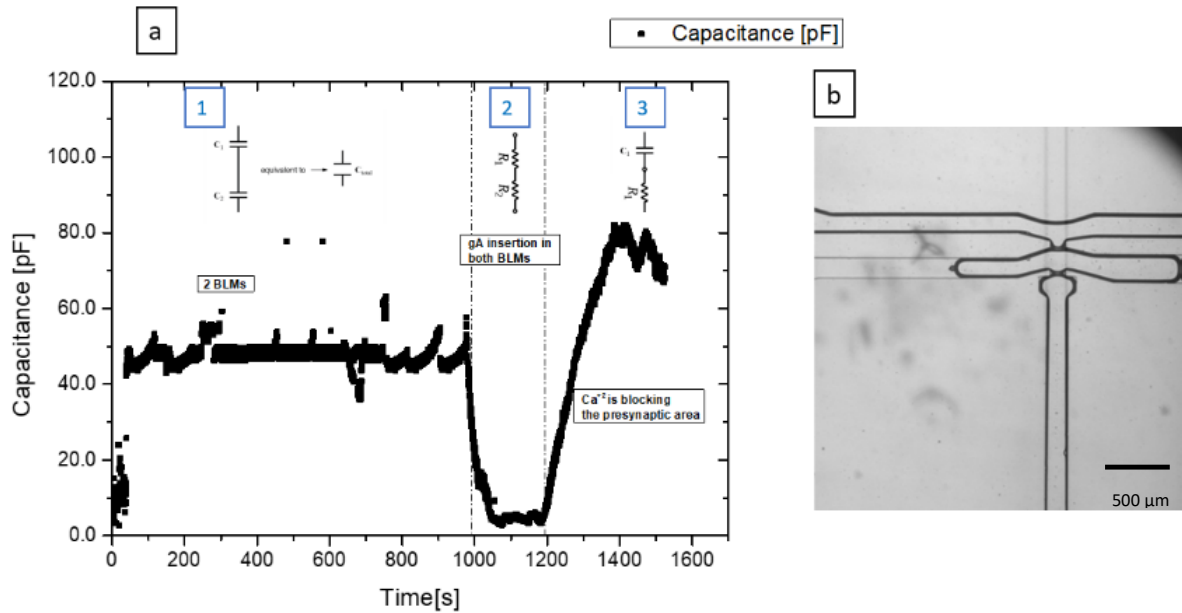


Figure 87: Capacitance measurements for insertion of gA and the effect of Ca^{+2} . A) Capacitance measurements is showing three crucial steps: 1. Formation of the 2 BLMs representing the pre- and postsynaptic membranes. 2. Insertion of gA in both and the drop in capacitance. 3. The flow of Ca^{+2} in the presynaptic area and the blockade of gA ion channels which is shown as increase in capacitance above that measured in the first step. B) A microscopic image for stable 2 BLMs.

The experiments started by perfusion of the chip with lipid/oil mixture for one hour. Later, we started pushing the buffer slowly into the chip as described before. All the three droplets contained gA subunits. After zipping and membranes formation (fig. 85a, 1), we have recorded a capacitance of about 50 pF indicating the formation of two BLMs just after about 20 seconds. After more than 900 seconds, gA subunits started to diffuse in the lipid monolayers, assembled and forming functional gA ion channels indicated by the drop in capacitance to about 10 pF (fig. 85a, 2). Such delay in capacitance drop could be correlated to certain reasons such as movement of the middle drop, despite slight moving, and this would affect the assembly of gA channels. One more hypothesis, is the concentration of gA in the middle channel; such concentration could be very low and thus required longer time to diffuse in both middle droplet-leaflets and subsequently resulted into a delay. After such drop, we have inserted some Calcium ions in the presynaptic freely flowing area, and once these ions reached the membrane,

they started to block all gA ion channels gradually. This was recorded as increase in the capacitance to reach 80 pF (fig. 85a, 3). To summarize this step, we created two opposing BLMs, both contain gA ion channels and finally we blocked only the presynaptic membrane by calcium ions (Synaptic-Vesicles like) while the postsynaptic membrane was still opened by functional gA channels; this is considered as postsynaptic membrane-receptors.

Summary

In this work, we presented new microfluidics methods to build unsupported artificial bilayer lipid membranes. Our complete new three-channel microfluidic scheme is able to produce two unsupported membranes with keeping the flow on one or both sides of the middle channel. This approach is enabling us to change the buffer solution completely in the upper and lower channels. All results were observed and explored by optical and electrophysiological means.

In chapter 3, we have presented all microfluidics schemes were used to build a single or double unsupported/free-standing BLM. We described different geometries for each target. Each BLM formation was confirmed optically and electrophysiological. A new and fast approach to build a BLM in a tube has been described with electrical proof, capacitance measurement, for the formation of the BLM. We have modified these geometries to build free-standing two BLMs in front of each other.

In chapter 4, we have studied the interaction of apatite nanoparticles with our artificial free-standing lipid membrane. This study has given a clear image for the behaviour of these nanoparticles when they come in contact with red blood cells and how they transfer their load; Trehalose, inside the RBCs to start the cryopreservation process. We have labelled Eu-NPs to study their translocation through the BLM, and results have showed no translocation. Also, we have used FITC as a substituent for Trehalose. We found that, FITC is diffusing to the adherent cell thanks to apatite NPs. After conducting capacitance measurements, we were able to calculate the gain in free energy to study the interaction of these NPs with the model membrane system according to the pH of the medium. We found out that in acidic medium (pH 6.5), apatite NPs have showed more interaction with lipid molecules than in a pH 7.

In chapter 5, we studied the effect of silicone oil on free-standing lipid membrane tension. It is confirmed that phospholipids are not soluble in silicone oils, but phospholipids membranes have lower membrane tension when few percentages of silicone oil were introduced to the system. Due to insolubility, Si AR20 was found to form oil inclusions within the lipid bilayer membrane. These oil inclusions have led to formation of micro- or nano-lipid domains. Such inclusions in membranes showed a notable dynamic heterogeneity. To study this phenomenon, we conducted interfacial tension, contact angle and membrane tension measurements in addition to the gain in free energy which was calculated before and after

formation of the BLM in presence and absence of silicone oil. We found that silicone oil is decreasing interfacial tension, membrane tension and consequently the gain in free energy. We also studied the effect of silicone oil on gramicidin A ion channel function. We tested the transfer of five different ions through gA channels in presence of different concentrations of silicone oil. The behaviour of gA ion channels in presence of silicone oil (5 and 10%) was unexpected and could not be predicted. We found that some ions like Na, K and Rb have higher conductance with increasing silicone oil percentages. We studied also the effect of the lipophilic coenzyme Q10 on membrane tension. We conducted capacitance and interfacial tension measurements for this purpose. We have reached a conclusion that, the insertion of CoQ10 in BLM has resulted in increasing membrane tension and decreasing the membrane thickness.

In chapter 6, for the first time, we present a model for artificial neuronal synapses. We improved the design of the three-channel cross geometry to produce very stable two free-standing BLMs. The main change is in the middle channel; we created a suspended drop to serve as a synaptic cleft. We produced this artificial synapse in a stepwise manner. Firstly, we produced two stable unsupported membranes in front of each other. Secondly, the gramicidin A started to assemble and form ion channels in both or in the presynaptic area according to the purpose of the experiment. Later, we perfused some calcium ions in the presynaptic region to block the gramicidin A ion channels in the presynaptic membrane.

Appendix

Low Noise on Capacitance Measurements (*On-Cell mode, Using Probe EPC 10*)

We present in the next few pages, as described in the manual of the ‘*Patchmaster*’, how to achieve capacitance measurements with the lowest noise possible. For capacitance measurements we used *Patchmaster* software and *EPC10*.

a. Hardware Setup

For higher resolution measurements, we made sure to have a PC with higher RAM (8 GB RAM) to record full sweeps in higher resolution; low noise. Before, starting new sets of experiments, we perform calibration by using the ‘*cell-model*’. Using the option ‘*Test and Calibrate*’ in the *EPC10-USB* menu in the *Patchmaster* software.

b. Software Setup

According to Heka manual, we must download the *Patchmaster* software (Version: 2x73.5) according to our operating system; Windows 10 in our case, through the following website:

https://www.heka.com/downloads/downloads_main.html

After that, we must unzip the downloaded file and follow the subsequent instructions.

For capacitance measurements, we used a default file ‘*Oncell-Cm.set*’ by copying this file into the *Patchmaster* folder. We open the *Patchmaster* application and then drag the ‘*Oncell-Cm.set*’ on it.

Also, this could be done manually following the procedures of the online manual (Section *Software Installation 3.6*):

https://www.heka.com/downloads/hardware/manual/m_epc10.pdf

For maximum points, sweeps, recordings, we increased the ‘*Max. Sample Points*’ from the ‘*Configuration*’ Window in the software. This will require more storage space on RAMs.

On our *Oncell-Cm* file; we used the following convention in the following order:

- AD-Channel 1: Output of the active amplifier with two filters 1 & 2 (Note that filter 1 prior to 2)
- AD-Channel 2: Capacitance trace; Called ‘*LockIn_CM*’
- AD-Channel 3: Conductance trace; Called ‘*LockIn_GM*’

c. Procedures for LockIn Calibration:

Calibrations should be done before patching otherwise it is not obligatory. If you need to calibrate during recording, you must make sure that your membrane; the seal, is very stable. After warming up the device for at least 30 min, we connect the probe to the model cell, and then apply the function: '*Test and Calibrate*' in the EPC_10 menu and follow all instructions. This will take about 10 minutes and should be done every 6 months at most.

Bibliography

- [1] GM. Cooper. *The Cell: A Molecular Approach*. 2nd edition. Sunderland (MA): Sinauer Associates; 2000, ISBN-10: 0-87893-106-6.
- [2] D. Balleza, “Toward Understanding Protocell Mechanosensation,” *Orig. Life Evol. Biosph.*, vol. 41, pp. 281–304, 2011.
- [3] D. E. Hughes, “The bacterial cytoplasmic membrane,” *J. Gen. Microbiol.*, vol. 29, pp. 39–46, 1962.
- [4] K. Mesa, “Essential Cell Biology.” *The Yale Journal of Biology and Medicine* vol. 88, pp. 100–101, 2015.
- [5] J. B. Dacks and M. C. Field, “Evolution of the eukaryotic membrane-trafficking system: origin, tempo and mode,” *J. Cell Sci.*, vol. 120, pp. 2977–2985, 2007.
- [6] J. S. Bonifacino and B. S. Glick, “The mechanism of vesicle budding and fusion,” vol. 116, no. 1980, pp. 153–166, 2004.
- [7] M. Faini, R. Beck, F. T. Wieland, and J. A. G. Briggs, “Vesicle coats: Structure, function, and general principles of assembly,” *Trends Cell Biol.*, vol. 23, pp. 279–288, 2013.
- [8] D. Hoffmann, T. Grunwald, S. Kuate, and O. Wildner, “Mechanistic analysis and comparison of viral fusogenic membrane proteins for their synergistic effects on chemotherapy,” *Cancer Biol. Ther.*, vol. 6, pp. 510–518, 2007.
- [9] R. Jahn, T. Lang, and T. C. Sü Dhof, “Review Membrane Fusion dynamic supramolecular assemblies involving con,” *Cell*, vol. 112: 519–533, 2003.
- [10] R. Jahn, R. Scheller, “SNAREs — Engines for Membrane Fusion”. *Nat. Rev. Mol. Cell Biol.* Vol. 7, pp. 631–643, 2006.
- [11] H. Bayley, B. Cronin, A. Heron, M. a. Holden, W. L. Hwang, R. Syeda, J. Thompson, and M. Wallace, “Droplet interface bilayers” *Mol. Biosyst.*, vol. 4, pp. 1191–1208, 2008.

- [12] M. Stefanic, K. Ward, H. Tawfik, R. Seemann, V. Baulin, Y. Guo, J. B. Fleury, and C. Drouet, "Apatite nanoparticles strongly improve red blood cell cryopreservation by mediating trehalose delivery via enhanced membrane permeation," *Biomaterials*, vol. 140, pp. 138–149, 2017.
- [13] C. Drouet, "Biomimetic Apatite-Based Functional Nanoparticles as Promising Newcomers in Nanomedicine: Overview of 10 Years of Initiatory Research," *Intern. Med. Prim. Healthc.*, vol. 1, pp. 1–9, 2017.
- [14] V. Sokolova and M. Epple, "Inorganic nanoparticles as carriers of nucleic acids into cells," *Angew. Chemie - Int. Ed.*, vol. 47, pp. 1382–1395, 2008.
- [15] O. S. Andersen, "Ion movement through gramicidin A channels. Single-channel measurements at very high potentials," *Biophys. J.*, vol. 41, pp. 119–133, 1983.
- [16] C. Eric and G. Ball, "The Composition of the Mitochondrial Membrane in Relation to Its Structure and Function," *Int. Rev. Cytol.*, vol. 13, pp. 99–133, 1962.
- [17] M. J. Acosta, L. Vazquez Fonseca, M. A. Desbats, C. Cerqua, R. Zordan, E. Trevisson, and L. Salviati, "Coenzyme Q biosynthesis in health and disease," *Biochim. Biophys. Acta - Bioenerg.*, vol. 1857, pp. 1079–1085, 2016.
- [18] B. Chance, P. Mueller, D. De Vault, and L. Powers, "Biological membranes," *Phys. Today*, vol. 33, pp. 32–38, 1980.
- [19] J. D. Nickels, J. C. Smith, and X. Cheng, "Lateral organization, bilayer asymmetry, and inter-leaflet coupling of biological membranes," *Chem. Phys. Lipids*, vol. 192, pp. 87–99, 2015.
- [20] R. Harrison, G.G. Lunt, "Structural Organization. In: *Biological Membranes. Tertiary Level Biology*," Springer, Dordrecht. pp 102-129, 1980.
- [21] I. D. Pogozheva, H. I. Mosberg, and A. L. Lomize, "Life at the border: Adaptation of proteins to anisotropic membrane environment," *Protein Sci.*, vol. 23:1165–1196, 2014.
- [22] M. A. Lemmon and J. Schlessinger, "(All Structures) NIH Public Access," vol. 141: 1117–1134, 2011.

- [23] I. D. Pogozeva, S. Tristram-Nagle, H. I. Mosberg, and A. L. Lomize, “Structural adaptations of proteins to different biological membranes,” *Biochim. Biophys. Acta - Biomembr.*, vol. 1828, pp. 2592–2608, 2013.
- [24] G. Van Meer, D. R. Voelker, and G. W. Feigenson, “Membrane lipids: where they are,” *Nat. Rev. Mol. Cell Biol.*, vol. 101, pp. 1–4, 2009.
- [25] A. Honigmann and A. Pralle, “Compartmentalization of the Cell Membrane,” *J. Mol. Biol.*, vol. 428, pp. 4739–4748, 2016.
- [26] A. Engel and H. E. Gaub, “Structure and Mechanics of Membrane Proteins,” *Annu. Rev. Biochem.*, vol. 77, pp. 127–148, 2008.
- [27] C. Théry, M. Ostrowski, and E. Segura, “Membrane vesicles as conveyors of immune responses,” *Nat. Rev. Immunol.*, vol. 9, pp. 581–593, 2009.
- [28] AA. Tokarev, A. Alfonso, N. Segev “Overview of Intracellular Compartments and Trafficking Pathways,” In: *Trafficking Inside Cells. Molecular Biology Intelligence Unit. Springer*, pp. 3-14. 2009
- [29] E. Sackmann, “Chapter 1: Biological Membranes Architecture and Function,” *Handb. Biol. Phys.*, vol. 1, pp. 1–63, 1995.
- [30] A. H. de Vries, F. J. van Eerden, C. Arnarez, H. I. Ingólfsson, M. N. Melo, C. A. Lopez, S. J. Marrink, T. A. Wassenaar, X. Periole, and D. P. Tieleman, “Lipid Organization of the Plasma Membrane,” *J. Am. Chem. Soc.*, vol. 136, pp.14554–14559, 2014.
- [31] H. Lodish, A. Berk, SL. Zipursky, et al. “*Molecular Cell Biology*,” 4th edition. New York, ISBN-10: 0-7167-3136-3. 2002.
- [32] R. Haas, B. C. Jackson, B. Reinhold, J. D. Foster, and T. L. Rosenberry , “Glycoinositol phospholipid anchor and protein C-terminus of bovine erythrocyte acetylcholinesterase: analysis by mass spectrometry and by protein and DNA sequencing,” *Biochem. J.*, vol. 314, pp. 817–825, 2015.
- [33] M. Murate and T. Kobayashi, “Revisiting transbilayer distribution of lipids in the plasma membrane,” *Chem. Phys. Lipids*, vol. 194, pp. 58–71, 2016.

- [34] T. Harayama and H. Riezman, "Understanding the diversity of membrane lipid composition," *Nat. Rev. Mol. Cell Biol.*, vol. 19, pp. 281–296, 2018.
- [35] G. de Wit, J. S. H. Danial, P. Kukura, and M. I. Wallace, "Dynamic label-free imaging of lipid nanodomains," *Proc. Natl. Acad. Sci.*, vol. 112, pp. 12299–12303, 2015.
- [36] B. Alberts, A. Johnson, J. Lewis, et al. "Molecular Biology of the Cell," 4th edition. New York: Garland Science, 2002
- [37] G. Nordlund, P. Brzezinski, and C. Von Ballmoos, "SNARE-fusion mediated insertion of membrane proteins into native and artificial membranes," *Nat. Commun.*, vol. 5, pp. 1–8, 2014.
- [38] B. Alberts, A. Johnson, J. Lewis, et al. "Molecular Biology of the Cell," 4th edition. New York: Garland Science, 2002
- [39] D. Chandler, "Interfaces and the driving force of hydrophobic assembly.," *Nature*, vol. 437, pp. 640–647, 2005.
- [40] I. M. Hafez and P. R. Cullis, "Roles of lipid polymorphism in intracellular delivery," *Adv. Drug Deliv. Rev.*, vol. 47, pp. 139–148, 2001.
- [41] X. J. Li and M. Schick, "Theory of lipid polymorphism: Application to phosphatidylethanolamine and phosphatidylserine," *Biophys. J.*, vol. 78, pp. 34–46, 2000.
- [42] J. Bigay and B. Antonny, "Curvature, Lipid Packing, and Electrostatics of Membrane Organelles: Defining Cellular Territories in Determining Specificity," *Dev. Cell*, vol. 23, pp. 886–895, 2012.
- [43] J. M. Seddon and R. H. Templer, "Handbook of biological physics - Polymorphism of Lipid-Water Systems," vol. 1, pp. 97–160, 1995.
- [44] S. Kakorin, U. Brinkmann, and E. Neumann, "Cholesterol reduces membrane electroporation and electric deformation of small bilayer vesicles," *Biophys. Chem.*, vol. 117, pp. 155–171, 2005.
- [45] M. K. Hans-Jürgen Butt, G. Karlheinz, *Physics and Chemistry of Interfaces*. 2006.
- [46] L. Dominguez, Ana; Fernandez, Aurora; Gonzalez, Noemi; Iglesias, Emilia; Montenegro, "Dominguez-JCE-1997," *J. Chem. Educ.*, vol. 74, pp. 1227–1231, 1997.

- [47] P. D. M. Shinitzky, *Biomembranes: Structural and Functional Aspects*. 2008.
- [48] I. van Uitert, S. Le Gac, and A. van den Berg, “The influence of different membrane components on the electrical stability of bilayer lipid membranes,” *Biochim. Biophys. Acta - Biomembr.*, vol. 1798, pp. 21–31, 2010.
- [49] J. C. Weaver and Y. A. Chizmadzhev, “Review Theory of Electroporation 1996.,” vol. 41, pp. 135–160, 1996.
- [50] L. V. Chernomordik, S. I. Sukharev, S. V. Popov, V. F. Pastushenko, A. V. Sokirko, I. G. Abidor, and Y. A. Chizmadzhev, “The electrical breakdown of cell and lipid membranes: the similarity of phenomenologies,” *BBA - Biomembr.*, vol. 902, pp. 360–373, 1987.
- [51] T. Batista Napotnik and D. Miklavčič, “In vitro electroporation detection methods – An overview,” *Bioelectrochemistry*, vol. 120, pp. 66–182, 2018.
- [52] P. Mojca, K. Tadej, M. Damijan, K. Peter and M. Alenka “Chapter Seven Electroporation of Planar Lipid Bilayers and Membranes,” in *Advances in Planar Lipid Bilayers and Liposomes*, vol. 6, pp. 165–226, 2008.
- [53] M. Pinot, S. Vanni, E. Ambroggio, D. Guet, B. Goud, J.-B. Manneville “Feedback between membrane tension, lipid shape and curvature in the formation of packing defects,” 2018.
- [54] TH. Wideman, GG. Asmundson, RJ. Smeets, AJ. Zautra, MJ. Simmonds, MJ. Sullivan, JA. Haythornthwaite, RR. Edwards. Rethinking the fear avoidance model: toward a multidimensional framework of pain-related disability. Vol. 154, pp. 2262–2265, 2013.
- [55] B. Antonny, L. Vamparys, S. Vanni, R. Gautier, P. F. J. Fuchs, C. Etchebest, and G. Drin, “Amphipathic Lipid Packing Sensor Motifs: Probing Bilayer Defects with Hydrophobic Residues,” *Biophys. J.*, vol. 104, pp: 575–584, 2013.
- [56] A. D. Petelska and Z. A. Figaszewski, “Interfacial tension of bilayer lipid membrane formed from phosphatidylethanolamine,” *Biochim. Biophys. Acta - Biomembr.*, vol. 1567, pp. 79–86, 2002.
- [57] A. D. Petelska, “Interfacial tension of bilayer lipid membranes,” *Cent. Eur. J. Chem.*, vol. 10, pp. 16–26, 2012.

- [58] S. Martens and H. T. McMahon, “Mechanisms of membrane fusion: Disparate players and common principles,” *Nat. Rev. Mol. Cell Biol.*, vol. 9, pp. 543–556, 2008.
- [59] A. Manuscript, “Viral and Developmental Cell Fusion Mechanisms: Conservation and Divergence,” vol. 14, pp. 11–21, 2013.
- [60] G. B. Melikyan, “Driving a wedge between viral lipids blocks infection,” *Proc. Natl. Acad. Sci.*, vol. 107, 2010.
- [61] L. V Chernomordik, M. M. Kozlov, and M. Biophysics, “Mechanics of membrane fusion,” vol. 15, pp. 675–683, 2009.
- [62] L. V Chernomordik and M. M. Kozlov, “Protein-Lipid Interplay in Fusion and Fission of Biological Membranes,” pp. 175–207, 2003.
- [63] R. Lipowsky, “The conformation of membranes,” vol. 349, 1991.
- [64] A. Portis, C. Newton, and W. Pangborn, “Studies on the Mechanism of Membrane Fusion: Evidence for an Intermembrane Ca^{2+} -Phospholipid Complex, Synergism with Mg^{2+} , and Inhibition by Spectrin,” *Biochemistry*, vol. 18, pp. 780–790, 1979.
- [65] S. Mondal Roy and M. Sarkar, “Membrane Fusion Induced by Small Molecules and Ions,” *J. Lipids*, vol. 2011, pp. 1–14, 2011.
- [66] A. P. Hornby and P. R. Cullis, “Influence of local and neutral anaesthetics on the polymorphic phase preferences of egg yolk phosphatidylethanolamine,” *BBA - Biomembr.*, vol. 647, pp. 285–292, 1981.
- [67] Y. A. Chen, R. H. Scheller, and H. H. Medical, “Snare-Mediated Membrane Fusion,” vol. 2, pp. 98–106, 2001.
- [68] H. Lodish, A. Berk, S. L. Zipursky, et al. *Molecular Cell Biology*, 4th editio. New York, 2000.
- [69] J. E. Rothman, R. H. Scheller, T. Söllner, S. W. Whiteheart, and M. K. Bennett, “A protein assembly-disassembly pathway in vitro that may correspond to sequential steps of synaptic vesicle docking, activation, and fusion,” *Cell*, vol. 75, pp. 409–418, 1993.
- [70] H. J. Risselada and H. Grubmüller, “How SNARE molecules mediate membrane fusion: Recent insights from molecular simulations,” *Curr. Opin. Struct. Biol.*, vol. 22, pp. 187–196, 2012.

- [71] N. Vardjan, J. Jorgačevski, and R. Zorec, “Fusion pores, SNAREs, and exocytosis,” *Neuroscientist*, vol. 19, pp. 160–174, 2013.
- [72] T. C. Südhof and J. E. Rothman, “Membrane Proteins: Grappling with SNAREs and SM proteins,” vol. 323, pp. 474–477, 2009.
- [73] C. Guyton and John E. Hall “Textbook of Medical Physiology 11th Edition. Unit IX: The Nervous System: A. General Principles and Sensory Physiology; Copyright Elsevier (2006).”
- [74] G. Perea, M. Navarrete, and A. Araque, “Tripartite synapses: astrocytes process and control synaptic information,” *Trends Neurosci.*, vol. 32, pp. 421–431, 2009.
- [75] W. Wefelmeyer, D. Cattaert, and J. Burrone, “Activity-dependent mismatch between axo-axonic synapses and the axon initial segment controls neuronal output,” *Proc. Natl. Acad. Sci.*, vol. 112, pp. 9757–9762, 2015.
- [76] Y. Kubota, F. Karube, M. Nomura, and Y. Kawaguchi, “The Diversity of Cortical Inhibitory Synapses,” *Front. Neural Circuits*, vol. 10, pp. 1–15, 2016.
- [77] A. E. Pereda, “Electrical synapses and their functional interactions with chemical synapses,” vol. 15, pp. 250–263, 2015.
- [78] T. Biederer, M. Missler, and T. C. Südhof, “Synaptic Cell Adhesion,” *Cold Spring Harb. Perspect. Biol.*, vol. 4, pp. a005694–a005694, 2012.
- [79] R. Llinás, I. Z. Steinberg, and K. Walton, “Relationship between presynaptic calcium current and postsynaptic potential in squid giant synapse,” *Biophys. J.*, vol. 33, pp. 323–351, 1981.
- [80] L. Qu, Y. Akbergenova, Y. Hu, and T. Schikorski, “Synapse-to-synapse variation in mean synaptic vesicle size and its relationship with synaptic morphology and function,” *J. Comp. Neurol.*, vol. 514, pp. 343–352, 2009.
- [81] B. Williamson, Robin J. Heyden, *Biology: Exploring Life*. 2006.
- [82] P. Avasthi and W. F. Marshall, “Discharge of the Readily Releasable Pool With Action Potentials at Hippocampal Synapses,” *Int. Soc. Differ.*, vol. 83, pp. 1–29, 2012.
- [83] S. Robert, *Biology and Human Behavior: The Neurological Origins of Individuality*, 2005.

- [84] D. Lavery, R. Desai, T. Uchański, S. Masiulis, W. J. Stec, T. Malinauskas, J. Zivanov, E. Pardon, J. Steyaert, K. W. Miller, and A. R. Aricescu, “Cryo-EM structure of the human $\alpha 1\beta 3\gamma 2$ GABAA receptor in a lipid bilayer,” *Nature*, vol. 565, pp. 516–520, 2019.
- [85] H. H. Masahito Watanabe, Kentaro Maemura, Kiyoto Kanbara and Takumi Tamayama, “GABA and GABA Receptors in the Central Nervous System and Other Organs,” *Int. Rev. Cytol.*, vol. 213, pp. 1–47, 2002.
- [86] J. Rohrbough and K. Broadie, “Lipid regulation of the synaptic vesicle cycle,” *Nat. Rev. Neurosci.*, vol. 6, pp. 139–150, 2005.
- [87] N. C. Harata, A. M. Aravanis, and R. W. Tsien, “Kiss-and-run and full-collapse fusion as modes of exo-endocytosis in neurosecretion,” *Journal of Neurochemistry*, vol. 97, pp. 1546–1570, 2006.
- [88] B. J. Taylor P, “Synthesis, Storage and Release of Acetylcholine,” in *Basic Neurochemistry: Molecular, Cellular and Medical Aspects.*, 6th ed., 1999.
- [89] B. P. Bean, “The action potential in mammalian central neurons,” *Nat. Rev. Neurosci.*, vol. 8, pp. 451–465, 2007.
- [90] A. Takeuchi and N. Takeuchi, “Anion permeability of the inhibitory post-synaptic membrane of the crayfish neuromuscular junction,” *The Journal of Physiology*, vol. 191, pp. 575–590, 1967.
- [91] K. Krnjević and S. Schwartz, “The action of γ -Aminobutyric acid on cortical neurones,” *Experimental Brain Research*, vol. 3, pp. 320–336, 1967.
- [92] V. Y. Poon, S. Choi, and M. Park, “Growth factors in synaptic function,” *Front. Synaptic Neurosci.*, vol. 5, pp. 1–18, 2013.
- [93] K. Jaideep, “Is Epilepsy a Disease of Synaptic Transmission?” *Am. Epilepsy Soc.*, vol. 49, pp. 298–307, 2008.
- [94] P. M. Casillas-Espinosa, K. L. Powell, and T. J. O’Brien, “Regulators of synaptic transmission: Roles in the pathogenesis and treatment of epilepsy,” *Epilepsia*, vol. 53, pp. 41–58, 2012.
- [95] A. Sinning and C. A. Hübner, “Minireview: PH and synaptic transmission,” *FEBS Lett.*, vol. 587, pp. 1923–1928, 2013.

- [96] G. Mukandala, R. Tynan, S. Lanigan, and J. J. O'Connor, "The effects of hypoxia and inflammation on synaptic signaling in the CNS," *Brain Sci.*, vol. 6, no. 1, 2016.
- [97] P. Clamping, A. Introductory, G. To, and P. Clamp, "Patch Clamping," pp. 395–403, 2003.
- [98] B. Sakmann and E. Neher, "Patch clamp techniques for studying ionic channels in excitable membranes.," *Annu. Rev. Physiol.*, vol. 46, pp. 455–472, 1984.
- [99] D. L. Ypey and L. J. DeFelice, "the Patch-Clamp Technique Explained and Exercised With the Use of Simple Electrical Equivalent Circuits.," *Electr. Prop. Cells*, vol. 1, no. 615, pp. 1–55, 2005.
- [100] J. W. Gibbs, Y. F. Zhang, M. D. Shumate, and D. a Coulter, "Regionally selective blockade of GABAergic inhibition by zinc in the thalamocortical system: functional significance.," *J. Neurophysiol.*, vol. 83, pp. 1510–1521, 2000.
- [101] S. McDavid and K. P. M. Currie, "G-proteins modulate cumulative inactivation of N-type (Cav2.2) calcium channels.," *J. Neurosci.*, vol. 26, pp. 13373–83, 2006.
- [102] M. J. Stutts, C. M. Canessa, J. C. Olsen, M. Hamrick, J. A. Cohn, B. C. Rossier, and R. C. Boucher, "CFTR as a cAMP-dependent regulator of sodium channels.," vol. 269, pp. 847–850, 1995.
- [103] J. M. Pocock and H. Kettenmann, "Neurotransmitter receptors on microglia," *Trends in Neurosciences*, vol. 30, pp. 527–535, 2007.
- [104] J. S. Dittman and J. M. Kaplan, "Behavioral impact of neurotransmitter-activated G-protein-coupled receptors: muscarinic and GABAB receptors regulate *Caenorhabditis elegans* locomotion.," *J. Neurosci.*, vol. 28, pp. 7104–12, 2008.
- [105] D. E. Schutter, "An Active Membrane Model of the Cerebellar Purkinje Cell I . Simulation of Current Clamps in Slice," vol. 71, no. 1, 2019.
- [106] L. Mellander, A. S. Cans, and A. G. Ewing, "Electrochemical probes for detection and analysis of exocytosis and vesicles," *ChemPhysChem*, vol. 11, pp. 2756–2763, 2010.
- [107] S. H. White and T. E. Thompson, "Capacitance, area, and thickness variations in thin lipid films," *BBA - Biomembr.*, vol. 323, pp. 7–22, 1973.

- [108] A. Llobet, V. Beaumont, and L. Lagnado, “Real-time measurement of exocytosis and endocytosis using interference of light,” *Neuron*, vol. 40, pp. 1075–1086, 2003.
- [109] Y. Okada, “Patch clamp techniques : from beginning to advanced protocols,” Springer, 2012.
- [110] R. Horn and a Marty, “Muscarinic activation of ionic currents measured by a new whole-cell recording method.,” *J. Gen. Physiol.*, vol. 92, pp. 145–159, 1988.
- [111] J. S. Fan and P. Palade, “Perforated patch recording with -escin,” *Pflugers Arch. Eur. J. Physiol.*, vol. 436, no. 6, pp. 1021–1023, 1998.
- [112] Y. Abe, K. Furukawa, Y. Itoyama, and N. Akaike, “Glycine response in acutely dissociated ventromedial hypothalamic neuron of the rat: new approach with gramicidin perforated patch-clamp technique.,” *J. Neurophysiol.*, vol. 72, pp. 1530–1537, 1994.
- [113] D. L. Armstrong and R. E. White, “An enzymatic mechanism for potassium channel stimulation through pertussis-toxin-sensitive G proteins,” *Trends in Neurosciences*, vol. 15, pp. 403–408, 1992.
- [114] C. M. Armstrong and W. F. Gilly, “Access resistance and space clamp problems associated with whole-cell patch clamping,” *Methods Enzymol.*, vol. 207, pp. 100–122, 1992.
- [115] E. Neher and A. Marty, “Discrete changes of cell membrane capacitance observed under conditions of enhanced secretion in bovine adrenal chromaffin cells,” *Neurobiology*, vol. 79, pp. 6712–6716, 1982.
- [116] N. Fidler and J. M. Fernandez, “Phase tracking: an improved phase detection technique for cell membrane capacitance measurements.,” *Biophys. J.*, vol. 56, pp. 1153–62, 1989.
- [117] E. Sakmann, B., & Neher, *Single-channel recording.*, vol. Chapter 6. 2001.
- [118] J.-P. Salvétat, G. Briggs, J.-M. Bonard, R. Bacsa, A. Kulik, T. Stöckli, N. Burnham, and L. Forró, “Patch clamp technique: review of the current state of the art and potential contributions from nanoengineering,” vol. 339, 2013.
- [119] J. H. Scofield, “Frequency-domain description of a lock-in amplifier,” *Am. J. Phys.*, vol. 62, pp. 129–133, 1994.
- [120] Bentham, “Lock-in amplifier,” *Rev. Sci. Instrum.*, vol. 78, 2007.

- [121] C. V Kulkarni, W. Wachter, G. Iglesias-Salto, S. Engelskirchen, and S. Ahualli, “Monoolein: a magic lipid?,” *Phys. Chem. Chem. Phys.*, vol. 13, 2011.
- [122] J. P. Dilger and R. Benz, “Optical and electrical properties of thin monoolein lipid bilayers,” *J. Membr. Biol.*, vol. 85, pp. 181–189, 1985.
- [123] S. J. Attwood, Y. Choi, and Z. Leonenko, “Preparation of DOPC and DPPC supported planar lipid bilayers for atomic force microscopy and atomic force spectroscopy,” *Int. J. Mol. Sci.*, vol. 14, pp. 3514–3539, 2013.
- [124] F. Wang and J. Liu, “A Stable Lipid Interface with Headgroup-Inversed Phosphocholine and a Comparison with SiO₂,” *J. Am. Chem. Soc.*, vol. 137, pp. 11736–11742, 2015.
- [125] P. Calvez, T. F. Schmidt, L. Cantin, K. Klinker, and C. Salesse, “Phosphatidylserine Allows Observation of the Calcium-Myristoyl Switch of Recoverin and Its Preferential Binding,” *J. Am. Chem. Soc.*, vol. 138, pp. 13533–13540, 2016.
- [126] H. M. McConnell and A. Radhakrishnan, “Condensed complexes of cholesterol and phospholipids,” *Biochimica et Biophysica Acta - Biomembranes*, vol. 1610, pp. 159–173, 2003.
- [127] K. Puth, H. F. Hofbauer, J. P. Saénz, and R. Ernst, “Homeostatic control of biological membranes by dedicated lipid and membrane packing sensors,” *Biological Chemistry*, vol. 396, pp. 1043–1058, 2015.
- [128] S. Ballweg and R. Ernst, “Control of membrane fluidity: The OLE pathway in focus,” *Biological Chemistry*, vol. 398, pp. 215–228, 2017.
- [129] S. Ma, J. M. Sherwood, W. T. S. Huck, and S. Balabani, “On the flow topology inside droplets moving in rectangular microchannels,” *Lab Chip*, vol. 14, pp. 3611, 2014.
- [130] A. S. Bourinbaïar and C. F. Coleman, “The effect of gramicidin, a topical contraceptive and antimicrobial agent with anti-HIV activity, against herpes simplex viruses type 1 and 2 in vitro,” *Arch. Virol.*, vol. 142, pp. 2225–2235, 1997.
- [131] B. M. Burkhart, R. M. Gassman, D. A. Langs, W. A. Pangborn, W. L. Duax, and V. Pletnev, “Gramicidin D conformation, dynamics and membrane ion transport,” *Pept. Sci.*, vol. 51, pp. 129–144, 1999.
- [132] J. M. David and A. K. Rajasekaran, “Gramicidin A: A New Mission for an Old Antibiotic,” *J. Kidney Cancer VHL*, vol. 2, 2015.

- [133] D. W. Urry, "The Gramicidin A Transmembrane Channel: A Proposed 7_r(L,D) Helix," *Proc. Natl. Acad. Sci.*, vol. 68, pp. 672–676, 1971.
- [134] A. Ota, M. Šentjurc, M. Bele, P. A. Grabnar, and N. P. Ulrih, "Impact of Carrier Systems on the Interactions of Coenzyme Q10 with Model Lipid Membranes," *Food Biophys.*, vol. 11, pp. 60–70, 2016.
- [135] B. Frei, M. C. Kim, and B. N. Ames, "Ubiquinol-10 is an effective lipid-soluble antioxidant at physiological concentrations.," *Proc. Natl. Acad. Sci.*, vol. 87, pp. 4879–4883, 1990.
- [136] H. N. Bhagavan and R. K. Chopra, "Plasma coenzyme Q10 response to oral ingestion of coenzyme Q10 formulations," *Mitochondrion*, vol. 7, pp. 78–88, 2007.
- [137] J. T. Tan and A. R. Barry, "Coenzyme Q10 supplementation in the management of statin-associated myalgia," *Am. J. Heal. Pharm.*, vol. 74, pp. 786–793, 2017.
- [138] J. Tanaka, R. Tominaga, M. Yoshitoshi, K. Matsui, M. Komori, A. Sese, H. Yasui, K. Tokunaga "Coenzyme Q10: The Prophylactic Effect on Low Cardiac Output Following Cardiac Valve Replacement," *Ann. Thorac. Surg.*, vol. 33, pp. 145–151, 1982.
- [139] M. Jafari, S. M. Mousavi, A. Asgharzadeh, and N. Yazdani, "Coenzyme Q10 in the treatment of heart failure: A systematic review of systematic reviews," *Indian Heart J.*, vol. 70, pp. S111–S117, 2018.
- [140] G. López-Lluch, J. del Pozo-Cruz, A. Sánchez-Cuesta, A. B. Cortés-Rodríguez, and P. Navas, "Bioavailability of coenzyme Q10 supplements depends on carrier lipids and solubilization," *Nutrition*, vol. 57, pp. 133–140, 2019.
- [141] B. Östman, A. Sjödin, K. Michaëlsson, and L. Byberg, "Coenzyme Q10 supplementation and exercise-induced oxidative stress in humans," *Nutrition*, vol. 28, pp. 403–417, 2012.
- [142] G. S. Kelly, "Squalene and its potential clinical uses," *Altern. Med. Rev.*, vol. 4, pp. 29–36, 1999.
- [143] R. G. Langdon, K. Bloch, The biosynthesis of squalene. *J Biol Chem.* vol. 200(1), pp. 129–134, 1953.
- [144] I. City and C. H. F. Rowell, "Further Observations on the Biosynthesis of squalene," *J. Biol. Chem.*, vol. 237, pp. 283–305, 1981.

- [145] L. G. Passi S, De Pità O, Puddu P, “Lipophilic antioxidants in human sebum and aging,” *Free Radic Res*, vol. 36, pp. 471–7, 2002.
- [146] L. Jonuaskas, et.al., “Optically clear and resilient free-form optics 3D-printed via ultrafast laser lithography,” *Materials (Basel)*, vol. 10, no. 1, 2017.
- [147] C. L. Henderson, P. C. Tsiartas, L. W. Flanagan, S. N. Pancholi, S. A. Chowdhury, K. D. Dombrowski, A. N. Chinwalla, and C. G. Willson, “Photoresist characterization for lithography simulation .4. Processing effects on resist parameters,” *Adv. Resist Technol. Process. Xiv*, vol. 3049, pp. 212–223, 1997.
- [148] Y. Zhao, S. Inayat, D. a Dikin, R. S. Ruoff, and J. B. Troy, “Impedance characterization and modelling of an improved patch clamp device,” *Proc. Inst. Mech. Eng. Part N J. Nanoeng. Nanosyst.*, vol. 1, pp. 1–11, 2010.
- [149] K. Funakoshi, H. Suzuki, and S. Takeuchi, “Lipid bilayer formation by contacting monolayers in a microfluidic device for membrane protein analysis,” *Anal. Chem.*, vol. 78, pp. 8169–8174, 2006.
- [150] O. H. Wolkers W., *Cryopreservation of Red Blood Cells*. New York, NY: Springer US, 2014.
- [151] K. L. Scott, J. Lecak, and J. P. Acker, “Biopreservation of red blood cells: Past, present, and future,” *Transfus. Med. Rev.*, vol. 19, pp. 127–142, 2005.
- [152] C. Marrocco, V. Pallotta, A. D’Alessandro, G. Alves, and L. Zolla, “Red blood cell populations and membrane levels of peroxiredoxin 2 as candidate biomarkers to reveal blood doping,” *Blood Transfus.*, vol. 10, pp. 71–77, 2012.
- [153] J. B. Boreyko, G. Polizos, P. G. Datskos, S. A. Sarles, and C. P. Collier, “Air-stable droplet interface bilayers on oil-infused surfaces,” *Proc. Natl. Acad. Sci.*, vol. 111, pp. 7588–7593, 2014.
- [154] N. Tamaddoni, G. Taylor, et.al., “Reversible, voltage-activated formation of biomimetic membranes between triblock copolymer-coated aqueous droplets in good solvents,” *Soft Matter*, vol. 12, pp. 5096–5109, 2016.
- [155] C. G. Siontorou, G. P. Nikoleli, D. P. Nikolelis, and S. K. Karapetis, “Artificial lipid membranes: Past, present, and future,” *Membranes (Basel)*, vol. 7, pp. 1–24, 2017.

- [156] T. Osaki and S. Takeuchi, “Artificial Cell Membrane Systems for Biosensing Applications,” *Anal. Chem.*, vol. 89, pp. 216–231, 2017.
- [157] G. Wu, P. Feng, X. Wan, L. Zhu, Y. Shi, and Q. Wan, “Artificial Synaptic Devices Based on Natural Chicken Albumen Coupled Electric-Double-Layer Transistors,” *Nat. Publ. Gr.*, pp. 1–9, 2016.

Bibliography of Figures

- Sigma Aldrich, Retrieved 2020, from <https://www.sigmaaldrich.com/catalog/substance/siliconeoil123456314862911?lang=de®ion=DE>
- Avanti Polar Lipids. (2020). Retrieved from <https://avantilipids.com/product/850375>
- Blaus, B. (2013). Wikipedia. Retrieved from https://commons.wikimedia.org/wiki/File:Blausen_0843_SynapseTypes.png
- Brown., B. S. (1997). Biological Membranes. London: Elsevier".
- Conn, C. E. (2012). Effect of lipid architecture on cubic phase susceptibility to crystallisation screens. *Soft Matter*, 6884-6896 .
- HEKA Elektronik GmbH. (2020). Retrieved from https://www.heka.com/products/products_main.html#physiol_patch
- Krishnavedala. (2014). Wikipedia. Retrieved from chemical structure of Ubiquinone (Coenzyme Q): <https://en.m.wikipedia.org/wiki/File:Ubiquinone.svg>
- Lombardo, D. (2015). Amphiphiles Self-Assembly: Basic Concepts and Future Perspectives of Supramolecular Approaches. *Hindawi*, 22.
- McMahon, S. M. (2008). Mechanisms of membrane fusion: disparate players and common principles. *Nature*, 543–556.
- Rajasekaran, J. M. (2015). Gramicidin A: A New Mission for an Old Antibiotic. *Journal of Kidney Cancer and VH*.
- Rohrbough, J. (2005). Lipid regulation of the synaptic vesicle cycle . Springer Nature.
- Ronco, A. L. (2013). Squalene: a multi-task link in the crossroads of cancer and aging. *Functional Foods in Health and Diseases*, 462-476.
- Ruiz, M. (2007, January 31). Retrieved from Wikipedia: https://en.wikipedia.org/wiki/File:Cell_membrane_detailed_diagram_en.svg
- Scheller, Y. A. (2001). SNARE-mediated membrane fusion. *Nature*, 98–106.
- Tritech Research. (2020). Retrieved from <https://www.tritechresearch.com/PN-31.html>
- Watson, H. (2015). Biological membranes. Portland Press Limited, 43-70.
- Wikipedia. (2016). Retrieved from Wikipedia: https://commons.wikimedia.org/wiki/File:0312_Animal_Cell_and_Components.jpg

Acknowledgment

'I will praise You, O Lord, with my whole heart; I will tell of all Your marvellous works. I will be glad and rejoice in You'. Psalm 9

Firstly, and always, I would like to thank my lord and saviour **Jesus Christ** for the endless and priceless fatherhood, support, protection, joy and happiness.

Throughout the writing of this dissertation I have received a great deal of support and assistance. I would like to thank my supervisor, **Prof. Dr. Ralf Seemann**, whose expertise was so valuable in the formulating of the research topic and methodology. Thanks a lot also for the personal support and being always for us all the time. I would like to thank both **Prof. Dr. Albrecht Ott** for heading the defense committee and **Prof. Dr. Bianca Schrul** for being my second reviewer.

From my deep heart, I would particularly like to thank **Dr, Jean Baptiste Fleury, Dr. Michael Jung** and **Dr. Jose Nabor Castillo** for your priceless support in guiding me through all new techniques and for your willingness to help without discomforting or complains. You provided me with all tools that I needed to choose the right direction and successfully complete my dissertation. You supported me greatly and were always willing to help me.

Many thanks to **Judith Rech** and **Monika Schuck** for her helpful and cooperative attitude. I would also like to thank my beloved colleagues, **Roghayeh, Navid, Sevda, Leonard, Weiwei** and **Pegah**. In addition, I would like to thank my parents for their wise counsel and sympathetic ear. You are always there for me.

Finally, I wish to thank my family for always motivating me, and the greatest thank goes to my beloved wife **Madonna** for her support and patience with me.

I would never have done it without all of you..... Thank you

Harvey

Declaration

I hereby confirm that I have independently prepared this thesis and without using other aids than those stated. The data and concepts taken over from other sources or taken over indirectly are indicated citing the source. The thesis was not submitted so far either in Germany or in other country in the same or similar form in a procedure for obtaining an academic title.

Saarbrücken, Date

Harvey Nagy Mounier Tawfik

Eidesstattliche Versicherung

Hiermit versichere ich an Eides statt, dass ich die vorliegende Arbeit selbstständig und ohne Benutzung anderer als der angegebenen Hilfsmittel angefertigt habe. Die aus anderen Quellen oder indirekt übernommenen Daten und Konzepte sind unter Angabe der Quelle gekennzeichnet. Die Arbeit wurde bisher weder im In- noch im Ausland in gleicher oder ähnlicher Form in einem Verfahren zur Erlangung eines akademischen Grades vorgelegt.

Saarbrücken, Date

Harvey Nagy Mounier Tawfik